_____

Surfactants Dynamics at Interfaces
A series of Second Harmonic Generation experiments

Dissertation

zur Erlangung des akademischen Grades

"doctor rerum naturalium"

(Dr. rer. nat.)

in der Wissenschaftsdisziplin "Physikalische Chemie"

eingereicht an der

Mathematisch-Naturwissenschaftlichen Fakultät

der Universität Potsdam

von

Audrée Andersen

Geboren am 31. Juli 1979 in Québec, Kanada

Potsdam, den 10 Oktober 2005

Le commencement de toutes les sciences, c'est l'étonnement de ce que les choses sont ce qu'elles sont.

Aristote, Métaphysique, I, 2.

PREFACE

Interfaces are present throughout our everyday world; they separate different bulk regions of matter. Interfaces are interesting because they exhibit properties and behaviours that are very different from the adjacent bulk phases. Given their unique properties, interfaces play a central role in nature and within a variety of technological applications. For instance, catalytic reactions often occur at an interface.

Amphiphiles are molecules that possess a polar lyophilic head and a non-polar lyophobic tail. Due to their molecular asymmetry, they adsorb at liquid-liquid or liquid-air interfaces, modifying the physical and chemical properties of a system. They can be insoluble or soluble in the adjacent bulk phase. The insoluble one form monolayers at the air-water interface and can be regarded as a 2-dimensional model system. On the other hand, soluble surfactants are in thermodynamic equilibrium with the adjacent bulk phase; the surface coverage is given by the bulk concentration. Through the system, a range of dynamical events happens; molecules are in constant motion at the interface (as for insoluble ones), and there is a constant exchange between the adsorbed and dissolved species. These dynamics have an important impact on the macroscopic properties of materials. Thus, it is important to understand the molecular characteristics of such systems, for different time scales.

Because of their inherent surface specificity, second order nonlinear optics techniques are powerful analytical tools that can be used to gain information on molecular dynamics and reorganization of soluble surfactants. Surface second-harmonic generation (SHG) provides information about surface coverage, molecular orientation and symmetry of the arrangement of the amphiphiles within the adsorbed layer. Sum-frequency generation (SFG), on the other hand, gives information about the vibrational modes of the adsorbed species. Simply speaking, IR-VIS SFG spectrum can be regarded as an infrared spectrum of the topmost monolayer and SHG as the corresponding UV-VIS spectrum. In favourable cases, one can retrieve order parameters describing the chain conformations. In the first project achieved in this thesis, we used both techniques in order to elucidate a surprising isotherm and odd-even effect occurring in a soluble hemicyanine dye series.

Moreover, this work was necessary to identify and characterize a proper model system for the dynamic investigations.

Two new experimental techniques have been designed in this thesis, allowing for characterisation of the exchange dynamics as well as reorientation dynamics. In both experiments, surface SHG is the central element.

Surface rheology governs many everyday phenomena. For example, the ability of a surfactant solution to form a wet foam lamella is governed by the surface dilatational rheology. Only systems with a non-vanishing imaginary part of the surface dilatational modulus are able to form wet foam lamellas. The aim of this thesis is to illuminate the dissipative processes that give rise to the imaginary part of the modulus.

Several papers suggest that the imaginary part of the modulus is the consequence of a reorientation of the amphiphiles present at the air-water interface. They are assumed to adsorb in two distinct states, differing in their orientation. According to these authors, this reorientation process, together with the diffusion from the bulk, can properly describe the frequency dependence of the modulus. Nevertheless, no attempt has been made to measure this parameter directly. Our criticism on this approach is the discrepancy of the time scale. We expect the orientation dynamics to be in the picosecond dynamical scheme. However, the reorientation model would require that reorientation processes occur in the millisecond time range, which is against our physical intuition. In order to directly measure the introduced parameters, we designed a pump-probe experiment that addresses orientation dynamics.

In our opinion, they only dissipative process occurring in the millisecond time regime is the molecular exchange between the top-most adsorption layer and an adjacent sublayer. We consider the interface as an interphase, an extended region differing from the bulk consisting of a topmost monolayer and adjacent sublayer. With this model, we could successfully bridge the gap between the Gibbs elasticity from the isotherm and the high frequency limit of the modulus. Furthermore, measurements at different concentrations provide strong evidence for non-equilibrium states in the extended surface region. The assessment of this model required the design of an experiment that discriminates between the surface compositional term and the sublayer contribution.

ORGANIZATION OF THE THESIS

The content of this thesis is divided in four chapters. Surface second order nonlinear techniques being common to all experiments, **Chapter 1** contains a brief overview of theoretical background related to nonlinear optics, SHG and SFG.

Chapter 2 describes the equilibrium properties of our model system. The isotherm reveals very surprising features. By combination of various optical techniques, we derived a molecular picture of the interfacial architecture. This work has been necessary to establish the equilibrium properties of our model system.

Chapter 3 is dedicated to the exchange dynamics. A rapid oscillating bubble is creating a non-equilibrium state which is then probed by surface SHG. The data are used to assess the Lucassen-van den Tempel-Hansen model (LvdTH model). Evidence is provided that the exchange process is a decisive process that is responsible for the imaginary part of the surface dilatational modulus.

As outlined, the reorientation model introduces orientation dynamics in the millisecond range. In order to verify in a direct way, **Chapter 4** describes the construction of a pump-probe experiment. Two laser pulses hit the sample; the first pulse changes the hyperpolarisability of the molecule, the second pulse probes the recovery of the SHG signal. The delay between the pulses can be controlled in the picosecond to nanosecond time frame. Results on molecular orientational recovery of soluble surfactants are being discussed.

At the end of the thesis, an **appendix** containing all the abbreviations and symbols, used in this work is presented.

Table of Contents

LIST OF FIGURES

LIST OF TABLES

CHAPTER 1

FUNDAMENTALS OF NONLINEAR OPTICS

Interfaces are the boundary regions that separate different bulk areas of matter. They have special chemical, physical, and biological properties (different from the ones found in the bulk) that have drawn interest of the scientists from different fields[1,2]. These particular properties are due to the fact that at interfaces, molecules and atomic species experience an asymmetry in their environment. Indeed, interfaces are characterized by thermodynamics and kinetics that differ from the bulk, which leads for instance to different molecular motions and geometrical arrangements. Such interfacial phenomena can have an important impact on the macroscopic properties of some materials, and their understanding on a molecular level is of prime importance.

Despite this interest, it remains difficult to probe the chemistry of interfaces, especially for liquid interfaces (vapour-liquid, liquid-liquid, solid-liquid) with traditional spectroscopic methods. In the past decades, many surface sensitive techniques (XPS, LEED, EELS, STM, etc.) have been developed but many of these are limited to surfaces under vacuum, as they involve absorption, emission or scattering of charged particles[3,4].

Optical techniques do not have this limitation. They only require that one of the two media adjacent to the interface is transparent. Furthermore, optical techniques are non-destructive and are applicable in situ to any interface accessible by light.

Nonlinear optics is a field born in 1961 when Franken et al. demonstrated for the first time second-harmonic generation in a quartz crystal[5]. Nevertheless, it is only with the advent of reliable pulsed lasers systems, in the early nineties, that nonlinear optics has become a powerful surface analytical tool. Since then, nonlinear optical effects have been applied to study different materials. Moreover, quite a number of nonlinear optical

techniques have been developed especially for surfaces studies. Thus, it has been proven that second-harmonic generation (SHG) and sum-frequency generation (SFG) were suitable to become very effective techniques for probing surface properties with sub-monolayer sensitivity[3,6,7].

1.1.   INTERACTION OF LIGHT WITH MATTER: LINEAR OPTICS

Light is an electromagnetic wave that has a characteristic frequency in the order of 10^{14}-10^{15} Hz. In matter, only electrons are able to follow these rapid oscillations. Thus, when light propagates in matter, it causes a displacement of the electrons. They experience a force which is given by the local electric field strength. If this field is weak as compared to the inner atomic field, (created by a tungsten bulb, for example), the electron distribution responds harmonically, following the harmonic oscillator model. This defines the framework of linear optics. Its distinct feature is that the frequency of the light is conserved in the experiment.

Hence, in linear optics, the induced dipole, μ_{ind}, is directly proportional to the strength of the local electric field, E[8]:

$$\mu_{ind} = \underline{\mu}^{(1)} = \underline{\underline{\alpha}}\,\underline{E} \tag{1.1}$$

where α is the polarizability tensor that relates the local electric field to the induced dipole moment[2]. Since μ_{ind} is not necessarily in the same direction as E, α is therefore a second order tensor. On a macroscopic scale, a polarization wave P is induced, which is the dipole moment per unit volume:

$$P_{ind} = \underline{P}^{(1)} = \varepsilon_0\,\underline{\underline{\chi}}^{(1)}\,\underline{E} \tag{1.2}$$

where the linear susceptibility, $\chi^{(1)}$, replaces the polarizability α in equation 1.1. In equation 1.2, P and E are vectors, thus $\chi^{(1)}$ is again a tensor of rank 2, generally called susceptibility tensor. It describes the electric and optical anisotropy of matter. For a molecular system, the linear susceptibility depends on the number of molecules per unit

volume, N, and the molecular polarizability, α, averaged over all the orientations of the molecules in the system:

$$\underline{\underline{\chi}}^{(1)} \propto N \langle \underline{\underline{\alpha}} \rangle \qquad (1.3)$$

1.2.   INTERACTION OF LIGHT WITH MATTER: NONLINEAR OPTICS

If the radiation interacting with matter is very intense, comparable to the inner atomic fields, the movement of the electrons is not a harmonic wave anymore. The polarization wave is then composed of several harmonic waves of different frequencies. Thus, higher-order terms in E must be included in the expression for the induced dipole moment:

$$\mu_{ind} = \underline{\mu}^{(1)} + \underline{\mu}^{(2)} + \underline{\mu}^{(3)} + ... = \underline{\underline{\alpha}} \cdot \underline{E} + \underline{\underline{\beta}} : \underline{EE} + \underline{\underline{\gamma}} \vdots \underline{EEE} + ... \qquad (1.4)$$

where β and γ are the first and second hyperpolarizability tensors. The corresponding macroscopic expression is:

$$P_{ind} = \underline{P}^{(1)} + \underline{P}^{(2)} + \underline{P}^{(3)} + ... = \varepsilon_0 (\underline{\underline{\chi}}^{(1)} \cdot \underline{E} + \underline{\underline{\chi}}^{(2)} : \underline{EE} + \underline{\underline{\chi}}^{(3)} \vdots \underline{EEE} + ...) \qquad (1.5)$$

The second-order (nonlinear) susceptibility, $\chi^{(2)}$, and the third-order susceptibility, $\chi^{(3)}$, are macroscopic quantities that can be measured. Optical processes that arise from these susceptibilities are known as second-order and third-order nonlinear optical effects (NLO). The consequence of the presence of those higher-order terms is the generation of light at new frequencies. The induced polarization, P, as a function of the applied field, E, (associated to the light wave) is presented in figure 1.1 in the case of a linear and a nonlinear response.

In the case of a nonlinear response, the polarization wave can be decomposed into a DC and polarization components at the fundamental and second harmonic frequencies. A Fourier analysis of the resultant second-order NLO is presented in figure 1.2.
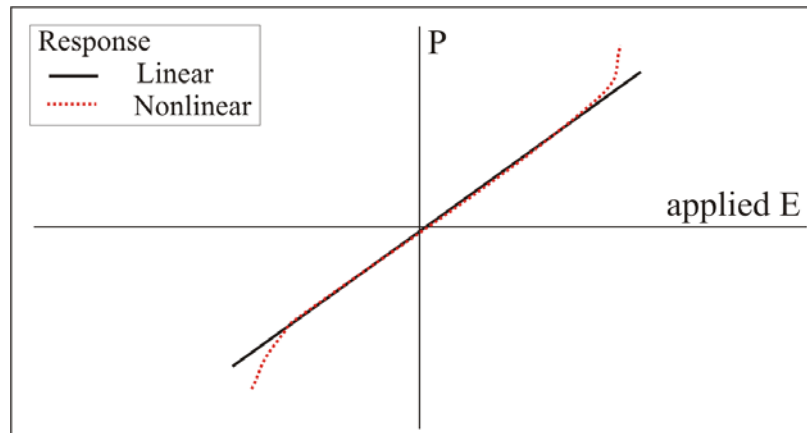
Figure 1.1   Induced polarization as a function of the applied field for linear and
second-order nonlinear materials.
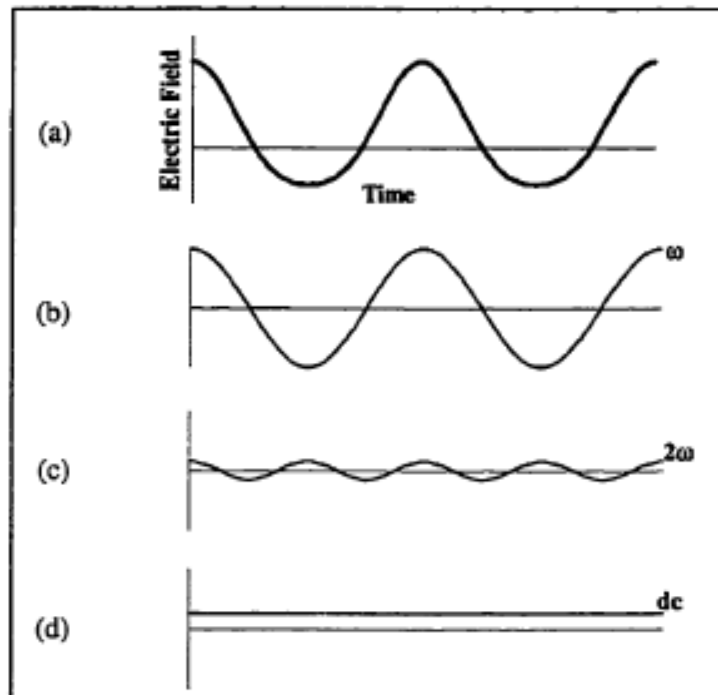
Figure 1.2   Fourier analysis of a polarization wave (a) of a second-order NLO material
to give waves with both the fundamental (b) and second harmonic
frequency (c), as well as a DC electric field (d). Taken from the literature[8].

The decisive structural information is contained in the nonlinear order susceptibility,
$\chi^{(2)}$. In a polarization dependent measurement, selected elements of $\chi^{(2)}$ are determined.

The orientation gas model relates the macroscopic quantity $\chi^{(2}$ to properties of the molecules. It states that the susceptibility tensor $\chi^{(2)}$, is given by the sum of the hyperpolarisabilities of all molecules.

This can alternatively be expressed by the number density of the molecules multiplied by their average orientation.

$$\underline{\underline{\chi_{ijk}^{(2)}}} \propto \sum\nolimits_{mol} \underline{\underline{\beta^{mol}}} \propto N\left\langle \underline{\underline{\beta^{mol}}} \right\rangle \tag{1.6}$$

where N is again the number of molecules per unit volume multiplied with the hyperpolarisability averaged over all orientations. From this, it is clear that the orientation average vanishes in bulk media such as liquids. Nonlinear second order processes can only occur in non-centrosymmetric media. This is also evident from the following symmetry consideration that can be worked out by analyzing the polarization response in a medium with inversion symmetry. The electric field E induces a polarization P. If the sign of E is reversed, the polarization response must invert also its sign and magnitude due to the prevailing symmetry.

The source term of the radiation at 2ω is given by a quadratic term of the electric field. Hence, the polarization response P matches –P, consequently $\chi^{(2)}$ must vanish in centrosymmetric media.

$$\begin{aligned}
\hat{i}E &= -E \\
\hat{i}P &= -P \\
P^{(2\omega)} &= \chi^{(2)}EE \\
-P^{(2\omega)} &= \chi^{(2)} - E - E \\
P &= -P \\
\chi^{(2)} &= 0
\end{aligned} \tag{1.7}$$

This is in accordance with the oriented gas model. The orientational average vanishes (see equation 1.6) in centrosymmetric media.

1.3. SECOND-ORDER NONLINEAR OPTICAL EFFECTS

There are many second-order NLO effects. Let's consider the interaction of intense laser pulse within a NLO medium. This medium is characterized by a second-order nonlinear susceptibility $\chi^{(2)}$; it is put in an optical field which consists of two different frequency components. The equation for the polarization response reads:

$$P_i^{(2)} = \chi_{ijk}^{(2)}(\omega_{out} = \omega_1 + \omega_2; -\omega_1, -\omega_2)E_j(\omega_1)E_k(\omega_2) \qquad (1.8)$$

where ω_{out} is the output frequency and ω_1 and ω_2, the input frequencies. The second-order NLO phenomena that have been used in this thesis are listed in table 1.1.

Name (Abbreviation)	Effect
Second-Harmonic Generation (SHG)	$\omega_{out} = \omega + \omega = 2\omega$
Sum-Frequency Generation (SFG)	$\omega_{out} = \omega_1 + \omega_2$
Optical Parametric Generation (OPG)	$\omega_{pump} = \omega_{idler} - \omega_{signal}$

Table 1.1 Second-order NLO effects.

The inherent surface specificity makes second order NLO experiments appealing for studying adsorption layers at the air-water interface. The bulk of the liquid does not contribute to the signal since the molecules are randomly oriented. Since the symmetry is broken in the interfacial region, SHG and SFG are probing specifically the adsorbed and oriented species.
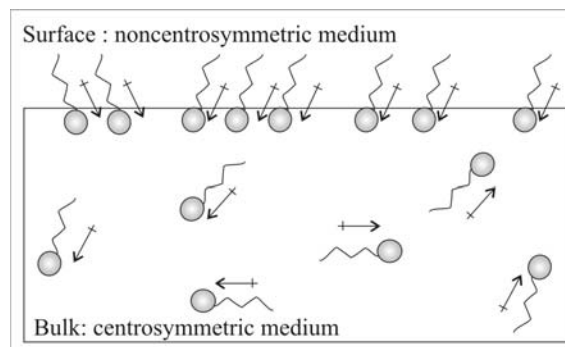
Figure 1.3   Centrosymmetric and a noncentrosymmetric medium.

1.4.   SECOND-HARMONIC GENERATION

SHG is a second-order NLO process, occurring when the response of a material, characterized by the vector P, acquires a component that is quadratic in the E of the input wave. One describes P with the second-order nonlinear susceptibility, $\chi^{(2)}$

$$P_i(2\omega) = \sum_{jk} \chi^{(2)}_{ijk} E_j(\omega) E_k(\omega) \tag{1.9}$$

where ω is the optical frequency. The polarization wave at the second-harmonic frequency 2ω is then the source of light at 2ω. When measuring the intensity, the polarization and the phase of this outgoing wave, one can determine selected elements of $\chi^{(2)}$ and determine the tensor elements. These elements are complex numbers, since they represent both the amplitude and the phase of the wave. The process of SHG is presented in Figure 1.4.
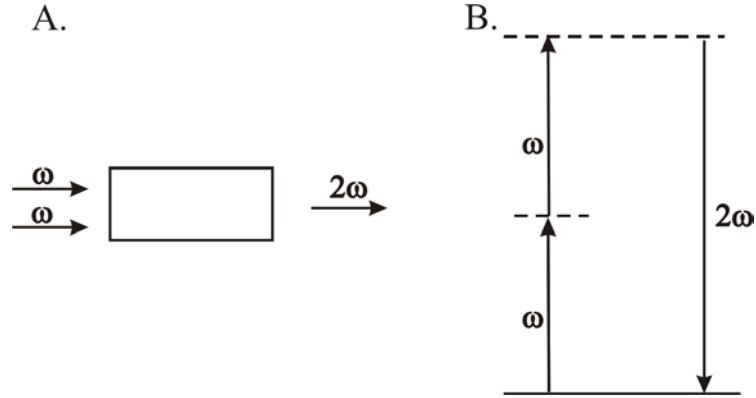
Figure 1.4   **A.** Geometry of SHG and **B.** Energy-level diagram for SHG

The source term for radiation at 2ω is given by equation 1.9. It is quadratic in the incident field, hence the following proportionality relationship between the incident light $I(\omega)$ and the SHG intensity $I(2\omega)$ holds:

$$I(2\omega) \propto \left| \chi^{(2)}_{eff} \right|^2 (I(\omega))^2 \tag{1.10}$$

where $\left|\chi_{eff}^2\right|$ is a linear combination of $\chi^{(2)}$ elements, with coefficients depending only on the experimental geometry (in particular, input and output polarizations, angle of incidence).

1.5. SURFACE SECOND-HARMONIC GENERATION

SHG is a powerful surface analytical technique. As outlined, $\chi^{(2)}$ completely vanishes in centrosymmetric media, and all bulk contributions are suppressed (with an exception of non-centrosymmetric crystals and chiral substances). In proximity of an interface between two centrosymmetric media (for example at the air-water interface), the inversion symmetry is broken and a nonzero value of $\chi^{(2)}$ describing the surface properties appears. Consequently, the SHG signal gives information about the integral over the orientational distribution of the molecules, as described by an interface susceptibility tensor. The signal can be detected in reflection as well as in transmission geometry. Usually, the one that is most easily accessible is chosen. Thus, when studying an interface, the technique is commonly called surface second-harmonic generation (SSHG).
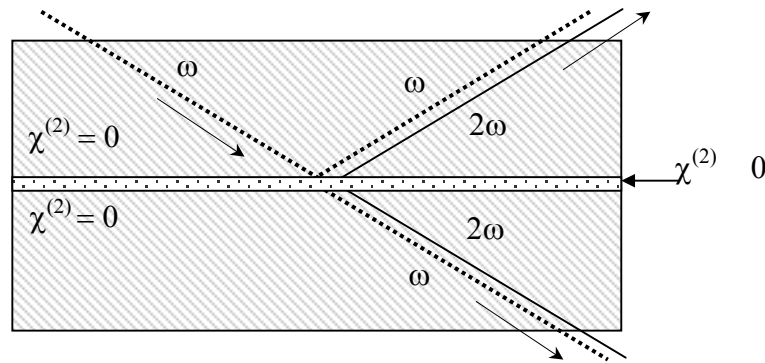
Figure 1.5   Schematic view of SHG at an interface

Equation 1.9 refers to surface fields, not to the one travelling through space. Surface fields can be calculated from the incident ones by applying the linear Fresnel equation for p- and s-light. Fresnel factors are given by the angle of incidence of the light and the refractive indices of the adjacent bulk media. The nonlinear induced polarization $P(2\omega)$ is the source of radiation at the harmonic frequency. The surface SHG field can be calculated from the induced polarization by the so-called L-factors. The derivation combines the continuity of the electric field and the phase-matching conditions.

In this thesis we are not attempting to calculate SHG intensities from the first principles. We are particularly interested in discussing ratio of intensities for different polarizations according to the oriented gas model. In some cases, we are working at the so-called magic angle. Here the following relation holds

$$\Gamma_m \approx \sqrt{I(2\omega)} \qquad (1.11)$$

where Γ_m is the orientated part of the amphiphile at the interface.

1.6.   THE d-TENSOR DESCRIBING SURFACE SECOND-HARMONIC GENERATION

Starting from this point, in order to make the explanation easier, the mathematical development is done in terms of matrices instead of tensors, as it was presented in the previous section. The components of the second order nonlinear susceptibility tensor can be defined as the proportionality constant relating the amplitude of the nonlinear polarization to the product of the field amplitudes, according to equation 1.8. $\chi^{(2)}$ is a third rank tensor containing 27 elements. Fortunately, the symmetry of the experimental arrangement reduces the number of independent elements and simplifies the analysis.

It is first useful to define the d-tensor as

$$\widetilde{d}_{ijk} = \frac{1}{2} \chi_{ijk}^{(2)} \qquad (1.12)$$

In the tensor $\widetilde{d}_{ijk}$, i describes the direction of the field amplitude of the nonlinear polarization, whereas j and k describe the directions of the two fundamental field amplitudes. In the case of SHG, j and k can be interchanged since the two waves have the same frequency:

$$\widetilde{d}_{ijk} = \widetilde{d}_{ikj} \qquad (1.13)$$

The number of independent coefficients is thus reduced to 18. The d-tensor can be written with a contracted notation, where we replace $\widetilde{d}_{ijk}$ by $\widetilde{d}_{il}$, with l representing jk.

The notation becomes then:

Jk	Xx	Yy	zz	yz,zy	zx,xz	xy,yx
L	1	2	3	4	5	6

while the index i: $1 = x$, $2 = y$ and $3 = z$. The susceptibility tensor can be written as:

$$\tilde{d}_{il} = \begin{bmatrix} d_{11} & d_{12} & d_{13} & d_{14} & d_{15} & d_{16} \\ d_{21} & d_{22} & d_{23} & d_{24} & d_{25} & d_{26} \\ d_{31} & d_{32} & d_{33} & d_{34} & d_{35} & d_{36} \end{bmatrix} \tag{1.14}$$

When we are far from the frequencies where the medium is absorbing, the NLO response is essentially independent of frequency. At these frequencies, the Kleinman symmetry conditions are valid[9]. Thus, the indices can be freely permuted, according to:

$$d_{123} = d_{132} = d_{213} = d_{231} = d_{312} = d_{321} \tag{1.15}$$

The number of independent coefficients becomes then 10 and $\tilde{d}_{il}$ can be written

$$\tilde{d}_{il} = \begin{bmatrix} d_{11} & d_{12} & d_{13} & d_{14} & d_{15} & d_{16} \\ d_{16} & d_{22} & d_{23} & d_{24} & d_{14} & d_{12} \\ d_{15} & d_{24} & d_{33} & d_{23} & d_{13} & d_{14} \end{bmatrix} = \begin{bmatrix} d_{xxx} & d_{xyy} & d_{xzz} & d_{xyz} & d_{xxz} & d_{xxy} \\ d_{xxy} & d_{yyy} & d_{yzz} & d_{yyz} & d_{xyz} & d_{xyy} \\ d_{xxz} & d_{yyz} & d_{zzz} & d_{yzz} & d_{xzz} & d_{xyz} \end{bmatrix} \tag{1.16}$$

in the contracted and extended notation.

If we consider a monolayer at the air-water interface with a dominant second-order hyperpolarizability $\beta^{(2)}_{\xi\xi\xi}$ along the molecular axis ξ, the components of the second-order susceptibility tensor, $\tilde{d}_{ijk}$, can be written in the simple form:

$$d_{ijk} = \frac{1}{2} N \langle (i \cdot \xi)(j \cdot \xi)(k \cdot \xi) \rangle \tag{1.17}$$

where N is the surface density of the molecules and i, j, k = x, y, z from the figure 1.6.

The equation represents the average over the molecular orientation distribution functions. In the substrate coordinate system, ξ possesses the following components:

$$\xi = (\sin\theta\cos\phi; \sin\theta\sin\phi; \cos\theta) \tag{1.18}$$
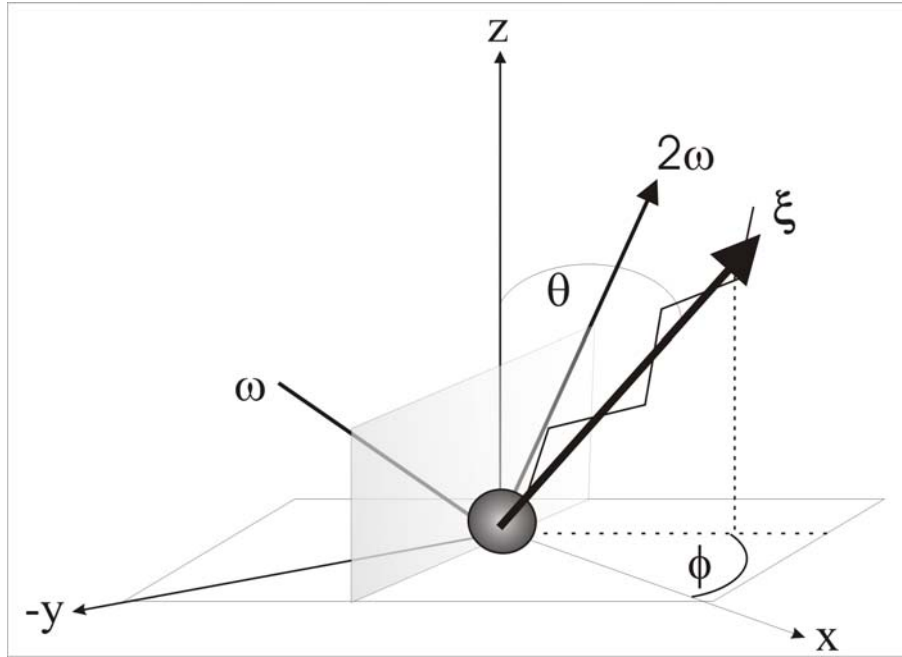
Figure 1.6   Coordinate system used in SSHG, where θ and ϕ are the polar and azimuthal angle between the substrate and the molecular axis of the surfactant.

For an isotropic distribution of molecules in a monolayer, there are only two independent non-vanishing components of d, d_{zzz} and $d_{xxz}= d_{yyz}$, and $\tilde{d}_{il}$ becomes

$$\tilde{d}_{il} = \begin{bmatrix} 0 & 0 & 0 & 0 & d_{15} & 0 \\ 0 & 0 & 0 & d_{24} & 0 & 0 \\ d_{15} & d_{24} & d_{33} & 0 & 0 & 0 \end{bmatrix} = \begin{bmatrix} 0 & 0 & 0 & 0 & d_{xxz} & 0 \\ 0 & 0 & 0 & d_{yyz} & 0 & 0 \\ d_{xxz} & d_{yyz} & d_{zzz} & 0 & 0 & 0 \end{bmatrix} \tag{1.19}$$

The two coefficients d_{xxz} and d_{zzz} can be calculated from equation 1.17 and 1.18:

$$d_{zzz} = \frac{1}{2} N \langle (z \cdot \xi)(z \cdot \xi)(z \cdot \xi) \rangle$$

$$d_{zzz} = \frac{1}{2} N \langle (\cos\theta)(\cos\theta)(\cos\theta) \rangle \qquad (1.20)$$

$$d_{zzz} = \frac{1}{2} N \langle \cos^3\theta \rangle$$

and

$$d_{xzz} = \frac{1}{2} N \langle (x \cdot \xi)(x \cdot \xi)(z \cdot \xi) \rangle$$

$$d_{xzz} = \frac{1}{2} N \langle (\sin\theta\cos\phi)(\sin\theta\cos\phi)(\cos\theta) \rangle$$

$$d_{xzz} = \frac{1}{2} N \langle \sin^2\theta\cos\theta \rangle \langle \cos^2\phi \rangle \qquad (1.21)$$

$$d_{xzz} = \frac{1}{4} N \langle \sin^2\theta\cos\theta \rangle$$

since $\langle \cos^2\phi \rangle = \frac{1}{2}$ for anisotropic distribution of ϕ. N represents the number of molecules.

1.7. SUM-FREQUENCY GENERATION

In an IR-VIS SFG experiment, a visible ω_{vis} and an infrared laser ω_{IR} beam are focused on the interface of interest. The spatial and temporal overlap of both pulses generates new light, which oscillates at the sum frequency $\omega_{vis} + \omega_{IR}$. The frequency of the infrared beam is changed and the SFG intensity is detected as a function of the wavelength and the polarization of the incoming beam. The spectrum contains information about the vibrational modes of adsorbed species. Figure 1.7 shows the experimental arrangement required to perform SHG experiments at air-water interface.

The number of photons N($\omega_{vis} + \omega_{IR}$) generated at the sum frequency is proportional to the energy of both pulses and inversely proportional to the area and the pulse width.

$$N_{\omega_{vis} + w_{IR}} \propto \left(\chi^{(2)} \right)^2 \frac{W_{\omega_{IR}} W_{\omega_{vis}}}{At} \qquad (1.22)$$
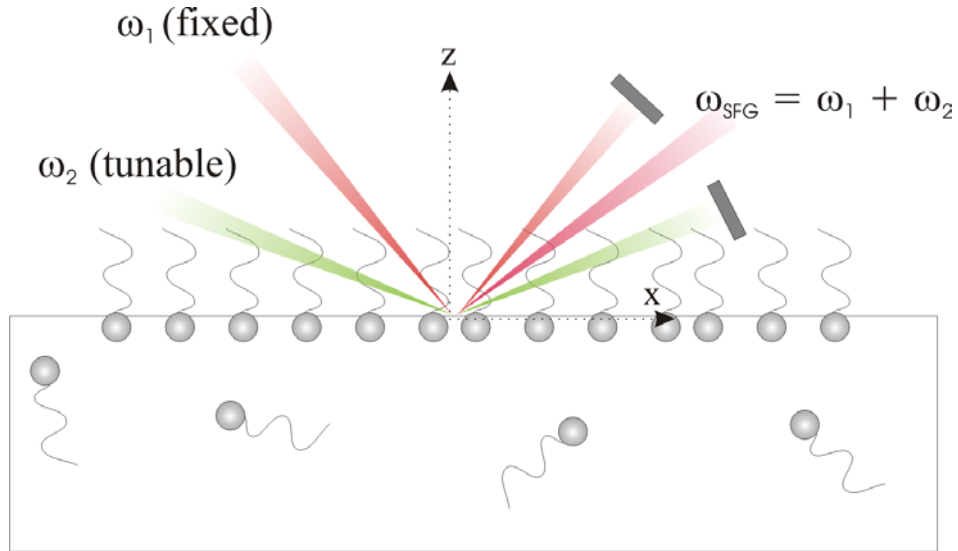
Figure 1.7   Experimental setup of an SFG

The structural information of the monolayer is contained in the nonlinear susceptibility of the second order. It can be separated into two contributions; a non-resonant term $\chi_{NR}^{(2)}$, which does not vary much with the scan of the infrared frequency, and a resonant term $\chi_{R}^{(2)}$, which contains the desired information about the vibrational modes of the molecule. Working with a dielectric material, the non-resonant term can be neglected.

The latter can be expressed in terms of the Raman cross-section and infrared transition dipole moments of the molecule, $M_{lm\nu}$ and $A_{n\nu}$

$$(\beta)_{lmn} = \frac{NA_{n\nu}M_{lm\nu}}{\omega_{\nu} - \omega_{IR} - i\Gamma_{\nu}} \tag{1.23}$$

where N is the number of adsorbed molecules, ω_{ν}, the resonant frequency of the vibrational mode with Γ_{ν} being the Lorentzian half-width driven by the external infrared frequency ω_{IR}. As a consequence of equation 1.23, a vibrational mode must be infrared and Raman active in order to be observed in a SFG spectrum. This limits substantially the number of allowed modes. Again, the nonlinear susceptibility tensor for SFG is given by the orientational gas model, as described in equation 1.6.

1.8. STRUCTURAL REQUIREMENTS FOR SHG

The high value of the hyperpolarizability of a molecule, β, comes from delocalized π−electrons as well as donors and acceptors groups. These features create an asymmetry in the response to an applied electric field; therefore it is desirable, when performing SSHG experiments, to utilize molecules having a long conjugation length.

To do so, scientists try to design molecules having strong electron donating substitutes (the strongest being by far $-N(CH_3)_2$) as well as strong electron acceptor groups (-NO being the strongest acceptor). An example of such a system is *p*-nitroaniline, where the $-NH_2$ group is the donor and the $-NO_2$ is the acceptor.
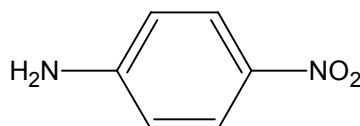
Figure 1.8   Molecular structure of *p*-nitroaniline

Together with the relative strength of donor and acceptor groups, another factor influences greatly the value of β, namely, the conjugation length between the donor and the acceptor. This has been subject of considerable experimental and theoretical interests as it defines the possibility of using organic nonlinear optics in integrated optics concepts[10-12]. The result of this extensive research is shown in figure 1.9.
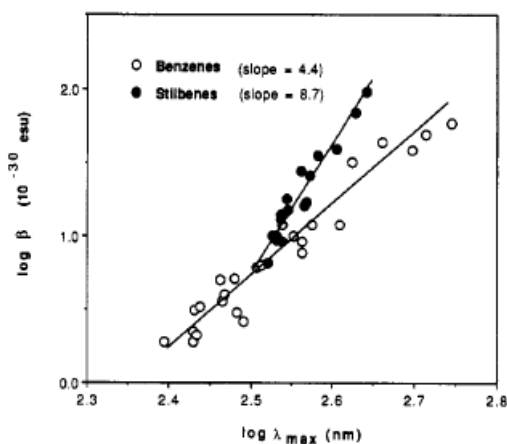
Figure 1.9   Example of the logarithm of β as a function of λ$_{max}$ for para-substituted benzenes and 4-4'-disubstituted stilbenes taken from the literature[13].

There is a link between the maximum of the linear absorption spectra and the conjugation length. The shorter is the conjugation length the blue-shifted is the absorption maximum. The conjugation length can also be related to the corresponding hyperpolarisability. For a class of materials, λ_{max} and β can be plotted on a log-log scale. In appears that β depends on λ_{max} with a factor of approximately $\beta \propto (\lambda_{max})^4$ to $(\lambda_{max})^9$. This has a very strong impact on the design of a proper model system.

One limitation of SSHG is that molecules with high hyperpolarizability have to be utilized. This boundary condition has created many problems in this project, due to the small hyperpolarizability of one of the samples.

NLO technique, like SHG, requires high peak power at the surface. For this reason, it can only be achieved by the use of pulsed laser sources. Such a system concentrates the light energy in a very short pulse leading to high peak power. As an example, a pulse having duration of one picosecond leads to a power of 1GW at the sample. On the other hand, when using a pulse of one nanosecond, the power at the sample is 1MW. The intensity of the incoming light cannot be changed arbitrarily; the upper limit is given by the damage threshold of the material. In short, SHG has a great potential for investigating interfaces, but a proper model system has to be designed.

REFERENCES

1.   Eisenthal, K. B. *Acc. Chem. Res.* **1993**, *26*, 636.

2.   Adamson, A., W.; Gast, Alice, O. *Physical Chemistry of Surfaces, 6th. Edition*; John Wiley & Sons, Inc.: New-York, USA, 1997.

3.   Shen, Y. R. *Annu. Rev. Phys. Chem.* **1989**, *40*, 327.

4.   Marruchi, L., Paparo, D., Cerrone, G., de Lisio, C., Santamato, E., Solimeno, S., Ardizzone, S., Quagliotto, P. *Optics and Lasers in Engineering* **2002**, *37*, 601.

5.   Franken, P. A., Hill, A.E., Peters, C.W., Weinrich, G. *Phys. Rev. Lett.* **1961**, *1*, 118.

6.   Shen, Y. R. *Nature* **1989**, *337*, 519.

7.   Shen, Y. R. *Surf. Sci.* **1994**, *299-300*, 551.

8.   Stucky, G. D., Marder, S.R., Sohn, J.E. Linear and Nonlinear polarizability. In *Materials for Nonlinear Optics Chemical Perspectives*; Marder, S. R., Sohn, J.E., Stucky, G.D., Ed.; American Chemical Society: Washington, 1991; pp 2.

9.   Kleinman, D. A. *Phys. Rev.* **1962**, *126*, 1977.

10.   Dulcic, A., Flytzanis, C., Tang, C.L., Pepin, D., Fitzon, M., Hoppiliard, Y. *J. Chem. Phys.* **1981**, *74*, 1559.

11.   Oudar, J. L., LePerson, H. *Opt. Comm.* **1975**, *13*, 164.

12.   Oudar, J. L. *J. Chem. Phys.* **1977**, *67*, 446.

13.   Cheng, L. T., Tam, W., Stevenson, S.H., Meredith, G.R. *J. Phys. Chem.* **1991**, *95*, 10631.

CHAPTER 2

ON THE IDENTIFICATION OF A PROPER MODEL SYSTEM

The Gibbs dividing surface is a too simple concept. It is desirable to view the interface as an interphase, in other words, as an extended region consisting of a topmost monolayer and an adjacent sublayer differing in its properties from the bulk.

Optical techniques can be used to probe selectively different elements of the interfacial architecture. SSHG measures only the oriented part of the interfacial region. Other techniques, like ellipsometry, evaluate both the topmost monolayer and the sublayer. IR-VIS SFG gives insights in the molecular conformation of the adsorbed species. The combination of various experiments gives a structural description of the interfacial architecture.

Among the molecules forming monolayers, several stilbazium dyes have attracted interest in the last years because of their strong fluorescence, their solvatochromism and their electrochromism that make them useful as molecular probes[1-3]. They are also interesting candidates for the integrated optics.

Laschewsky et al synthesized a homologous series of soluble amphiphiles containing stilbazium chromophores[4]. Due to their high hyperpolarisability, they are promising model system for our subsequent studies on surfactant dynamics. In this chapter, we characterize their equilibrium properties by SSHG, IR-VIS SFG, UV-VIS spectroscopy, surface tensiometry, ellipsometry and BAM for different chain lengths.

2.1. GIBBS MONOLAYERS

Amphiphiles are surface-active molecules (or *surfactants*) that are formed by a lyophilic head and a lyophobic tail, as depicted in figure 2.1C. The solubility of an amphiphilic molecule in water depends on the balance between the alkyl chain length and the strength of the hydrophilic head[5]. When they are insoluble, they self-organize at the interface (liquid-liquid or gas-liquid) to form a quasi 2-dimensional system, which is called Langmuir monolayer (Fig. 2.1A.)[6].

When the balance of the parameters makes the surfactants soluble, they create what is called a Gibbs monolayer. In this case, they self-organize at the interface and form a monolayer by adsorption. This adsorption layer is in thermodynamic equilibrium with the adjacent bulk phase, a feature that is the decisive difference from the Langmuir monolayers. At higher concentrations, formation of micelles (Fig. 2.1B) or aggregates can occur, leading to a number of interesting phenomena. Finally, a fast exchange between the molecules composing the system is observed, which makes the experimental investigation more complicated.
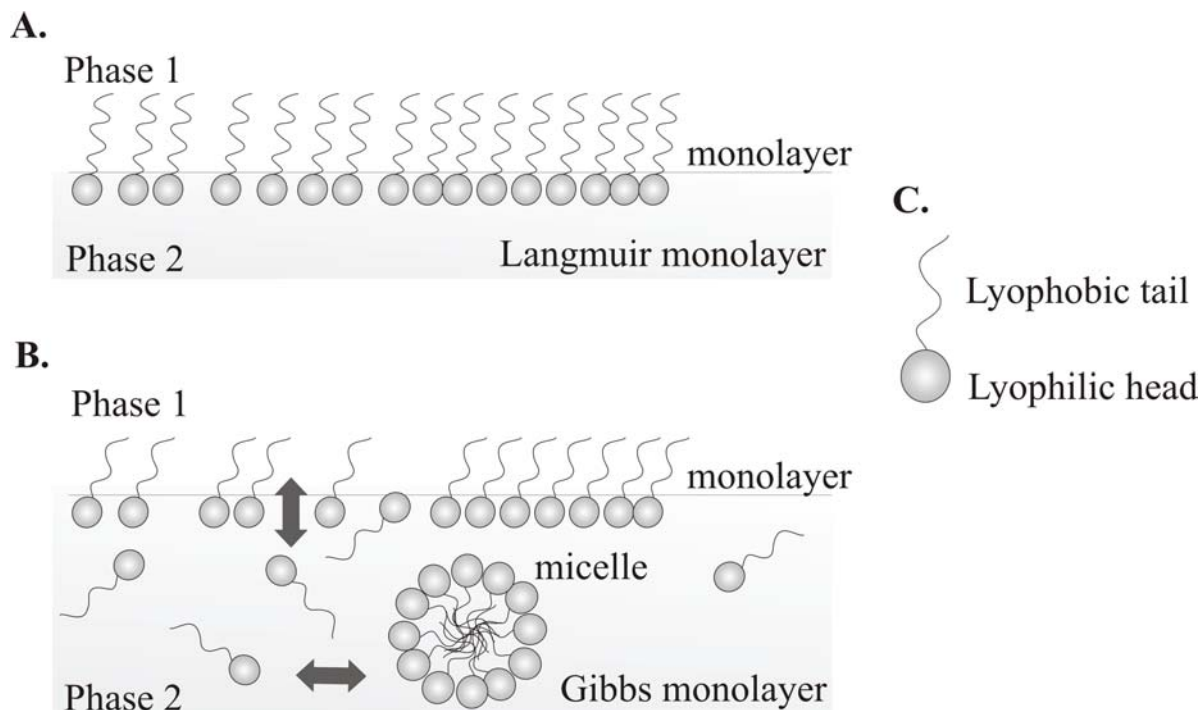
Figure 2.1   Example of an amphiphilic system A. Langmuir monolayer, B. Gibbs monolayer, C. Amphiphilic molecule.

The concentration of surfactant at which micelles appear is known as critical micellar concentration (CMC). Below the CMC surfactants are present as individual molecules, whereas above the CMC, they form aggregates. The presence of micelles in the solution brings some changes in the physical properties of the system.

The molecular structure of the amphiphiles is also influencing the surface tension and the surface properties of the system. The length of the lyophobic chain, the size of the lyophilic head and the degree of lyophilicity are all factors to be taken into account when studying the properties of such a system[7]. Thus, the most common analysis of this layer relies on a proper analysis of the equilibrium surface tension, γ.

2.2. SURFACE TENSION

The existence of condensed phase is a consequence of an intermolecular attractive force. Molecules in the bulk experience an isotropic force field. Those on the surface have no neighbouring atoms above, giving rise to surface tension.
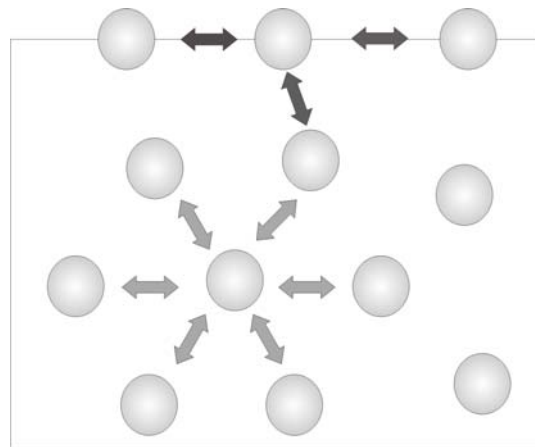
Figure 2.2   Example of the forces shared with the neighbouring atoms in the bulk and at the surface.

One can also describe the surface tension γ by expressing it as the work dW needed to change the surface area (dA) of a sample (constant temperature and volume):

$$dW = \gamma dA \qquad\qquad (2.1)$$

The surface tension of water at constant temperature changes significantly with the addition of organic or inorganic solutes into the aqueous medium. More than 100 years ago, Gibbs derived the relation between the surface tension, γ, of a solution and its solute concentration. In its simplest form, this equation reads

$$\Gamma_2 = -\frac{1}{mRT}\frac{d\gamma}{d\ln(c)} \qquad (2.2)$$

where Γ_2 is the excess amount of solute adsorbed per unit surface area of the liquid and c, the molar concentration of the solute in the medium. The factor *m* is 1 when in presence of non-ionic surfactant, and 2 when the surfactant is ionic.

2.3. TENSIOMETRY

The measurement of the surface tension (air-liquid interface) is based on force measurements of the interaction of a probe with the surface. A probe is hung on a balance and brought into contact with the liquid interface tested. The forces experienced by the balance as the probe interacts with the surface of the liquid are used to calculate surface tension.

These forces depend on many factors: the size and the shape of the probe, the contact angle of the liquid/solid interaction and the surface tension of the liquid. The size and shape of the probe are easy to control. The contact angle is controlled to be zero (complete wetting). This is achieved by using probes with high-energy surfaces (e.g. platinum).

The mathematical interpretation of the force measurements depends on the shape of the probe used. The DuNouy ring and the Wilhelmy plate are mostly used. The two probes are depicted in figure 2.3.

In this thesis, the surface tension measurements have been performed with the DuNouy ring used as a probe. Therefore, this method will be explained.
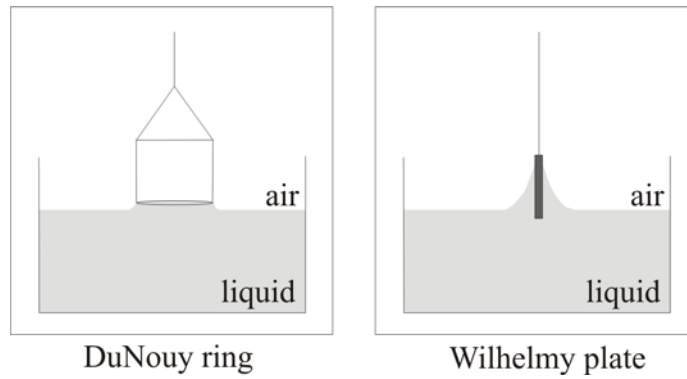
Figure 2.3   DuNouy ring and Wilhelmy plate used for surface tension measurements.

The DuNouy ring utilizes the interaction of a platinum ring with the surface to be tested. The ring is pulled through the liquid/air interface and the maximum downward force directed to the ring is measured. An example of the different steps of the measurement is presented in figure 2.4.
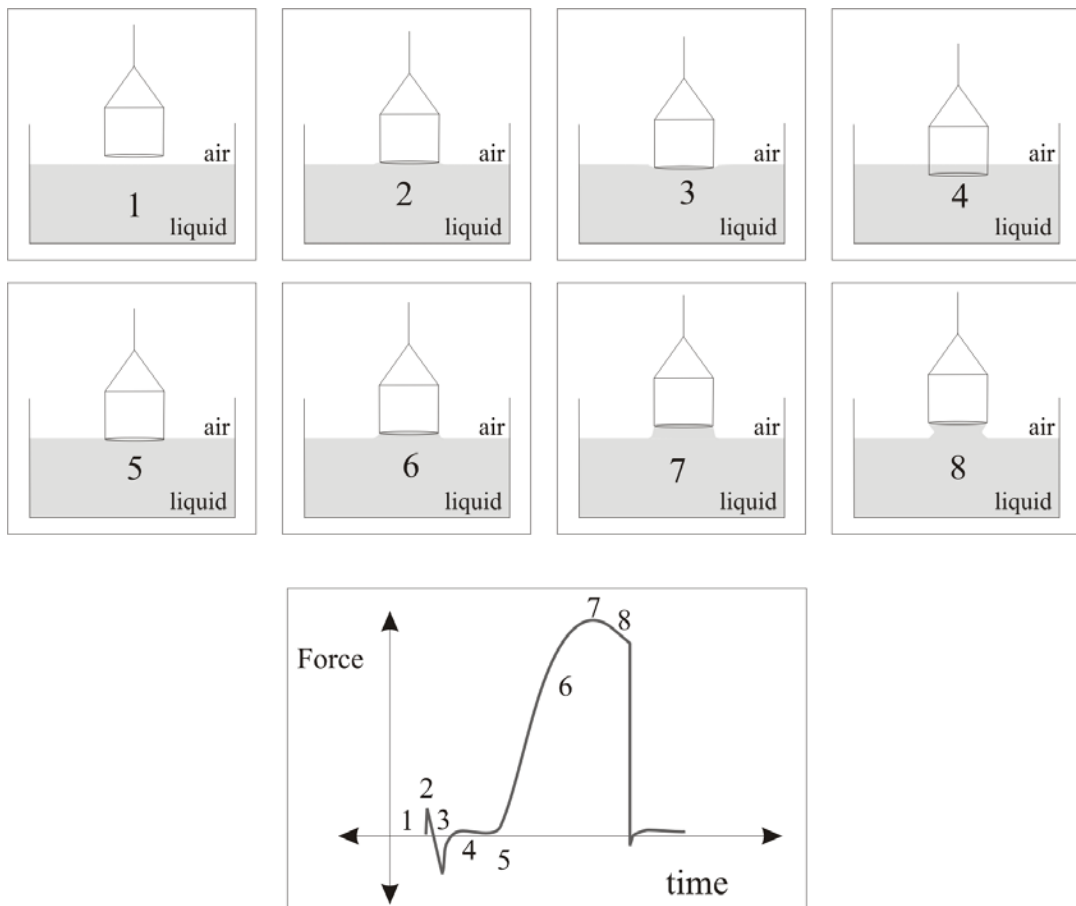
Figure 2.4   Measurement of surface tension with the DuNouy ring method.

The ring starts above the surface, where the force is zeroed (1). Then, moving down, the ring hits the surface (2) and we can observe a slight positive force due to the cohesive forces. The ring is pushed through the surface, causing a small negative force (3). The ring is moved up again, breaks through the surface (4) and when lifted through it, (5) the force increases (6) until a maximum W_g is reached (7). Finally, the force decreases a little until the lamella breaks (8).

From this measurement, the surface tension is calculated according to the following equation[8]:

$$\gamma = \frac{W_g}{4\pi R} \qquad (2.3)$$

where Wg is the pull of the ring (measured from the experiment) and $4\pi R\gamma$ the downward pull. R is the radius of the ring. This method is, however, not direct. One must use correction factors that take into account the dimensions of the ring (the perimeter, ring wire thickness and the effect of the opposite inner sides of the ring to the measurement).

2.4. ELLIPSOMETRY

Ellipsometry refers to a class of optical experiments that measure changes in the state of polarization upon reflection or transmission on the sample of interest. It is a powerful technique for the characterization of ultrathin films at fluid interfaces[9]. In favorable cases, thicknesses of thin films in the range of Angström can be accurately measured. It is possible to quantify submonolayer surface coverages with a resolution down to 1/100 of a monolayer or to measure the orientation adopted by the molecules on mesoscopic length scales. The only requirement for the experiment is that the sample must reflect laser light.

A typical ellipsometric experiment is depicted in figure 2.5. Light, having a well-defined state of polarization, is incident on a sample. The reflected light usually differs in its state of polarization and these changes are measured and quantified in an ellipsometric experiment.
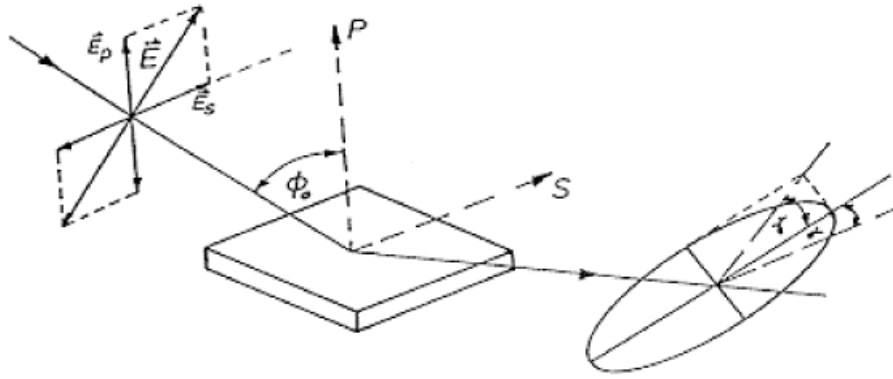
Figure 2.5   Scheme of an ellipsometry experiment.

An ellipsometric measurement yields two quantities, Δ and Ψ, which are sensitive to the interfacial architecture. The basic equation of ellipsometry relates both quantities to the complex reflectivity coefficients, r_p and r_s, for $\hat{p}$ and $\hat{s}$ polarized light:

$$\tan \Psi e^{i\Delta} = \frac{r_p}{r_s} \tag{2.4}$$

The ellipsometric angle Δ measures changes in the phase upon reflection, whereas Ψ probes the reflectivity properties of the sample.

Usually a monolayer on a non-absorbing dielectric support does not change the reflectivity of the sample and hence in the ultrathin film limit only a single quantity is obtained. Therefore, all measured quantities remain strongly coupled and the data analysis is restricted to a single quantity, the changes in Δ. The ellipsometric experiment yields the difference $d\Delta$ between the covered (Δ) and uncovered surface (Δ_0), which is proportional to the following integral of the dielectric function ε across the interfacial region[10]

$$\eta = \int \frac{(\varepsilon - \varepsilon_1)(\varepsilon - \varepsilon_2)}{\varepsilon} dx \tag{2.5}$$

where ε_1 and ε_2 are the dielectric constants of the adjacent bulk phases, in our case air and water, respectively.

Although optical techniques possess an inherent potential for the characterization of the air-water or oil-water interface, the characterization of adsorption layers of soluble surfactants is a tricky business due to the low number density at the interface, the formation of only fairly thin layers (<2 nm) in the presence of dissolved amphiphiles in the bulk phase. The established way to retrieve surface coverage relies on a proper thermodynamic interpretation of equilibrium surface tension isotherms, a tedious enterprise that demands faster, more convenient, and more accurate alternatives.

Ellipsometry has been proposed as such an alternative[11,12]. In many experiments it is possible to establish from first principles a direct proportionality between the ellipsometric response and surface coverage. If the dielectric constant of the support exceeds those of all other media (ε_2 { ε ، ε_1), as is frequently the case for adsorption onto solid supports, the following simplification applies:

$$\eta = \frac{\varepsilon_1 - \varepsilon_2}{\varepsilon_1} \int (\varepsilon - \varepsilon_1) dx \tag{2.6}$$

A linear relationship between ε and the prevailing concentration c of amphiphile within the adsorption layer is well-established[13]

$$\varepsilon = \varepsilon_1 + c \cdot \frac{d\varepsilon}{dc} \tag{2.7}$$

This relation yields a direct proportionality between the quantity η and the adsorbed amount Γ.

$$\eta = \frac{\varepsilon_1 - \varepsilon_2}{\varepsilon_1} \cdot \frac{d\varepsilon}{dc} \int c\, dx = \frac{\varepsilon_1 - \varepsilon_2}{\varepsilon_1} \cdot \frac{d\varepsilon}{dc} \cdot \Gamma \tag{2.8}$$

However, none of the assumptions used to derive equation 3.8 applies for adsorption layers at the liquid-air interface. In fact, the proportionality between the ellipsometric response and the adsorbed amount Γ may hold, but must be established experimentally.[14]

2.5. BREWSTER ANGLE MICROSCOPY

The existence of a Brewster angle is a peculiarity of p-polarized light. The reflectivity coefficient r_p vanishes at the Brewster angle, as it is presented in figure 2.6.
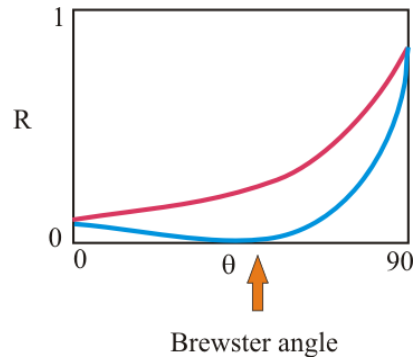
Figure 2.6   Representation of the Brewster angle.

Hence, no light is reflected there. However, a monolayer at the air-water interface yields a certain amount of reflected light, which is sufficient to produce an image. This is presented in figure 2.7. The inhomogeneities of Langmuir films, for example, on scales larger than a few micrometers can be detected.
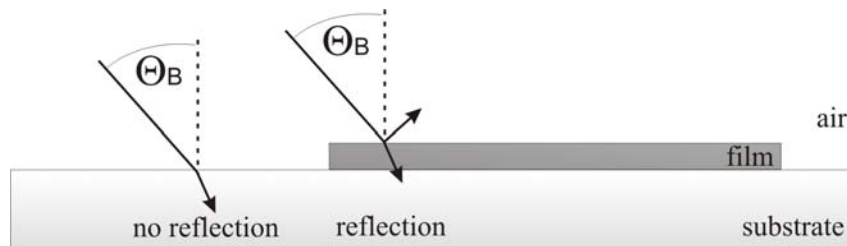
Figure 2.7   Reflection of p-polarized light set at the Brewster angle in absence and presence of a film.

A general setup of Brewster angle microscopy (BAM) is presented in figure 2.7. The air-water interface is illuminated at the Brewster angle with laser light polarized in the plane of incidence. The reflected light is collected through an objective and directed towards a CCD camera. The interpretation of images is in general quite simple and more direct than in fluorescence microscopy since the reflected light is as high as the density of the layer is high. Moreover, there is no need for a fluorescent probe, as it is required in the case of fluorescence microscopy.
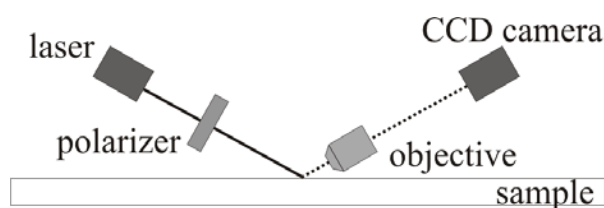
Figure 2.8   Setup of a Brewster angle microscope.

2.6. MATERIALS

The homologous series of N-n-alkyl-4'-(dimethylamino)-stilbazium bromides HC*n* with *n* = 5-8 used in this project has been kindly provided by Prof Dr Laschewsky. They have been synthesized according to a procedure described in the literature[15,16]. Moreover, they have been purified by an automatic high-performance purification apparatus in order to get surface-chemically pure solutions. The molecule is showed in figure 2.9.
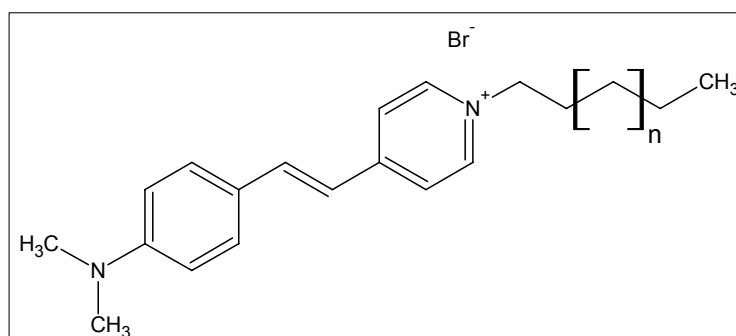
Figure 2.9   N-n-alkyl-4'-(dimethylamino)-stilbazium bromides, HC*n*

Different solutions having different concentrations (10, 30, 60, 150, 300, 400, 700 and 1000 μmol) have been prepared by dissolving the solid in Milli-Q water (resistance: 18,2 MΩ). Due to the poor solubility of the substance, the solutions had to be sonicated for at least 10 minutes at room temperature in order to get homogeneous solutions. To prevent from chemical degradation, they have been stored in the refrigerator, covered by aluminium foil. The solutions, kept in these conditions, are stable for at least one month.

The -$N(CH_3)_2$ unit of the molecule, together with the π-system of the benzyl-pyridium group, leads to a high hyperpolarizability, necessary to get a good SSHG signal.

2.7. INSTRUMENTATION

2.7.1   Surface tension measurements

Surface tension measurements have been performed in order to verify the purity of the substances used in the project. A Krüss Tensiometer Control Panel (K11) has been utilized, using the ring method. For each measurement, the Huh and Mason correction has been automatically applied, and two series of measurements have been performed.

2.7.2   UV-VIS spectroscopy

The UV-spectra were carried out with an Agilent 8453 UV–VIS spectrophotometer using a 1cm cuvette.

2.7.3   Ellipsometry measurements

Ellipsometry on the different hemicyanine aqueous solutions was performed on a Multiskop (Optrel GmBH), in the nullellipsometry mode. The setup used a laser, polarizer, compensator, sample and analyser arrangement. The measurements were carried out at an angle of 59 degrees and a fixed wavelength of 632.8 nm.

2.7.4   Brewster Angle Microscopy

BAM on the different hemicyanine aqueous solutions was performed on a Multiskop (Optrel GmBH), in the Brewster angle microscopy mode. The setup used a laser, polarizer, sample, objective and a CCD camera arrangement. The measurements were carried out at an angle of 56 degrees and a fixed wavelength of 632.8 nm.

2.7.5   Infrared Spectroscopy

Infrared spectra have been taken from the substance in the form of KBr pellets, in order to look for the main vibration bands from the molecule. Infrared measurements have been performed with a Nicolet FTIR-impact 400 spectrometer. The resolution was 4 cm^{-1} and 64 scans were taken for each measurement.

2.7.6   SSHG Characterization

The SHG system used during all the researches done in this work is an active/passive mode-locked Neodynium: yttrium–aluminum–garnet (Nd:YAG) laser (B.M. Industries, YAG 502 DPS 7910DP). The laser pulses are 35 ps, and the repetition rate is 10 Hz. The intensity after the oscillator was always 0,05 W and was varying between 0,004 and 0,01 W for the 532nm light.

In this part of the project, the experiment has been carried out with the frequency-doubled light at 532 nm. However, for each part of this thesis, a different setup has been built, in order to get the right signal.

In the case of the characterization of the hemicyanine dyes series by SSHG, the experiments have been performed on a flat surface, in a Petri dish, according to the setup presented on Fig 2.7. The configuration uses a combination of different $\lambda/2$ plates, which allow one to perform an orientation experiment, depending on their position, as well as the use of a Glen-Thompson prism.

A $\lambda/2$ plate turns the light but allows it to remain in the same state of polarization (for example, linearly polarized light remains linearly polarized light). In this setup, the first $\lambda/2$ plate is set in a way that the light is going vertically towards the system, giving a lot of intensity. The Glen-Thompson prism makes the light becoming p-polarized and by turning the second $\lambda/2$ plate from 45 degrees, one can go from p- to s- polarized light. The last $\lambda/2$ plate remains in the p-polarized position, and therefore it is possible to perform the orientation experiment. When one wants to measure simply normal intensity, one has to set the system in an s-p polarization state (s-polarized for the second and p-polarized for the third $\lambda/2$ plate).

The incoming beam is passing first through a narrow-band interference filter (532 BP, LOT-Oriel) in order to be sure we have only 532nm light going to the sample. The frequency-doubled light generated at the interface is then separated from the fundamental light by use of a series of visible cutoff filters (UG5, UG11, Schott) and a narrow-band interference filter (266 BP5, LOT-Oriel). These filters are presented in figure 2.10.
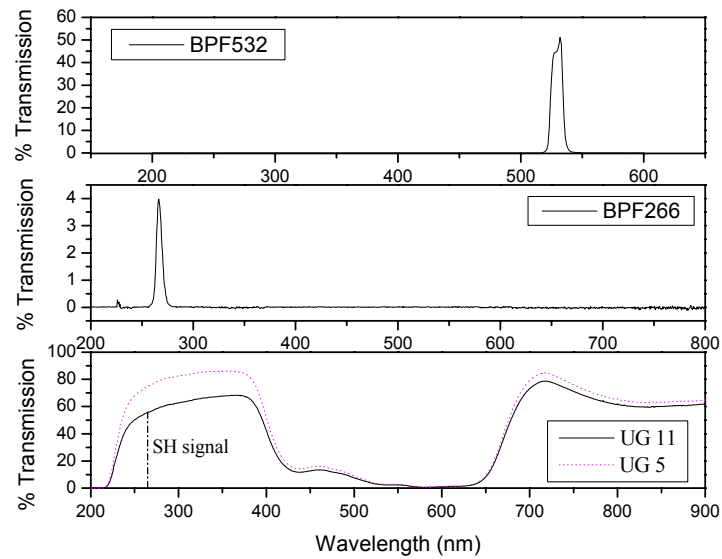
Figure 2.10   Absorption spectra of the filters used in the SSHG setup.

The SH light is detected by a photomultiplier tube (R1398, Hamamatsu) with a quantum efficiency of 15%, and a cathode radiant sensitivity of 35 mAW-1 at 266 nm. The supply voltage over the photomultiplier tube is 1850 V (V5D, Seefelder Messtechnik). Finally, the detected signal is processed via an oscilloscope (54720D, Hewlett-Packard) and integrated by a computer program.
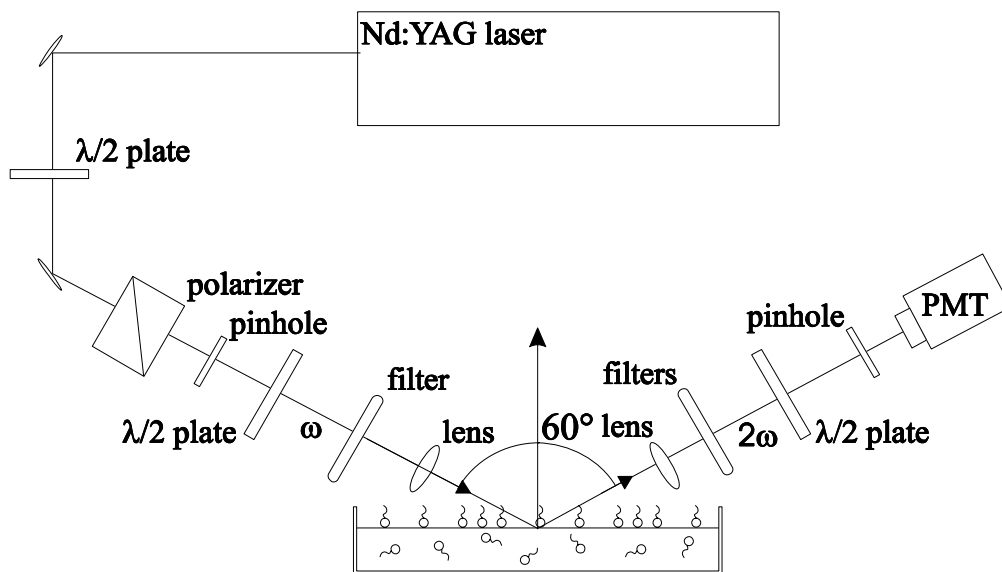
Figure 2.11   Scheme of the setup used in a flat surface configuration (Petri dish).

2.7.7   Surface SFG Characterization

The optical scheme of the SFG spectrometer is presented in figure 2.12 and 2.13. The picosecond mode-locked Nd:YAG laser (Ekspla, PL2143A/SS) generates optical pulses of three wavelengths: the fundamental Nd-YAG radiation (1064 nm), the second harmonic (532 nm) and the third harmonic (355nm). The duration pulse of the fundamental radiation is 30 ps and the repetition rate 10Hz.

Mirrors M1-M2 direct the 1064 nm beam from the laser to the Harmonics Unit. The third harmonic and fundamental beam from the harmonic unit pump the parametric generator PG401/DFG. Mid-infrared PG401/DFG output having a tuning range 2,3 –10 μm is a result of difference frequency generation when mixing the idler wave of optical parametric generation with 1064 nm radiation of the laser.

Mirrors M5, M10 and M11 direct the mid-IR beam to the sample. Beamsplitter BS2 (uncoated ZnSe plate) reflects a part of the mid-IR radiation to the photodetector PD2 for continuous monitoring of IR energy.

The visible beam needed for SFG is the second harmonic of PL2143A/SS. To ensure a Gaussian profile of the 532nm beam, a lens (L3), a pinhole (PH) and another lens (L4) form a spatial filtration system. Half-wave plate HWP1 and HWP2 and a Glan prism GP1 allow optimization of the visible beam for the specific SFG experiment: polarization selection and continuous pulse energy tuning from minimum to maximum value.

To ensure the time overlap of 532 nm and mid-pulse beam, beamsplitter BS1 directs a part of the 532nm beam radiation to a photodiode PD1.

The SFG signal is directed to the signal monochromator by mirrors M14 and M15. A Glan prism (GP2) is used for the analysis of the SFG signal polarization as well as for scattered light rejection.

A monochromator filters the SFG signal and a photomultiplier tube (PMT) (Hamamatsu, R7899), having cathode sensitivity minimal of 70 μA/lm and typical of 119 μA/lm and a maximum anode to cathode voltage of 1250 Vdc, is used to detect it. All

system components are computer-controlled under LabVIEW software. Since this instrument was available at the very end of this thesis, not so many experiments have been performed with it.
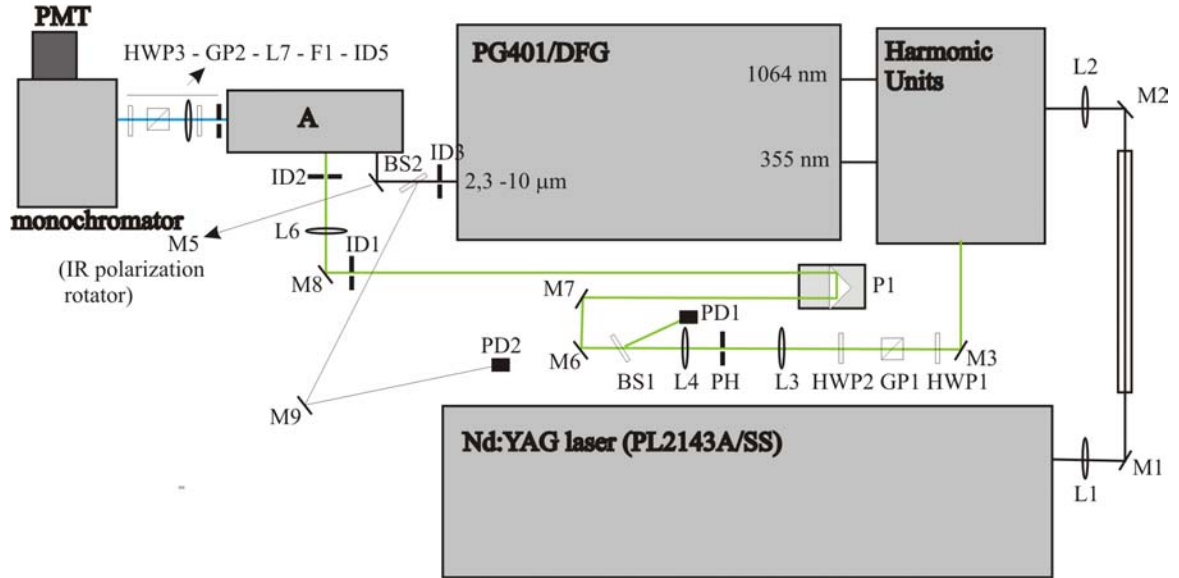
Figure 2.12   SFG spectrometer optical layout.
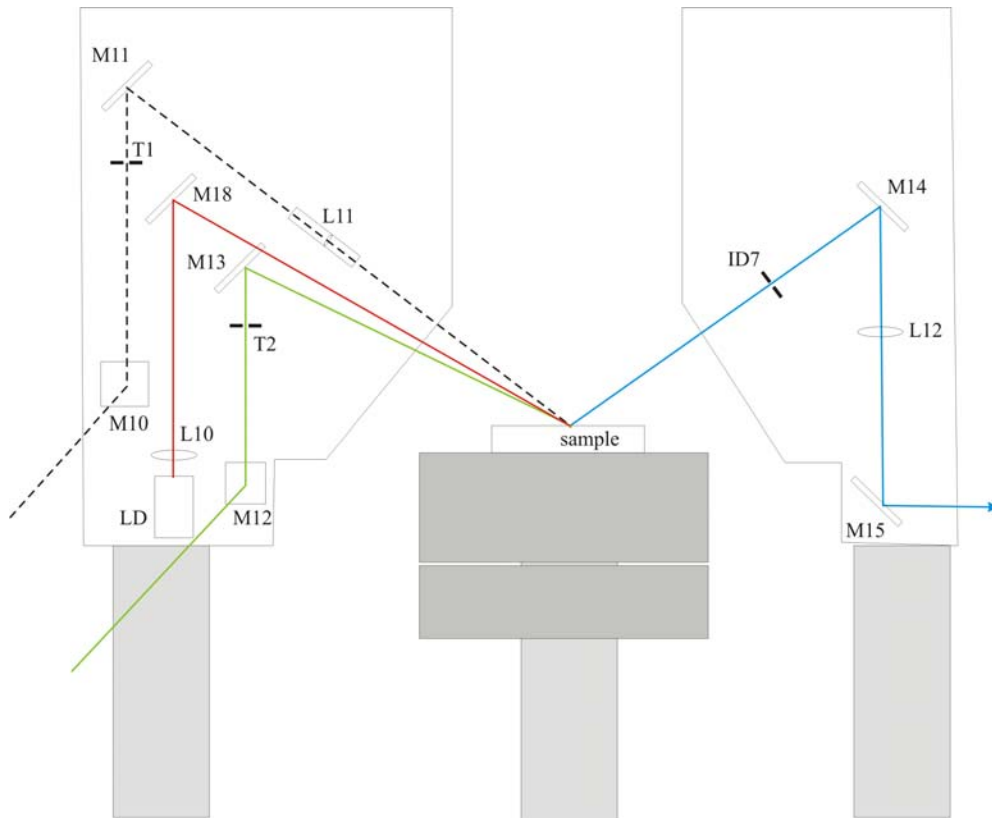
Figure 2.13   Side view of A area.

2.8. RESULTS AND DISCUSSION

Surface tension measurements

In order to check the quality and the purity of the solutions, a series of surface tension measurements has been taken for each chain length. The results obtained are showed in figure 2.14. From the curves, it is possible to observe an alternating effect in the slope of the curves, depending on the chain length.
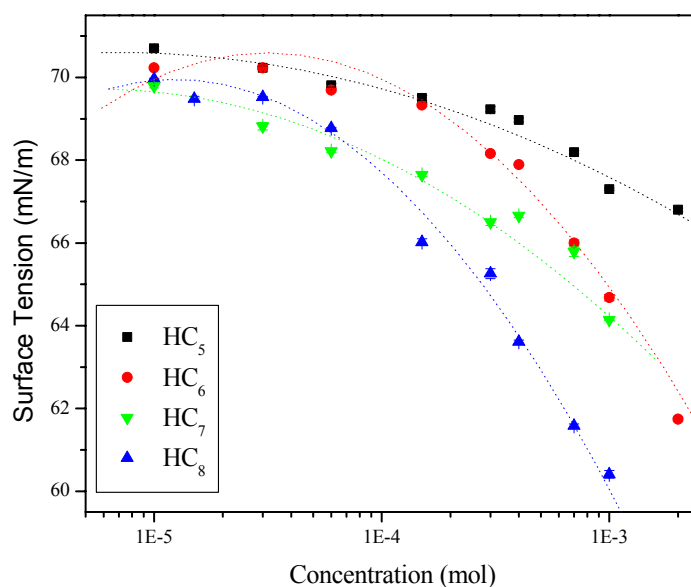
Figure 2.14 Equilibrium surface tension (σ_e) as a function of the concentration (c) isotherms of the homologous series of N-n-alkyl-4'-(dimethylamino)-stilbazium bromides HC*n* at 295K.

From these data, the derivative of the surface tension (σ_e) over the ln(concentration) has been plotted as a function of the bulk concentration, giving values proportional to the surface excess, according to equation 2.9. The curves obtained are presented in figure 2.15.

$$\Gamma \propto \frac{\partial \sigma_e}{\partial \ln c} \qquad (2.9)$$

From the curves obtained in figure 2.15, we took the value obtained for 1mmol and made a graph as a function of the carbon number, presented in figure 2.16. Thus, a odd-even effect is clearly visible.
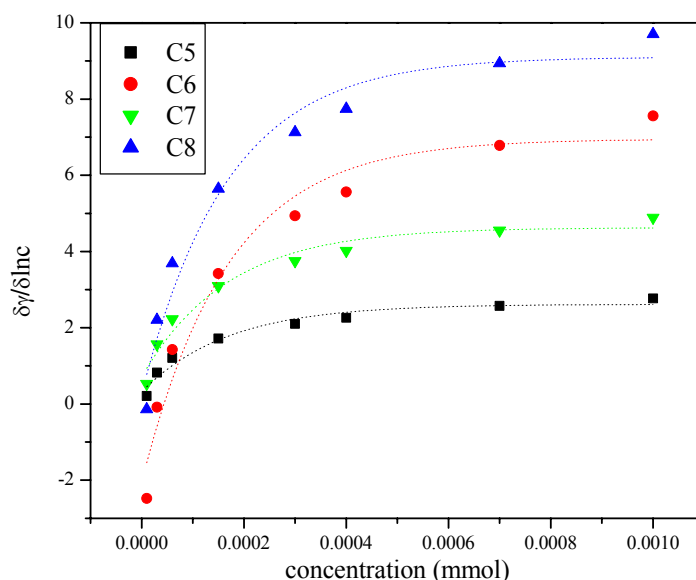
Figure 2.15 $\delta\sigma_e/\delta\ln c$ proportional to Γ as a function of the concentration (c) isotherms of the homologous series of N-n-alkyl-4'-(dimethylamino)-stilbazium bromides HC*n*
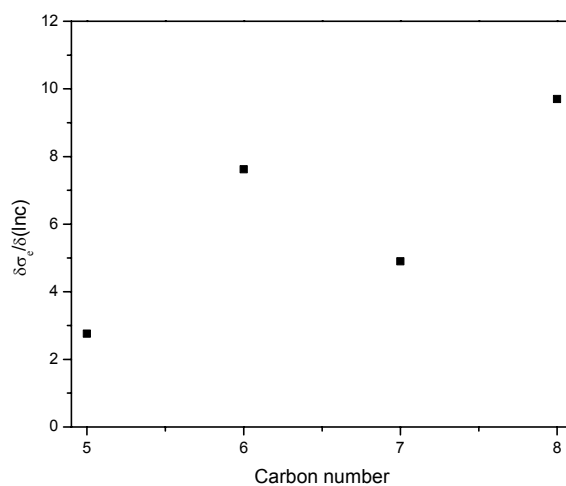
Figure 2.16 $\delta\sigma_e/\delta\ln c$ proportional to Γ as a function of the carbon number for 1mmol solutions of the homologous series of N-n-alkyl-4'-(dimethylamino)-stilbazium bromides HC*n*

The surface activity of the molecule depends on the chain length of the alkyl chain. Surprisingly the even chains possess a higher surface activity as compared to the odd chains. Usually, by increasing the hydrophobicity, we observe a monotonous behaviour; however, this is not the case here. In other words, C6 and C8 have a higher surface activity than C5 and C7.

UV-VIS measurements

Before performing SHG experiments on the system, some parameters have to be verified. The first problem that can arise and needs to be checked is the absorption of SH signal by the solution. An easy way to verify it is by measuring an UV-VIS spectrum of the solution.

As an example, a curve from a 15μmol HC_8 solution is presented in figure 2.17. The spectrum shows almost no absorption at 532nm and a small absorption at 266nm. We can then conclude that for the following experiment, performed in reflection mode, the absorption of the signal is not important enough to create any problem. Moreover, the remaining absorption at 532 nm provides the resonance enhancement of the signal. We therefore used the 532nm light as incident beam for the SSHG experiments. The same conclusion arose for the other chain lengths. There is no surface aggregation leading to a shift in the absorption spectra with increasing the concentration of the solution, such as – H or –J aggregates.
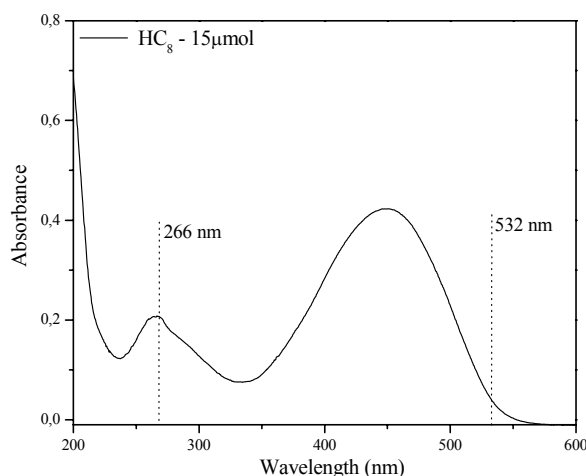
Figure 2.17   UV- spectrum of a 15 μmol HC_8 (1cm).

Stability of the SH signal

SSHG requires high power laser pulses that can create damage onto the sample. Therefore, the first step in the NLO characterization requires the determination of the surface damage-threshold. Usually, we work significantly below this value. Then, we crosscheck the degradation of the molecules by the laser beam over time. To do so, one simply looks at the intensity of the SH signal as a function of time. To get a clear answer to this question, we performed the experiment in two different ways. In one case, the beam was always hitting the surface at the same spot, because we let the Petri in a static position. In the second case we aligned the beam a little off from the center of the Petri, and we turned it clockwise while performing the measurement, in order to have the beam always hitting a fresh surface. The results for both situations are presented in figure 2.18.
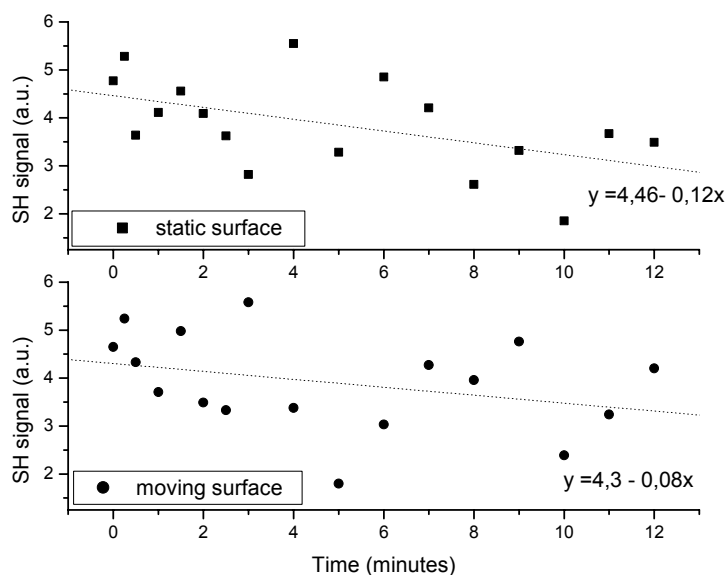
Figure 2.18   SH signal of a HC_5 solution (concentration) as a function of the time for static (■) and moving (●) surface.

The slope of the signal gives the degradation. As one can observe, there is no significant difference between the two situations; therefore we can let the solution standing in the beam, without moving it; this makes the experiment easier to accomplish. Moreover, one can conclude that there is only a very slight degradation happening at the

surface with time, but not important enough to take it into account in the time scale of our measurements.

Effect of the carbon number of the HC_n series on the SHG signal

The isotherms of the hemicyanine dye series have been measured with SSHG. The results obtained are presented on figure 2.19. It is important to note that the intensity of the incoming beam is different for each experiment; therefore, it is not possible to compare the isotherms between them in this sense.
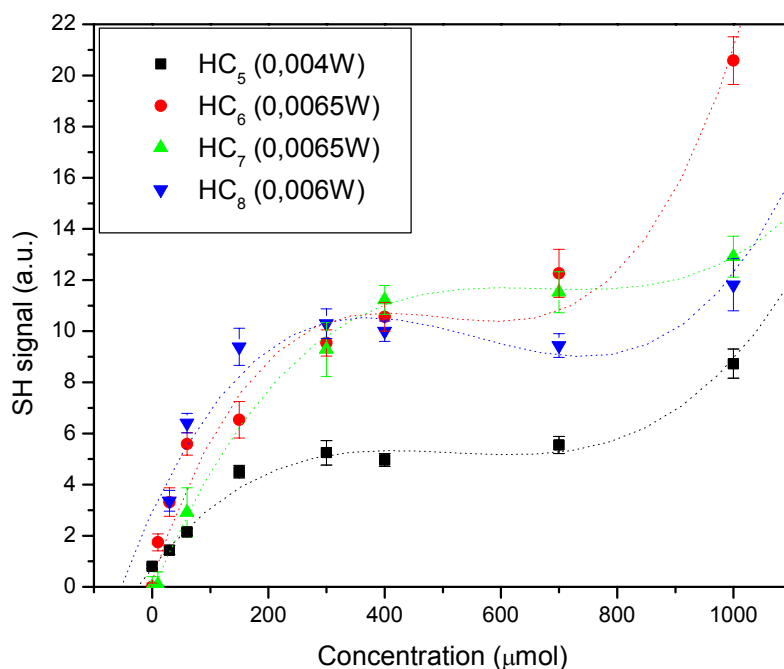
Figure 2.19   SHG isotherms of the hemicyanine dye series.

SSHG signal can directly be translated to the monolayer coverage for two different situations. The first case is when the mean orientation is close to the so-called magic angle, which occurs at around 39 degrees.[17] At this angle, SSHG is unable to determine the width of the orientation; therefore, we directly probe in a semi-quantitative way the surface coverage. The orientational analysis presented later demonstrates that it is the case. In this sense, we can interpret the SSHG signal as a mass coverage of the interface.

Secondly, according to the equation 1.20 and 1.21, SSHG probes directly the surface coverage if the monolayer orientation is independent of the surface coverage. Therefore,

$$N_s \propto \sqrt{I(2\omega)} \propto \Gamma_m \tag{2.10}$$

where N_s is the surface coverage, and $I(2\omega)$ the intensity of the SH signal. The results of N_s calculated from the curves obtained in figure 2.19 are presented in figure 2.20.
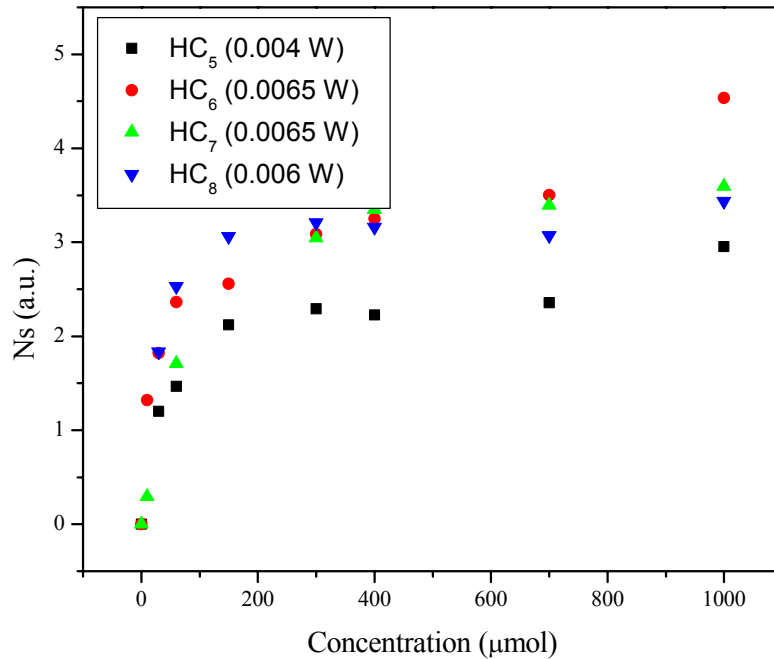
Figure 2.20   Ns ($\propto \Gamma_m$) isotherms for the hemicyanine dye series.

From the results obtained, we can conclude that all isotherms possess the same features. Moreover, an interesting observation comes from the fact that instead of reaching a plateau for the highest concentrations, N_s ($\propto \Gamma_m$) keeps increasing. Hence, we can conclude that with increasing concentration, the mass coverage of amphiphiles with polar order is increasing. This holds for every chain length.

Since the results presented in figure 2.19 and figure 2.20 have been obtained with different incoming beam intensities, we performed another series of experiments for fixed concentrations, at fixed intensity. The result is presented in figure 2.21.

N_s as a function of the carbon number is presented for 30 and 1000 μmol. An alternation in the intensity of the signal according to the number of carbons atoms in the chain is clearly noticeable. According to these results, N_s, proportional to Γ_m, is higher for the odd numbers.
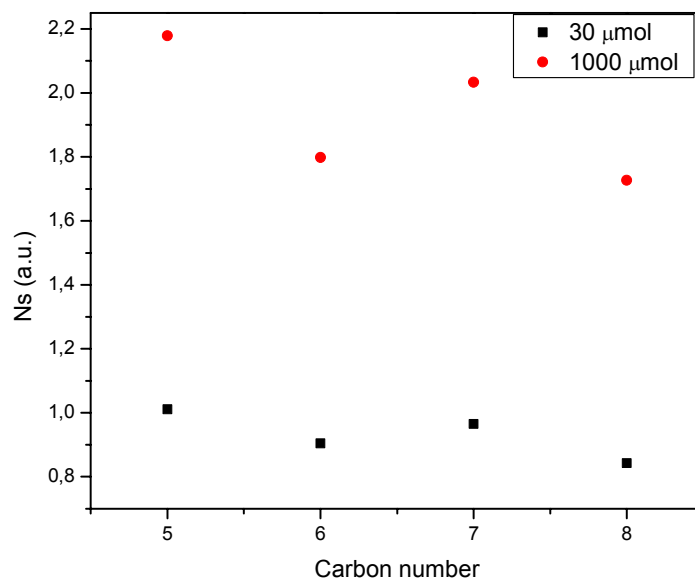
Figure 2.21   Ns ($\propto \Gamma_m$) as a function of the carbon number for low and high molecular concentration.

From these results, one can conclude that an odd-even effect is observed, however not understood. Therefore, orientation SSHG and IR-VIS SFG measurements have been performed. Moreover, the increase of the signal for higher bulk concentrations could arise from a molecular reorganization occurring at higher concentrations, leading to a higher surface coverage. In order to verify this hypothesis, ellipsometric measurements have been performed.

Effect of the carbon number of the HC$_n$ series onto the ellipsometric signal

Ellipsometric measurements have been performed on the series of hemicyanine dye. Ellipsometry measures the integral of the dielectric function across the interface. It is not sensitive to the polar order and it is in most cases proportional to the mass coverage at the

interface. The value of (Δ_0-Δ) as a function of the bulk concentration has been calculated for each sample. The result obtained is presented in figure 2.22.

The curves obtained for each chain length present unusual features. Usually, the increase of the bulk concentration would lead to the formation of a monolayer at the interface, thus creating a plateau after a certain concentration. As a consequence, the intensity of (Δ_0-Δ) would remain constant after a certain concentration. However, in this case, for every chain length, we observe an increase of the signal at higher concentrations.
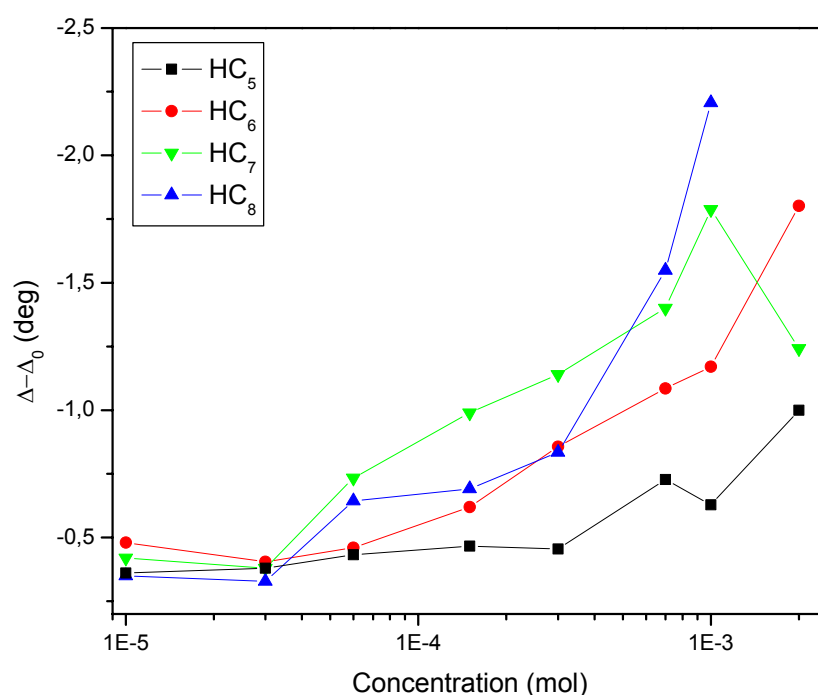
Figure 2.22 Ellipsometric measurements of (Δ_0-Δ) as a function of the bulk concentration for the hemicyanine dye series.

Since this value is proportional to Γ, this means that we observe an increase of the mass coverage. This is in very good agreement with the SSHG isotherms presented in the precedent section. The only exception to this observation is the highest concentration (2mmol) of the HC_7 solution.

Observation with the BAM allowed understanding this sudden diminution of the signal for that concentration. A BAM image taken from the 2 mmol HC_7 solution is presented in figure 2.23.
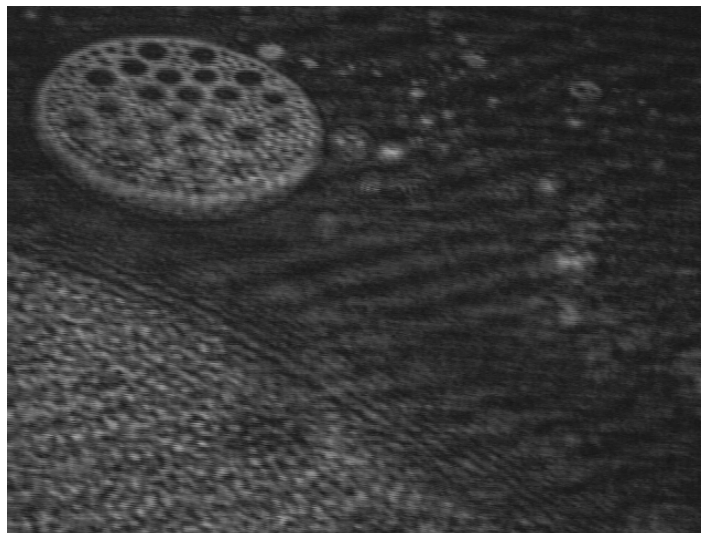
Figure 2.23   BAM image taken from a 2 mmol HC_7 solution.

For this solution, one clearly observes inhomogeneities in the form of 2D foams at the air-water interface. All the other solutions presented a homogeneous surface, without any aggregate. Therefore, we can conclude that we reached the solubility limit of this compound. As a result, all experiments performed with this concentration have been rejected.

Evidence for an organized interfacial architecture

The surface tension isotherms obtained for all chain lengths do not show any strange behaviour. In fact, the surface tension measurement is very sensitive to the interaction of the first molecular layer with water. For this reason, it is possible that interfacial structures built under or over the monolayer in contact with water are not visible in the isotherms. The same happens with the π-A isotherm taken with the Langmuir through, as it is shown in the literature[18].

Surface tension isotherms do not present any hint for an organized interfacial architecture other than a monolayer, however SSHG and ellipsometric measurements

clearly provide evidence for build up of a multilayer. SSHG is probing the polar order part whereas ellipsometric probes the surface coverage independently to the polar order. We observe a constant increase of the signal with the bulk concentration; we can therefore conclude for a molecular interfacial reorganization containing more than a monolayer. The possible interfacial molecular organizations are presented in figure 2.24.
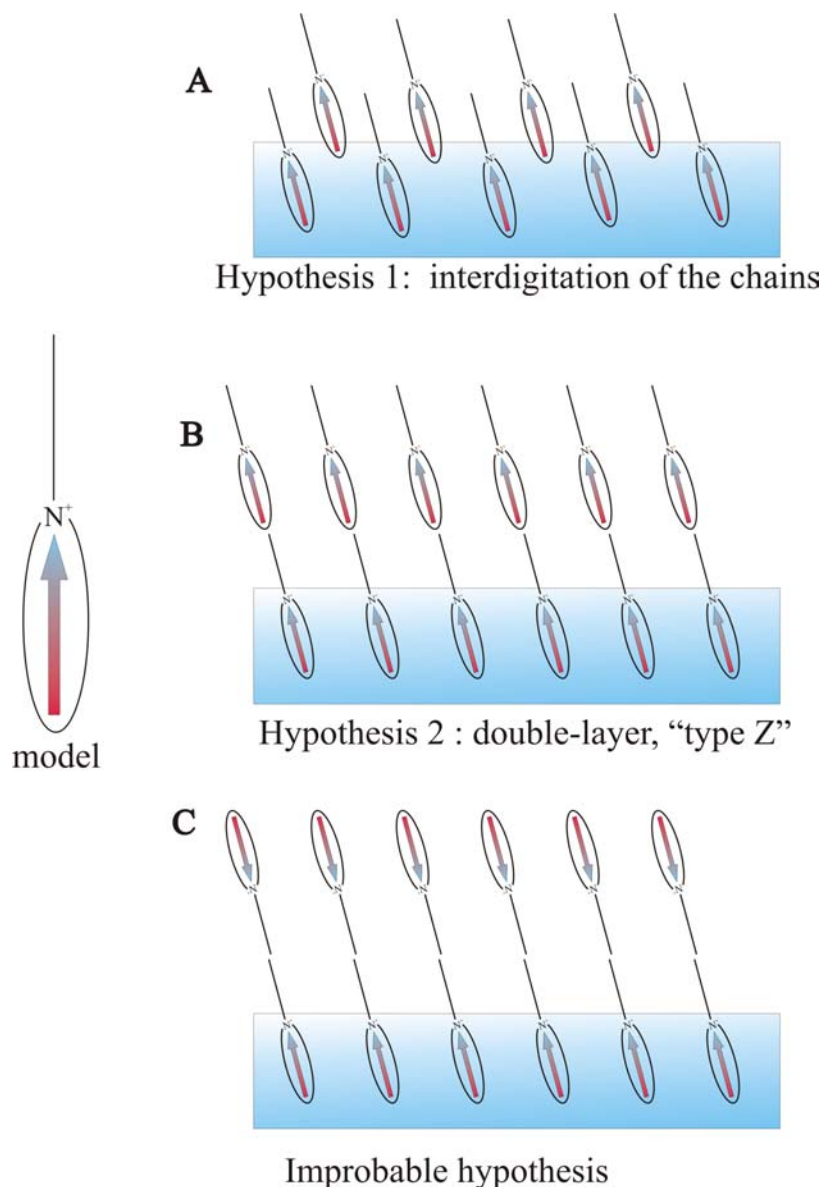
Figure 2.24   Possible interfacial organizations for the HC*n* solutions.

From these three hypotheses, one can be discriminated, due to the results obtained with SSHG. SSHG occurs only when the symmetry of a system is broken. In the case of

figure 2.24 C, the dipoles of the molecules are oppositely aligned. This creates a symmetry in which each dipole cancels its neighbour. Having this situation, the SH signal would diminish or even vanish. Since the observed signal is increasing, we can discard this possibility.

The two other hypotheses are presented in figure 2.24 A and B. We can see in the first case an interdigitation of the chains, and in the second, the building of a double-layer, that can be compared to Z-type layers from Langmuir-Blodgett films.

The case oz Z-type layers occurs when we are in presence of a weak polar group or when it is not so hydrophilic[5]. In our case, we are in presence of a $-N(CH_3)_2$ group, which is not very hydrophilic. In both situations (weak polar group and low hydrophilicity), interactions between adjacent monolayers are hydrophilic-hydrophobic, and therefore this multilayer is less stable than in the situation C, for instance. On the other hand, it creates a noncentrosymmetric system, leading to a high SH signal. However, if we would be in the presence of a perfect Z-type layering, the SH signal would become 4 times higher than for a monolayer. In our case, we observe an increase of the signal, but no so high. Therefore, it would be difficult to believe that we are in presence of a perfect double-layer system.

Moreover, the chain length is rather short. In the case of the insoluble system, chains are rigid and the building of an organized double-layer is easier as it is in the case of soluble system. For these reasons, the situation presented in figure 2.24A represents the most consistent and the most probable one. Since the signal increases slightly at higher concentrations, we conclude to a formation of a second layer, however not completely organized.

Furthermore, if we look at the structure of the molecule, we observe that the alkyl chain would have a surface area of around 20 Å^2 whereas the stilbene head would have a bigger surface area, approximately of 40 Å^2. That leaves a lot of space between the molecules forming the interfacial monolayer for the formation of a second interdigitated layer. In order to further prove these conclusions, we could look at the thickness of the interfacial layer. This could be done with careful measurements with X-ray diffraction or neutron reflectivity. Nevertheless, the IR-VIS SFG analysis might bring further answers to this interrogation.

Effect of the carbon number on the orientation of the HC_n series at the air-water interface

To characterize the orientation of the surfactants at the air-water interface, we performed orientation-SSHG experiments. The results obtained for 2 concentrations (30 mmol and 1 mmol) of the hemicyanine series are presented in figure 2.25 and table 2.1.
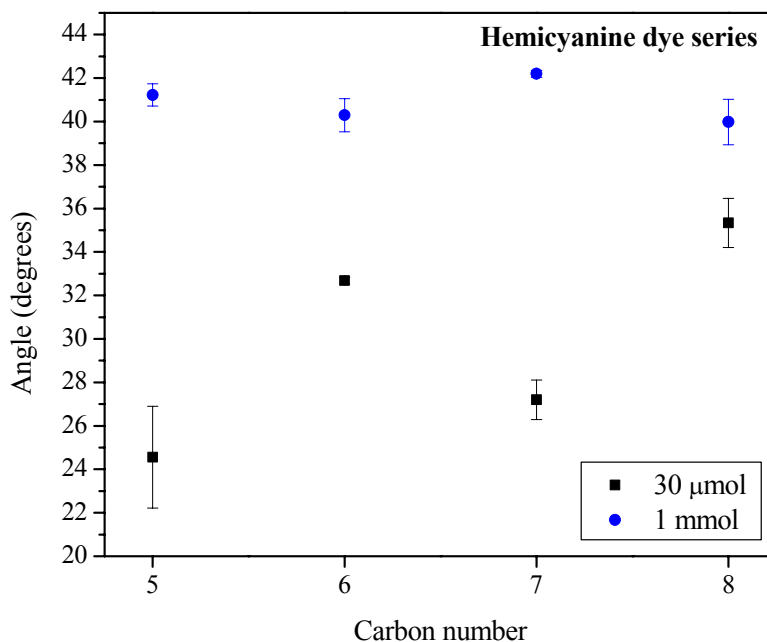
Figure 2.25   Molecular orientation as a function of the carbon number for low and high concentration.

Chain length	Molecular orientation (degrees)	
	30 μmol	*1 mmol*
5	24,5 ± 2,3	41,2 ± 0,5
6	32,7 ± 0,1	40, 3 ± 0,7
7	27,1 ± 0,9	42,2 ± 0,2
8	35,3 ± 1,1	39,9 ± 1,0

Table 2.1   Data compiled from figure 2.25

For low concentration, we observe an alternating effect in the angle θ. The values for the even members of the series are 24-27 degrees whereas for the odd members it is more 33-35 degrees. The difference is however not very important.

In the case of higher concentrations, we see that all the chain lengths possess a similar orientation angle θ, that is around 40 degrees. Unfortunately, this experimental value is very difficult to analyse. Being close to the magic angle, the orientational analysis does not provide any insights in the width of the distribution. It can be that most of the molecules have an angle θ of 40 degrees. Nevertheless, it is also possible that the distribution is very broad and that the angle of orientation varies from 0 to 90 degrees with respect to the normal. Of course, the molecules can also behave in any in between situation, as presented in figure 2.26.
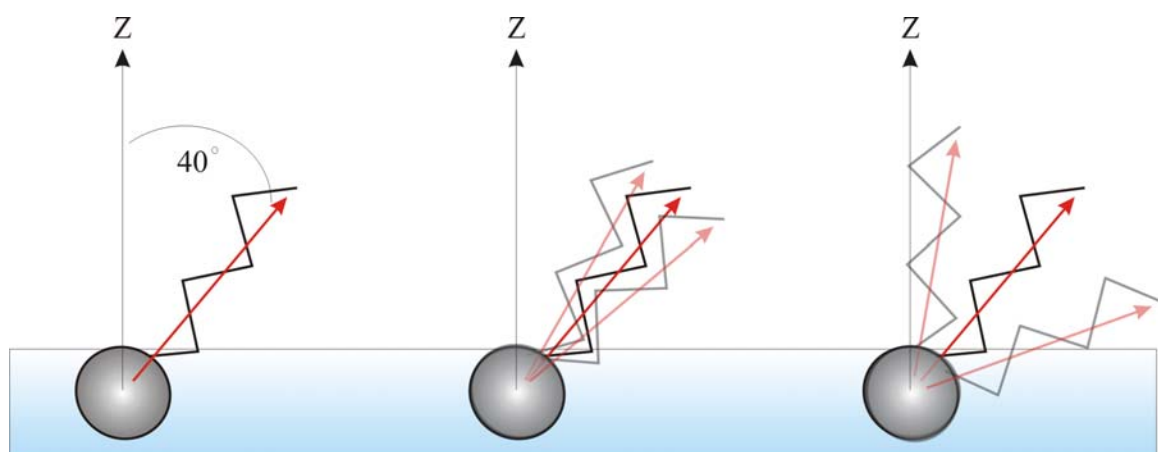
Figure 2.26   Possible angle distributions for the HC_n series at high concentration.

For this reason, we decided to perform a surface sum-frequency generation analysis of the surface. The results obtained are presented in the following sections.

FTIR analysis

In order to perform surface SFG experiments, we need to find out which bands will be utilized. To do so, we performed an infrared spectrum onto the different chain length substances. All presented similar spectra; therefore, as an example, figure 2.27 and figure 2.28 show infrared spectra of HC_8 for the regions of interest. On one hand, we are interested in the orientation of the molecule at the air-water interface, we need to study the intensity of the peaks associated with the stilbene moiety of the molecule. Moreover, to verify the alkyl chain conformation, we need to look at the bands associated to the – CH_3 and $-CH_2$ elongations, which are present in a different region of the infrared spectrum. This is presented in figure 2.28.

Assignments of the peaks associated to the stilbene vibrations for the region of interest are presented in the table 2.2. As one can observe, all peaks are related to the stretching vibrations of the rings constituting the stilbene moiety. Moreover, table 2.3 presents the description of the assignments associated to the $-CH_3$ and $-CH_2$ elongations. These bands will be described in greater details in the next section.
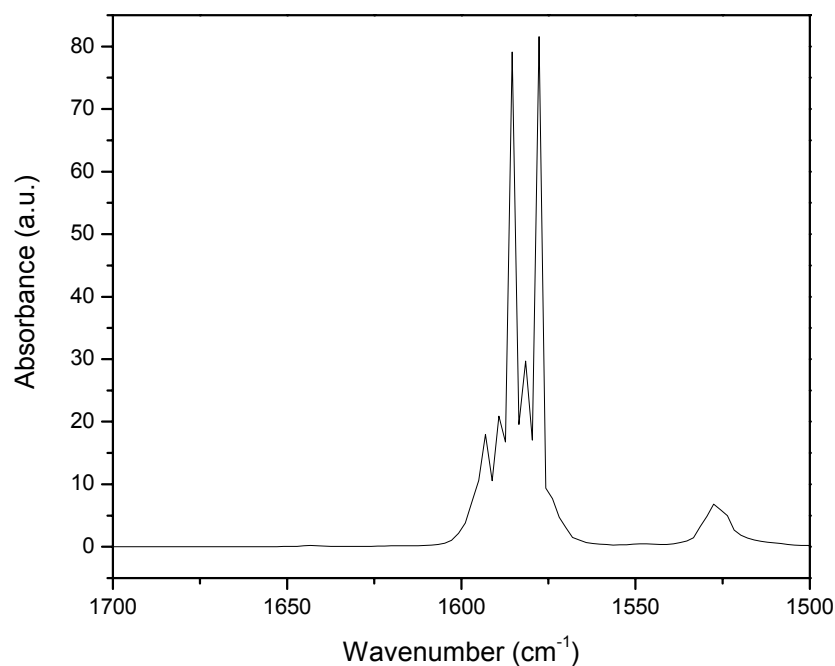
Figure 2.27   Infrared spectrum of HC_8 (KBr pellet) for the mid-frequency region.

Peak position (cm-1)	Intensity	Assignment
1593	sh, w	-C-H and ring C=C str.vib.
1589	w	=C-H and ring C=C str.vib.
1585	sh, s	Skeletal vibration ring (C-C stretching)
1578-1581	sh, m	Ring stretching vibration, parasubst. Pyridine
1527	br, w	=C-H and ring C=C stretching vibration

Absorption: **s** – *strong*, **m** – *medium*, **w** – *weak*, **sh** – *sharp*, **br** – *broad*.

Table 2.2   IR vibration assignments in the mid-frequency region for HC_8
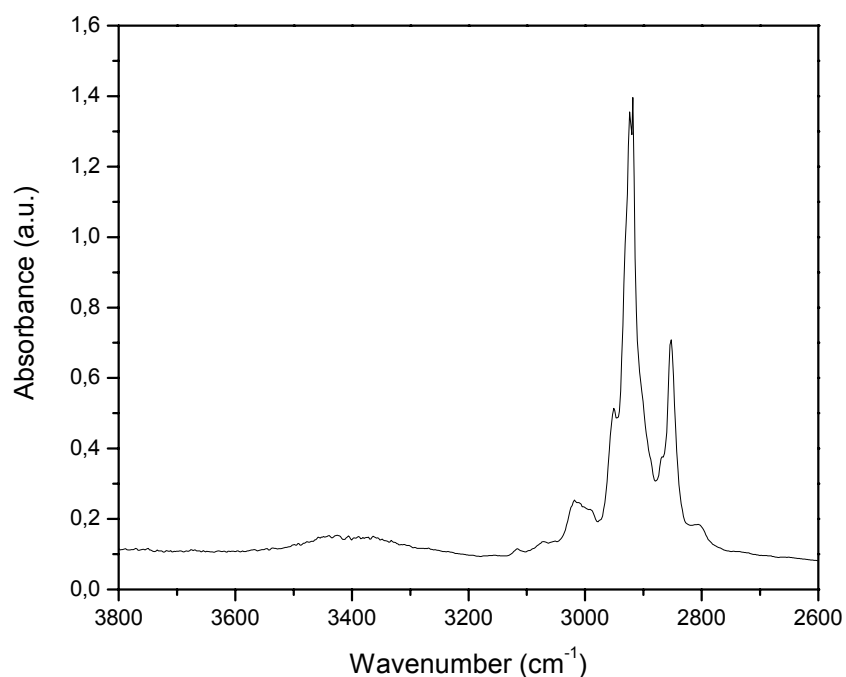
Figure 2.28   Infrared spectrum of HC_8 (KBr pellet) for the high frequency region.

Peak position (cm-1)	Intensity	Assignment
3430-3380	br, w	-OH elongation, water
2951	shoulder, w	$-CH_3$ r- out of plane
2922	sh, s	$-CH_2$ d- sym stretch
2870	shoulder, w	$-CH_3$ r+ in plane
2852	sh,s	$-CH_2$ d+ asym stretch

Absorption: **s** – *strong*, **m** – *medium*, **w** – *weak*, **sh** – *sharp*, **br** – *broad*.

Table 2.3   IR vibration assignments in the high frequency region for HC_8

Description of the chain conformation at the air-water interface by IR-VIS SFG measurements

The generation of an SFG signal requires an asymmetric environment both on a macroscopic and a microscopic scale. The asymmetry in the macroscopic scale is the result of the polar arrangement of the amphiphiles at the air-water interface. On a microscopic scale, we must consider the local contributions of the different chemical groups onto the hyperpolarisability β.

In the frequency-window corresponding to alkyl chains in a normal FTIR spectrum (see preceding section), the spectral signature is determined by the methyl ($-CH_3$) and the methylene ($-CH_2$) stretching modes. The methyl group, being a terminating group, is in general contributing to the SFG spectrum. The situation is different for the methylene group. An all-trans chain provides local inversion symmetry leading to a cancellation of β for these modes.[19,20] The rotational barrier of alkyl chains is not too different from the thermal energy kT. Hence, gauche-defects can occur, breaking this local symmetry. In this situation, the stretching modes of the methylene groups contribute to the SFG spectrum. The intensity of the associated bands is increasing with the increase of the presence of gauche-defects.

As it is schematised in figure 2.29, in the situation A, the methylene groups are symmetrically opposed; therefore, the signal vanishes. However, it is clear the in the situation B, the presence of the gauche defect breaks the symmetry of the system; hence, the methylene groups give a signal. This is a very interesting property for studying order in the alkyl chains and their conformation at the air-water interface.
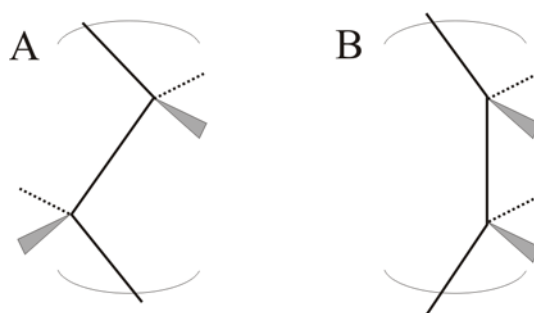
Figure 2.29   Scheme of the methylene groups position in the case of **A**. normal alkyl chain and **B**. alkyl chain having a gauche defect.

In order to understand a better way, a complete description of all the possible situations is presented in the following pages. First, we identify the peaks that can be present in an IR-VIS SFG spectrum of the alkyl chains at the air-water interface. This is presented in Table 2.4. Then, Figure 2.30 describes schematically and semi-qualitatively the different chain conformations at the interface together with the expected spectra.

CHEMICAL ASSIGNMENT	NOTATION	POSITION OF THE BAND (cm^{-1})
-CH$_3$ (methyl)		
Symmetric stretching (ν_s)	**r$^+$**	~ 2875
Fermi band (ν_{FE})	**r$_{FE}$**	~ 2900-2930
Asymmetric stretching (ν_a)	**r$^-$**	~ 2960
-CH$_2$ (methylene)		
Asymmetric stretching (ν_s)	**d$^+$**	~ 2850
Fermi band (ν_{FE})	**d$_{FE}$**	~ 2890-2930
Asymmetric stretching (ν_a)	**d$^-$**	~ 2915

Table 2.4   IR vibration assignments of all the possible peaks present in an IR-VIS SFG spectrum of the alkyl-chain region.

Table 2.4 presents the different assignments associated to the methyl and the methylene group. If we are in the presence of a perfect monolayer having no gauche defect, the peaks associated to the methyl group, r$^+$, r$_{FE}$ and r$^-$ are clearly identifiable. Figure 2.30A presents schematically this situation. The r$^+$ and r$^-$ bands come from the symmetric and asymmetric stretching modes of the –CH$_3$ group. The r$_{FE}$ band comes from a Fermi resonance of the –CH$_3$ stretch and overtone of a -CH$_3$ bending mode.[20] This represents of course the situation where the monolayer at the air-water interface possesses a perfect packing, having no defect.

If the monolayer presents some defects, as it is pictured in figure 2.30B (the gauche defects being highlighted by orange circles), we observe on the SF spectrum the appearance of peaks related to the methylene groups. The d$^+$ and d$^-$ bands come from the symmetric and asymmetric stretching modes of the –CH$_2$ group. However, the d$^-$ band is usually not seen since it is hidden by the Fermi band, d$_{FE}$, which comes from the Fermi

resonance of the $-CH_2$ stretch and overtone of a $-CH_2$ bending mode.[20] Since the quantity of gauche defects is rather small, the intensity of the bands coming from the $-CH_3$ modes are still more intense than the one coming from the $-CH_2$. The ratio of the intensities between the d+ and r+ bands is a good way of determine in a semi-quantitative way the number of gauche defects in the system.
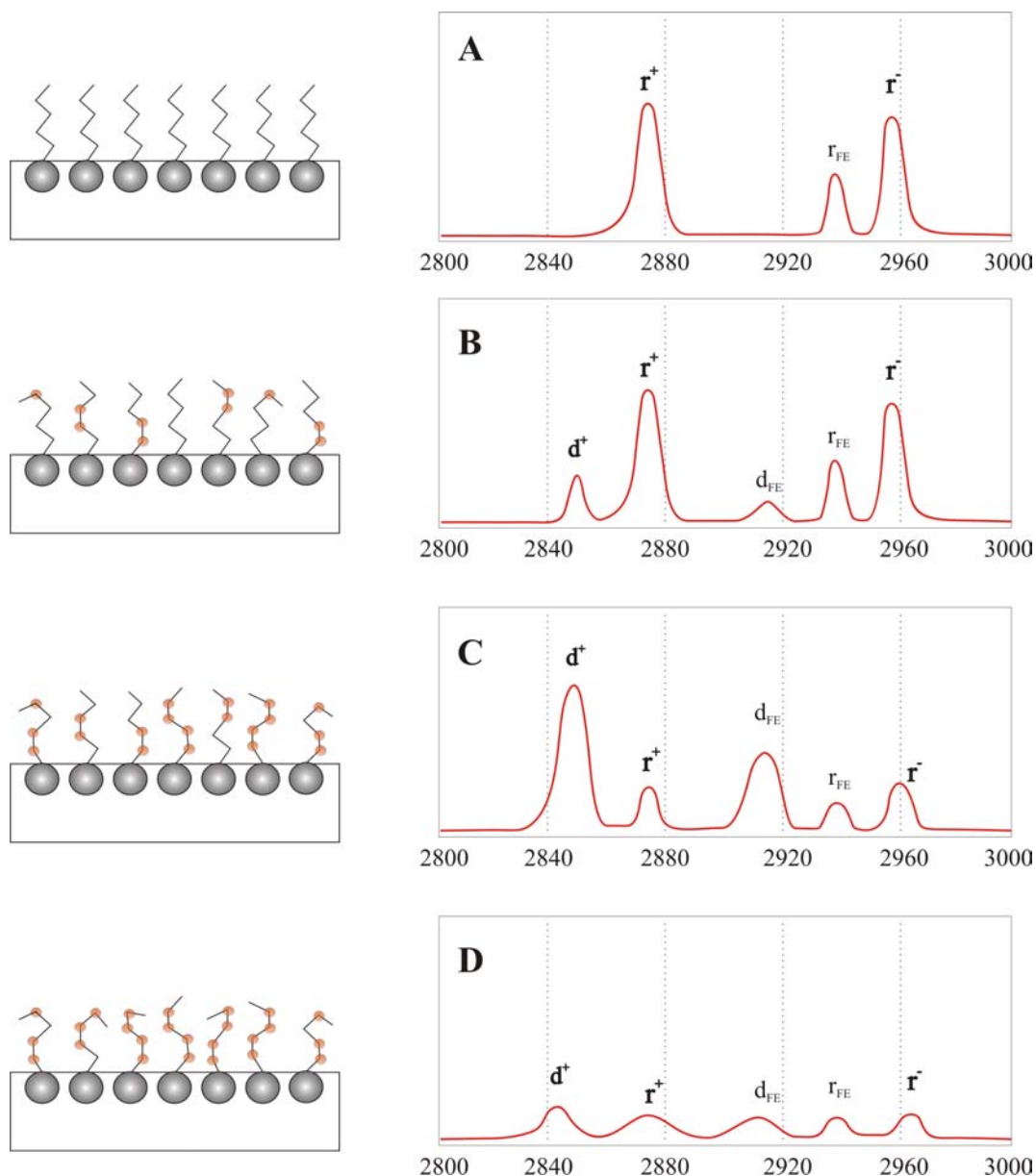
Figure 2.30 Molecular and spectral description of the possible conformations of alkyl chains at the air-water interface.

As the quantity of gauche defects increases, we observe a decrease of the signals coming from the $-CH_3$ bands and an increase of the one coming from the $-CH_2$ bands.

This is presented in figure 2.30C. Finally, when we reach a state where the quantity of gauche defects is too important, the chains adopt a fluid-like state, there is no order anymore and therefore all the peaks possess a very small or even vanishing intensity. This is an extreme situation, and it is pictured in Figure 2.30D.

Having this model in mind, we can now describe the experimental results obtained for the different chain lengths. In order to analyse in a proper way the spectra, one has to look first for the relative intensities of the different frequency-windows of the spectrum. Therefore, we present in figure 2.31 the IR-VIS SFG spectra of the stilbene region of every chain length, for two different concentrations, as well as for two different polarizations. Figure 2.32 presents the IR-VIS SFG spectra of the alkyl chain region for solutions of 1mmol and –ppp polarization, for every chain length.
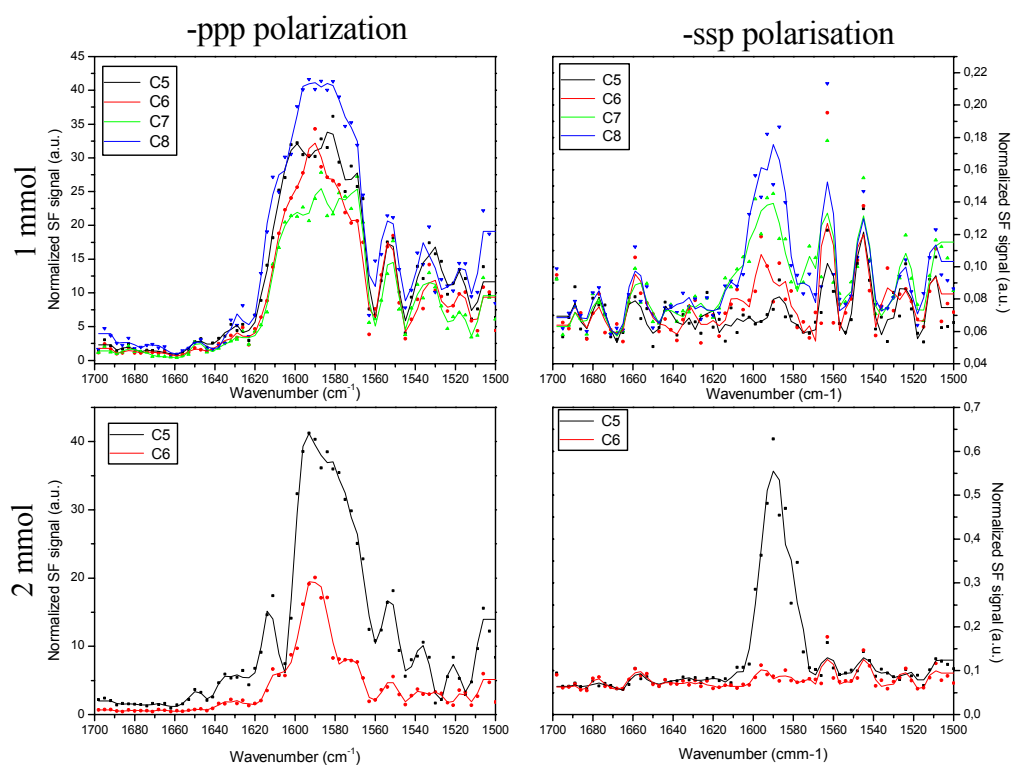
Figure 2.31   IR-VIS SFG spectra of the stilbene region of the different chain lengths of the hemicyanine dye series (1 mmol solutions) and different polarizations.

In figure 2.31, we observe the spectra from 1400cm^{-1} to 1600 cm^{-1}. The SFG spectra show an unusual high intensity. This is due to a double-resonant enhancement between

stretching modes and the electronic transitions. A further quantification would require a detail analysis of the Raman cross-section of all individual modes in this region. This defines also the intensity level which we can expect from the corresponding SFG alkyl stetching modes. The corresponding spectra for the alkyl chain region are presented in figure 2.32.
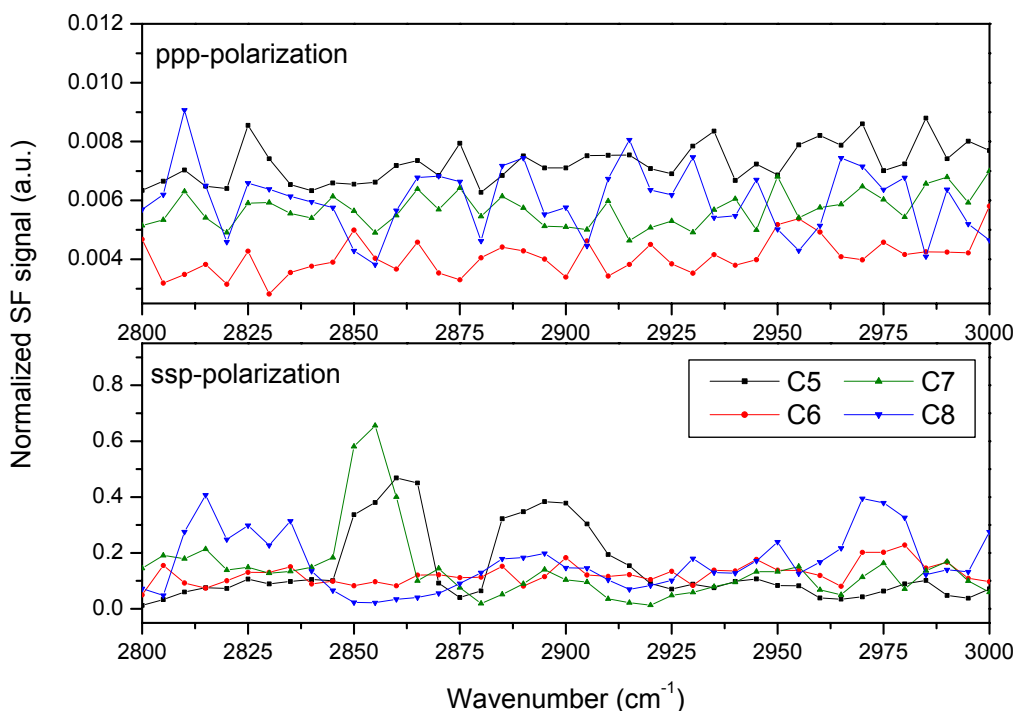
Figure 2.32   IR-VIS SFG spectra of the alkyl region of the different chain lengths of the hemicyanine dye series (1 mmol solutions) and ppp polarization.

The data in the mid-frequency range clearly proves that our SFG setup is working properly. Meanwhile, quite a few samples have been analysed in the alkyl stretching-mode. The corresponding spectra showed in figure 2.31 present only random noises. This means that there is no order in the alkyl chains. The result is then the presence of a complete fluid-state. This is in good agreement with the literature; it was reported that by shortening the alkyl chain of the monolayers, one observes an increase in defects concentration.[21,22]

2.9. CONCLUSION

The interfacial structural properties of a hemicyanine dye series have been elucidated by means of nonlinear optical techniques. The combination of the different techniques used allowed describing the structural organisation as well as the molecular orientation at the interface.

The results obtained from SSHG and ellipsometric measurements show that for the series of HC_n, for $n = 5-8$, a formation of an interdigitated layers-system occurs at the air-water interface for higher concentrations. A BAM experiment also demonstrated that when we reach the solubility limit of the hemicyanine dye, an aggregation giving raise to 2D foam structures at the air-water interface occurs.

Orientation SSHG demonstrated that for high concentration, the average orientation angle is approximately 40 degrees. This value is problematic in the sense that we cannot describe the width of the distribution of the orientation. The pump-probe experiment, presented in chapter 4, could solve this problem.

IR-VIS SFG demonstrated that the chains are in a complete unorganized fluid-like state, for every chain length. This conclusion makes sense, since the chains are rather short.

This structure investigation leaves some questions opened, nevertheless, it is sufficiently characterised to perform the subsequent dynamic orientation experiments.

REFERENCES

1. Loew, L. M., Hassner, L.S.A., Alexanian, V. *J. Am. Chem. Soc.* **1979**, *101*, 5439.

2. Ephardt, H., Fromherz, P. *J. Phys. Chem.* **1989**, *93*, 7717.

3. Ephardt, H., Fromherz, P. *J. Phys. Chem.* **1993**, *97*, 4540.

4. Lunkenheimer, K., Laschewsky, A. *Prog. Colloid Polymer Sci.* **1992**, *89*, 239.

5. Ulman, A. *An introduction to ultrathin organic films from Langmuir-Blodgett to self-assembly.*; Academic Press, inc.: San Diego, 1991.

6. Gaines, G. L. *Insoluble monolayers at liquid-gas interfaces*; Interscience Publishers: London, 1966.

7. Rosen, M. J. *Surfactants and Interfacial Phenomena, second edition*; John Wiley & Sons: New-York, 1989.

8. Chattorajm D.K., B., K.S. *Adsorption and the Gibbs surface excess*; Plenum Press: New-York, 1984.

9. Azzam, R. M. A., Bashara, N.M. *Ellipsometry and Polarized light*; Elsevier Science Pub Co: Amsterdam, 1987.

10. Lekner, J. *Theory of Reflection*; Martinus Nijhoff Publishers: Boston, 1987.

11. Möbius, D. *Current Opinion in Colloid & Interface Science* **1996**, *1*, 250.

12. Bain, C. B. *Current Opinion in Colloid & Interface Science* **1998**, *3*, 287.

13. Motschmann, H., Stamm, M., Toprakcioglu, C. *Macromolecules* **1991**, *24*.

14. Hutchison, H., Klenerman, S., Manning-Benson, S., Bain, C. *Langmuir* **1999**, *15*.

15. Lupo, D., Prass, W., Scheunemann, U., Laschewsky, A. *J. Opt. Soc. Am. B* **1988**, *35*, 300.

16. Phillips, A. P. *J. Org. Chem.* **1949**, *14*, 302.

17. Simpson, G. J., Rowlen, K.L. *JACS* **1999**, *121*, 2635.

18. Harke, M., Ibn-Elhaj, M., Möhwald, H., Motschmann, H. *Phys. Rev. E* **1998**, *57*, 1806.

19. Ward, R. N., Duffy, D.C., Davies, P.B., Bain, C.D. *J. Phys. Chem.* **1994**, *98*, 8536.

20. Guyot-Sionnest, P., Hunt, J.H., Shen, Y.R. *Phys. Rev. Lett.* **1987**, *59*, 1597.

21.   Hoffmann, H., Mayer, U., Krischanitz, A. *Langmuir* **1995**, *11*.

22.   Lagutchev, A. S., Song, K.J., Huang, J.Y., Kang, P.K., Chuang, T.J. *Chem. Phys.* **1997**, *226*, 337.

CHAPTER 3

SURFACE SHG COMBINED WITH THE OSCILLATING-BUBBLE TECHNIQUE: ON FOAM RHEOLOGY

Many technological processes in detergent and brewing industry as well as in sewage disposal require the formation of foams of a definite lifetime. Nuclear waste decontamination is based on formation of foam and its breaking. Moreover, some fire extinguishers utilize foams. The knowledge of the physicochemical properties of foams, especially factors that influence their stability, is very important for the process control. A foam lamella is a thin water slab stabilised by surfactant layers; it is a fragile system and its response to mechanical disturbance is of utmost importance. In the past, research has been performed to get a better understanding of these phenomena, but several fundamental aspects remain unclear: for instance, stability of foams is still not yet resolved. It has been proven that foam stability depends on various parameters among which the type of the added surfactant and the surface rheological properties of adsorption layers played the most important role[1-3].

The stability or instability of foams and emulsions is mostly determined by the surface rheological properties of adsorption layers at liquid interfaces. Nevertheless, because of lack of reliable data, a comprehensive investigation of this problem is not yet possible.

The combination of SSHG with the oscillating bubble technique (OB-SSHG) has been achieved in order to gain information about the exchange dynamics of adsorbed and dissolved surfactants at the air–water interface[4]. The oscillating bubble technique generates a non-equilibrium state by periodic compression-expansion cycles of the surface layer. The state of the adsorption layer is then investigated in situ by SSHG. Comparing the results obtained from elastic and viscoelastic systems helps to gain a better comprehension of foam stability.

3.1   SURFACE RHEOLOGY

If we have a system at equilibrium, for instance, soluble surfactants in water, a certain quantity of molecules adsorb at the interface, creating the so-called Gibbs monolayer, while another fraction will remain solubilized in the bulk. Bulk and surface layer are in equilibrium with a constant exchange of adsorbed and dissolved species. As long as the system remains untouched, equilibrium prevails. Such a system is presented in figure 3.1.
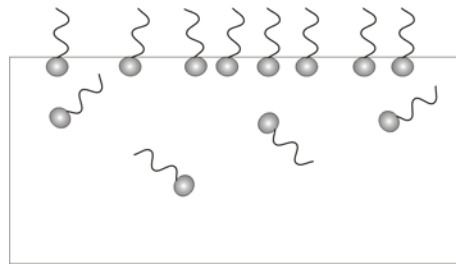
Figure 3.1   Soluble surfactants in equilibrium state.

An excellent way to gain new information about the system is to force it into a non-equilibrium state and to monitor the relaxation processes. For instance, when creating an expansion-compression cycle of the surface, as depicted in figure 3.2, the system responds in order to restore the equilibrium coverage. Upon compression, molecules must desorb whereas upon expansion, they move back to the surface.
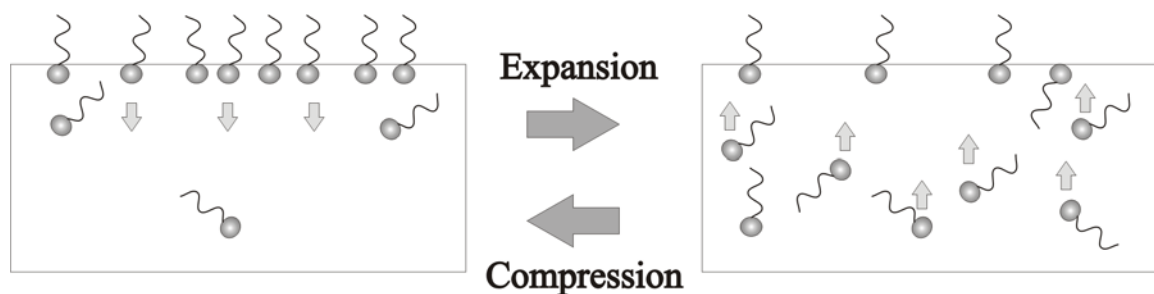
Figure 3.2   System response to external disturbance creating non-equilibrium state.

Understanding the underlying processes of such phenomena is the heart of surface rheology. These data are extremely important for basic sciences and technological processes.

For instance, microfluidics is a rapidly developing field which has moved into the focus of various technological applications, ranging from pharmaceutical, medical and biological to printing processes. The manipulation of ordered foams and emulsion structures in specific and confined geometry requires an understanding of the viscous dissipation occurring between the foam or emulsion and the channel[5], another important parameter of surface rheology.

In the case of coating processes, understanding the surface rheology, and more precisely the intrinsic surface viscosity is crucial to maintain the stability in high-speed coating processes as well as to understand how the surfactant stabilizes the liquid bridge against oscillations[6].

In the context of foams, one has to distinguish between foam formation and foam stability. Foam formation can be successfully related to a fundamental parameter of the aqueous surfactant system. Engels et al[7] demonstrated that the rate of foam formation of many amphiphiles can be linked to the relative dynamic surface pressure. Figure 3.3, taken from their publication, presents the linear relation between both quantities. On the other hand, foam stability could not be yet related to a fundamental parameter. Nevertheless, our preliminary investigations indicate a relationship between the foam stability and surface dilatational modulus[8].
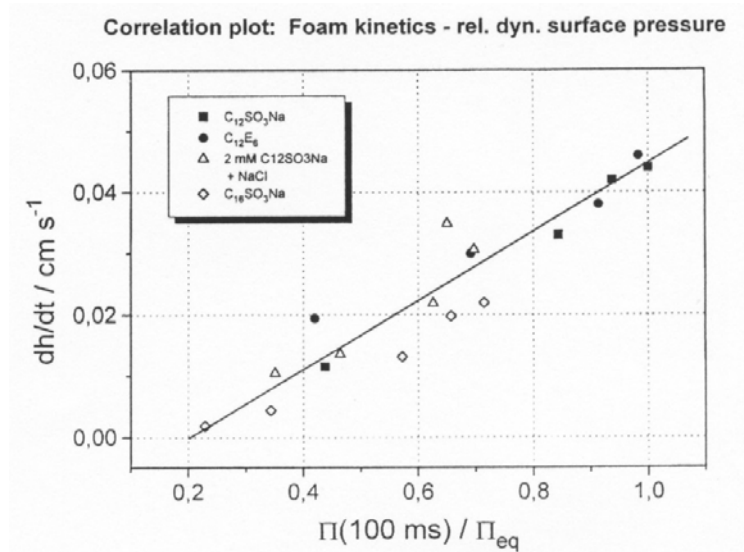
Figure 3.3   Correlation plot between foam formation and relative dynamic surface pressure.

3.2. SURFACE ELASTICITY

The adsorption of molecules at the interface changes the surface tension. The difference between the surface tension of film covered and pure water can be interpreted as a surface pressure Π [N/m]:

$$\Pi = \sigma_{H_2O} - \sigma_{film} \qquad (3.1)$$

Soluble surfactants adsorb at the interface and are in equilibrium with the bulk. According to Gibbs, the surface excess Γ [g/m^2] is proportional to the derivative of the equilibrium surface tension isotherm with respect to the logarithm of the bulk concentration c.

$$\Gamma \propto \frac{\partial \sigma_e}{\partial \ln c} \qquad (3.2)$$

Thus, the surface elastic modulus E is defined in analogy to the corresponding bulk quantity as the change in the surface pressure Π upon a relative area change $\delta A/A$. Essentially, it measures the ability of a system to adjust its surface tension upon stress.

$$E = -A\frac{\partial \Pi}{\partial A} = -\Gamma\frac{\partial \Pi}{\partial \Gamma} \qquad (3.3)$$

This relation holds because

$$\Gamma \propto \frac{1}{A} \qquad (3.4)$$

The modulus can be a complex quantity. If the surface layer is exposed to harmonic perturbation, a time-shift can occur between the system response and the applied disturbance. If the phase-shift vanishes completely at higher frequencies, the system is completely elastic. However, if there is a delay between the disturbance and the response, one must take into account the intrinsic dilatational viscosity, κ, which contributes to the imaginary part of the complex modulus E. Thus, the complete definition of elasticity reads:

$$E(\omega,c) = \left|E(\omega,c)\right|\exp(i\phi(\omega,c)) = \varepsilon(\omega,\Gamma) + i\kappa\omega \qquad (3.5)$$

where the real part $\varepsilon(\omega,\Gamma)$ is the storage modulus depending on surface composition and frequency.

3.3. MEASUREMENT OF THE SURFACE DILATATIONAL MODULUS

The surface dilatational modulus is a measure of the change of the surface tension, $\Delta\gamma$, upon a defined change in the surface area $\Delta A/A$. Its measurement requires a precise knowledge of the dynamic surface tension and area change. Many methods for the investigation of equilibrium properties of fluid surfaces and interfaces are known[9,10]. For instance, we can cite light scattering techniques[11] as well as oscillating drop tensiometry.

In the latter, the shape of a drop is determined by the balance between gravity and surface tension[12]. Oscillating drop tensiometry gives the surface tension while video analysis leads to the area of the oscillation. Miller *et al*[13] investigated the limit of the technique and found an upper frequency limit of 1Hz. Despite the fact that it remains a good technique for the analysis of proteins, its use for classical surfactants is thus rather limited.

Other techniques are based on the principle of harmonic changes of the area. These techniques operate over different frequency ranges and use different excitation principles. The capillary wave technique generates harmonic waves mechanically or electrically and measures the damping factor and the wavelength of the propagated wave. The frequency range covered by this technique is from 30 Hz to 4 KHz. However, the wave parameters have to be determined precisely, which is very difficult to achieve experimentally[14-17].

The oscillating barrier method is another well-established method[18-20]. This is a modified Langmuir through possessing two symmetrically oscillating barriers and a Wilhelmy plate used to measure the dynamic surface tension. In this case, the method works only over a very small frequency range of 0,005 Hz to 0,5 Hz. This method is therefore limited to insoluble monolayers or soluble surfactants at low concentrations.

The most precise measurements are possible by the oscillating bubble technique. It is important that harmonic surface changes match the molecular exchange processes at the surface. If the harmonic oscillation is much slower than the molecular exchange processes, the surface tension adopts an equilibrium value and there is no resistance against the area change. If the harmonic oscillation is too fast, the molecular exchange is suppressed and the behaviour of a Langmuir monolayer is observed. For soluble surfactants, the decisive frequency range, the so-called mid-frequency range, covers 1 to 500 Hz. This range can be covered by the oscillating bubble technique, pictured in figure 3.4. Thus, it is a suitable technique to get the surface dilatational modulus of soluble surfactant solutions.
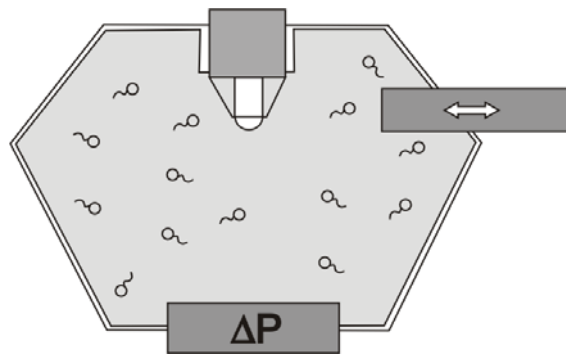
Figure 3.4   Cross-sectional view of the oscillating bubble technique chamber.

The oscillating bubble technique is related to oscillating drop tensiometry but instead of analysing the drop contour, it monitors the Laplace pressure within the chamber:

$$\gamma(t) = \frac{P(t)r(t)}{2} \qquad (3.6)$$

This technique has been first described by Kretzschmar *et al*[21] and Wantke *et al*[22,23]. This method covers a frequency range of 1 Hz to 500 Hz, which makes it a very versatile technique. The principle of the method is presented in Figure 3.4. A small hemispherical bubble is produced at the tip of a capillary. The capillary is dipped in a surfactant solution that fills a closed measuring chamber. A piezoelectric translator generates a sinusoidal oscillation of the bubble. The bubble oscillates with a specific amplitude and frequency. Changes in the bubble radius and surface area, and consequently in the adsorption layer

density, produce sinusoidal changes of the pressure in the chamber. A sensitive pressure transducer records the change.

The oscillating bubble technique possesses a well-defined geometry. The spherical symmetry enables a sound modelling of the underlying processes. Unwanted features such as Marangoni flow are suppressed and bulk effect can be eliminated by proper calibration with known substances. As mentioned above, the frequency range is quite wide and the specific geometry allows one to get reliable information about the intrinsic dilatational surface modulus in the mid-frequency region.

The oscillating bubble technique has been pioneered by Wantke and Fruhner. It has been improved and further developed during this thesis. An automatisation of the system has been performed. Moreover, the design of the chamber has been reengineered. The data obtained with this technique have been related to the Lucassen-van den Tempel-Hansen model (LvdTH model).

3.4. THE LUCASSEN–VAN DEN TEMPEL–HANSEN (LVDTH) MODEL & THE GIBBS ELASTICITY

Early ideas on foam stability assumed that it was determined by adsorbed surfactants, which controlled the mechanical-dynamical properties of the surface layer. The well-established Lucassen-van den Tempel-Hansen (LvdTH) model was one of the first model describing the dynamic surface behaviours[24,25]. Figure 3.5 depicts the model proposed back in the seventies.
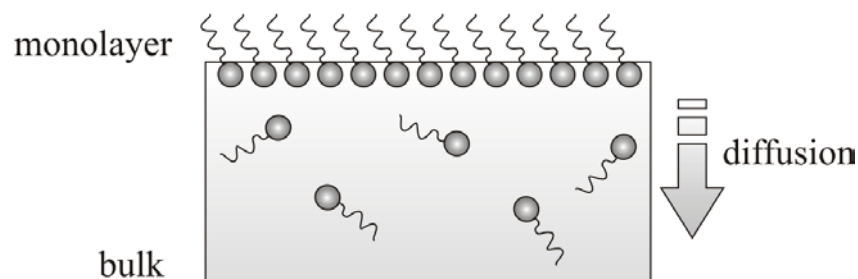
Figure 3.5   The LvdTH model, consisting of a monolayer and a bulk where the surface-active molecules are solubilized.

The model consists in a monolayer where molecules adsorb at the interface, and a bulk, where molecules are solubilized. There is a fast exchange of the molecules between the bulk and the monolayer, and by compressing or extending the surface, the diffusion of the molecules in the bulk is observed. The LvdTH model adopts the following analytical form[18,25]:

$$\varepsilon(f,c) = E(f,c)\exp(i\varphi(f,c)) = \varepsilon_g \frac{1+\zeta+i\zeta}{1+2\zeta+2\zeta^2} \tag{3.7}$$

with $\zeta = \sqrt{D/2\omega}\, dc/d\Gamma$; D being the diffusion coefficient of the surfactants in the bulk and $\omega = 1/\tau$ with τ being the diffusion relaxation time.
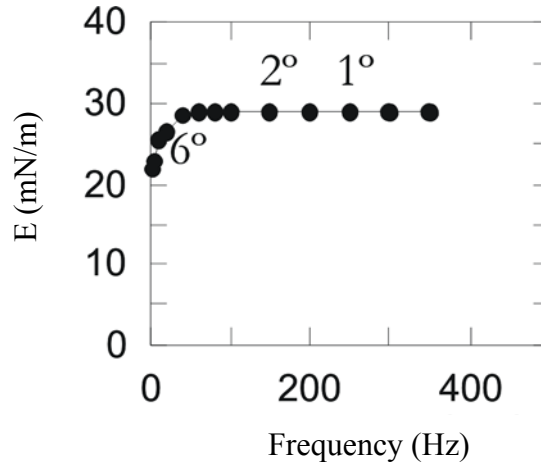
Figure 3.6 Elasticity as a function of the frequency for a 1 mmol CTAB solution. The numbers represent the phase shift observed between the pressure response and the piezo oscillation at the corresponding frequencies.

Several surfactant systems can be described within the frame of the LvdTH model. Figure 3.6 shows an oscillating bubble measurement performed on a 1 mmol hexadecyl-trimethylammonium bromide (CTAB) solution. The curve shows the magnitude of the elastic modulus as a function of the oscillating frequency. We observe that the modulus reaches a limited value (ε_m) at higher frequencies. Furthermore, the phase shift vanishes at higher freqencies. This describes a purely elastic behaviour, as predicted by LvdTH model.

The system shows a much more complex behaviour when measured at higher concentration, near the CMC. An example of such a situation is presented in figure 3.7, where the oscillating bubble measurement on a 6 mmol hexadecyl-trimethylammonium bromide (CTAB) solution is depicted. First, the elasticity modulus does not reach a plateau; instead, it continuously increases with the frequency. Furthermore there is a phase-shift of about 20 degrees between the piezo oscillation and the pressure response. This behaviour is not captured by LvdTH model and requires further modification: it describes a surface viscoelastic system, which is manifested in a phase shift between the harmonic piezo oscillation and the harmonic pressure response.
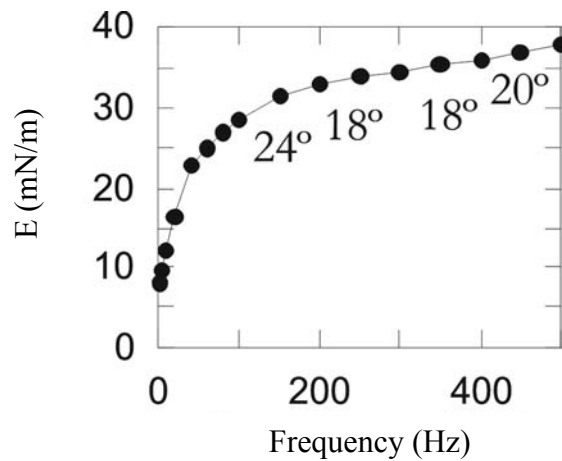
Figure 3.7   Elasticity as a function of the frequency for a 6 mmol CTAB solution. The numbers represent the phase shift observed between the pressure response and the piezo oscillation at the corresponding frequencies.

As a conclusion, the LvdTH model fully describes a purely elastic system, as expressed by Lucassen *et al*[24], but it cannot account for surface viscoelastic behaviours.[1,3,26,27]. Therefore, the LvdTH model has been modified.

3.5.   THE MODIFIED LVDTH MODEL AND THE INTRINSIC SURFACE DILATATIONAL MODULUS

The simplest way to account for the observational facts is to add an imaginary part to the modulus as shown in the equation 3.8, where κ would be the intrinsic surface

dilatational viscosity. The dimension of κ is Ns/m. At higher frequencies, the imaginary part of the modulus contributes to its magnitude.

$$\varepsilon(f,c)=E(f,c)\exp(i(f,c))=\varepsilon_g\frac{1+\zeta'+i\zeta'}{1+2\zeta'+2(\zeta')^2}+i\kappa\omega \tag{3.8}$$

Here an intrinsic dissipative term $i\kappa\omega$ is added and the real function ζ of equation 3.7 must be replaced by the complex expression $\zeta'=h(f)\zeta$, with

$$h(f)=k/(k+(1+i)(\omega D/2)^{1/2}) \tag{3.9}$$

characterizing the non-equilibrium state within the surface layer. It depends on the rate constant k [1,3]. For great k ($k^2 \gg \omega D$), the molecular exchange between monolayer and sublayer is so fast that the equilibrium state within the surface layer is instantaneously established and h becomes 1.

Simply speaking, the modulus consists of two contributions: the classical LvdTH model with its plateau at higher frequency and a linear contribution coming from the imaginary part to the modulus. The combined features assemble the characteristic of the measurement. The equation is separated in two terms, the first being the compositional term and the second arises from the intrinsic dilatational surface viscosity. These two terms are schematised in figure 3.8.
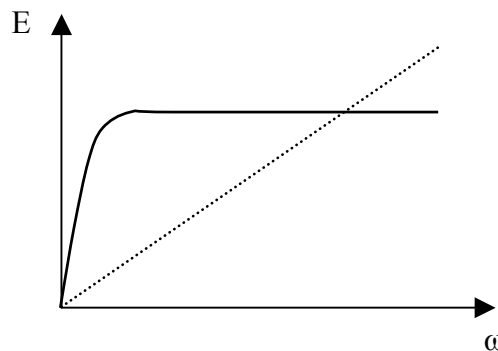
Figure 3.8   Intrinsic dilatational surface elasticity (─) and intrinsic dilatational surface viscosity (·····)

The Gibbs elasticity can also be calculated from the surface tension isotherm, according to the following development:

$$\varepsilon_0(c) = -\Gamma \frac{dc}{d\Gamma} \frac{d\gamma}{dc} = \left. -c\left(\frac{d\gamma}{dc}\right)^2 \middle/ \left(\frac{d\gamma}{dc} + c\frac{d^2\gamma}{dc^2}\right) \right. \tag{3.10}$$

The oscillating bubble technique measures precisely the high frequency limit ε_m of the modulus. A puzzle is a striking mismatch between the high frequency limit and the Gibbs elasticity as retrieved from the equilibrium surface tension isotherm. The mathematical procedure requires the formation of the second derivative with all its accompanying numerical uncertainties. Despite this big error in ε_0 (Gibbs elasticity) there is a fundamental mismatch as shown as in figure 3.9.
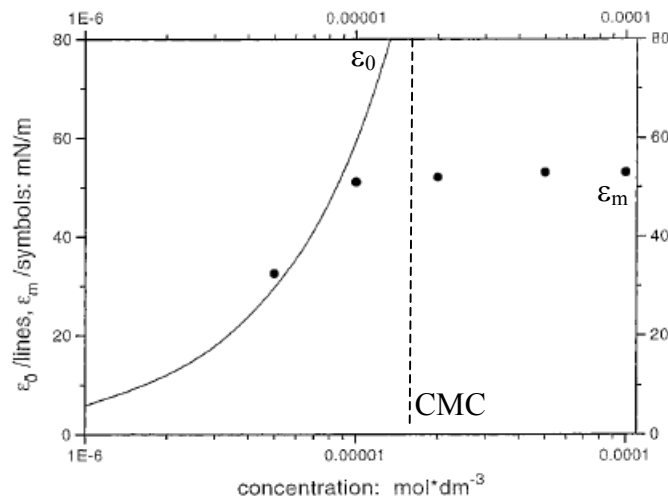
Figure 3.9   Comparison between ε_0 (calculated Gibbs elasticity) (–) and ε_m (high frequency limit fom experimental Gibbs elasticity) (●) for tridecyl-dimethyl-phosphine oxide solutions[3].

On figure 3.9, ε_m is presented as a function of the concentration. Slightly after the CMC, the value reaches a plateau and remains constant. However, in the case of ε_0 the behaviour is clearly different as the value increases suddenly, shortly before the CMC. This puzzle can be resolved by modifying the adsorption model.

In the examples presented in the precedent section as well as in figure 3.9, the frequency dependence of the E modulus of the surfactant illustrates clear evidence for the presence of an intrinsic surface dilatational viscosity. It has been proven that including a molecular exchange between the monolayer and an added sublayer to the existing model can bridge these contradictions. The modified LvdTH model as it would then become, is presented in Figure 3.10.
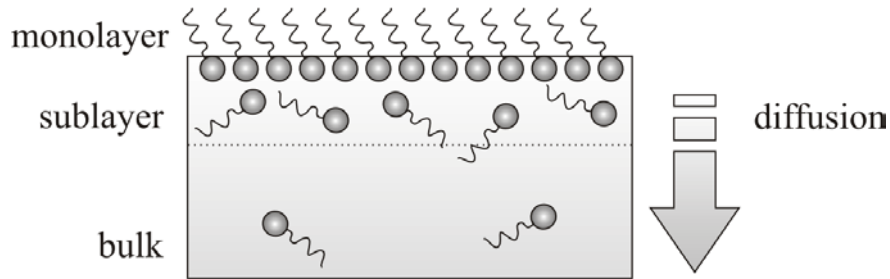
Figure 3.10   The modified LvdTH model, where a sublayer has been added to the existing model.

In this case, by compressing the surface, one pushes the molecules of the monolayer into the sublayer where they accumulate to form an enrichment layer. When expanding the layer again, molecules return to the interface.

In a more practical way, we can rewrite equation 3.8 starting from the Gibbs elasticity used in the LvdTH model as the first step in the elaboration of the complex term representing the intrinsic dilatational surface modulus. The equation would then become:

$$E(\omega, c) = A \frac{\delta \gamma}{\delta \Gamma} \cdot \frac{d\Gamma}{dA} + \kappa \cdot \frac{\delta(\Delta A)/\delta t}{\Delta A} \qquad (3.11)$$

where E is the elasticity modulus as a function of the concentration (c) and the frequency (ω), γ is the dynamic surface tension, ΔΓ, the change in surfactant concentration at the surface, κ, the surface dilatational viscosity, and ΔA, the change in surface area.

Oscillating bubble measurements as well as comparison between calculated and experimentally obtained Gibbs elasticities demonstrated that the original LvdTH model

has to be modified to overcome its imperfections. The literature shows that a sublayer has been added to overcome the problem. Mathematically, the discrepancies would be bridged. Some indirect experimental proofs have also been published in the past. However, real direct experimental proofs are lacking. In this part of the thesis, an experiment combining non-linear optical techniques with the oscillating bubble technique has been developed and used in order to get a clearer picture.

3.6   COMBINATION OF SURFACE SHG AND OB

Oscillating bubble technique allows one to get the intrinsic surface dilatational viscoelastic modulus described by equation 3.11. SSHG leads to the concentration of molecules at the surface. Combining the two techniques allows for instantaneous measurement of the concentration of surfactants in the monolayer (Γ_m) in the mid-frequency range. This represents a major unknown parameter in the theoretical models describing surface rheology. The discrimination of the two signals coming from the two techniques is pictured in Figure 3.11.

$$\Delta\gamma = \frac{\partial\gamma}{\partial\Gamma}\Delta\Gamma + \kappa\frac{\partial(\Delta A)/\partial t}{A}$$

Obtained by surface pressure measurements according to the oscillating bubble method.

SHG gives the concentration of the molecules at the surface
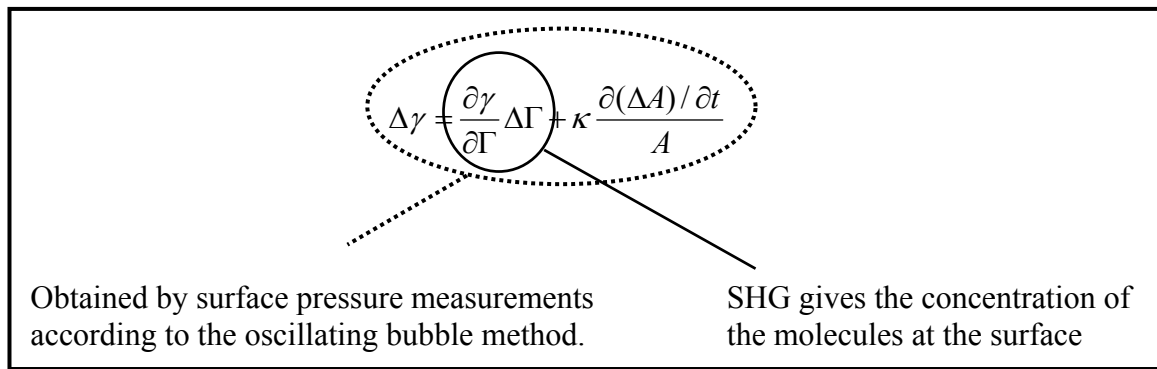
Figure 3.11   Mathematical representation of the terms found with oscillating bubble and SHG techniques.

With the setup used in this thesis, it is possible to cover the 10-60 Hz range. For frequencies above 60 Hz, the shape of the bubble deviates a little from the spherical geometry. This is due to oscillations; because of this, the reflected light is spread differently, and the comparison of the results is less accurate.

3.7 EXPERIMENTAL SECTION: SURFACE SHG-OB ON AN ELASTIC SYSTEM

3.7.1 MATERIALS

Various concentrations of aqueous solutions of the hemicyanine dye HC_8 were studied as a model-system of an elastic surfactant. The molecule is depicted in Figure 3.12, as well as the fluortenside F381. The results obtained with the F381 have been published previously[4,28], and will be used here for comparison purpose. All solutions were prepared by dissolving the solid in MilliQ water.
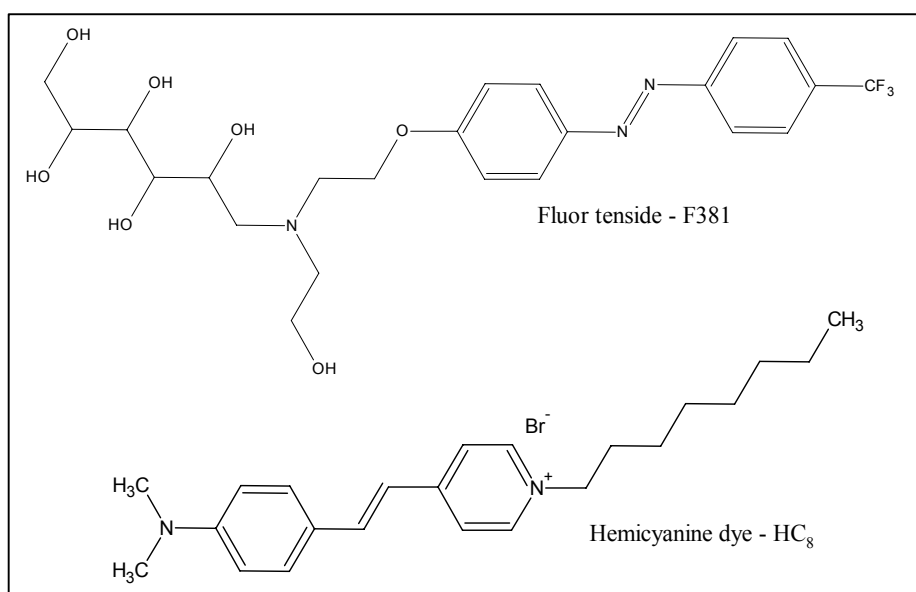
Figure 3.12   Molecular structure of F381 and HC_8. Both substances possess a high hyperpolarizability, due to the π-system, favoring the SHG signal.

3.7.2 OSCILLATING BUBBLE MEASUREMENTS

The oscillating bubble method used in this work generates a change in the adsorption state at the fluid surface of a bubble in a well-defined manner. An open capillary with a diameter of approximately 0,4 mm is placed within a closed chamber. At the tip of the capillary a small hemispherical bubble is produced. A piezoelectric translator immersed in the chamber generates a sinusoidal oscillation of the pressure in the chamber, causing the bubble to oscillate. The amplitude of the pressure response as well as the phase shift between the piezo-oscillation and the pressure signal are evaluated via a phase-sensitive

lock-in detection scheme. The apparatus used allows a frequency range of 1-500 Hz. Bulk effects are eliminated by calibration measurements on decanoic acid solutions and water.

3.7.3 SHG-OSCILLATING BUBBLE MEASUREMENTS

The setup, which has been developed in our laboratory, has been modified from its original version[4,28] in order to avoid the absorption caused by the aqueous solution of hemicyanine dye at 266nm, as shown in Figure 3.13. The setup is described in details in the following lines.
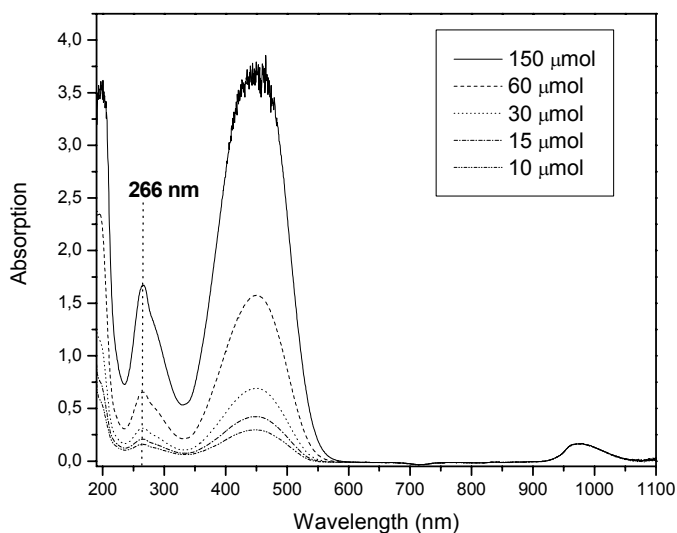
Figure 3.13 UV-VIS spectra (cuvette = 1cm) of different concentrations of HC_8.

First, the chamber is filled with an aqueous solution of surfactants. At the tip of a glass capillary in the middle of the chamber, a small hemispherical bubble is formed. The capillary was silanized and broken before usage, leaving the capillary walls hydrophobic and the fracture area hydrophilic. This three-phase contact is essential for the stability of the bubble.

A piezoelectric translator (LVPZT, 830.40, Physik Instrument) is connected to the chamber, generating a sinusoidal deformation of the bubble volume, and consequently of the surface area and the bubble radius. The voltage over the piezoelectric translator is generated by a computer (A-WIN) and amplified (LVPZT-amplifier, model E-501.00,

Physik Instrument) before reaching the translator. The computer also triggers the laser, described in section 2.6.4, and the trigger signal can be freely chosen during the sinusoidal voltage cycle.

The fundamental light is coming into the chamber from the lower left part of the chamber and is focused by a lens (*f* =16 mm, Linos Photonics) onto the bubble. The lens is attached to a movable screw, making it possible to adjust the distance between the lens and the bubble. Light is incident with an angle of 68°, in the total reflection mode at the bottom of the bubble, which has a diameter of approximately 2mm. The frequency-doubled light generated at the bottom of the bubble is passing first through a UV-transparent cuvette, which was installed about 2 mm from the oscillating bubble on the exit side of the chamber in order to decrease the UV absorption coming from the solution. The light is then collected by a quarz-lens (*f* = 20 mm, Linos Photonics) attached to an adjustable screw at the rear end of the chamber, and exiting in the lower right part of the chamber. A scheme of the chamber is presented in figure 3.14.
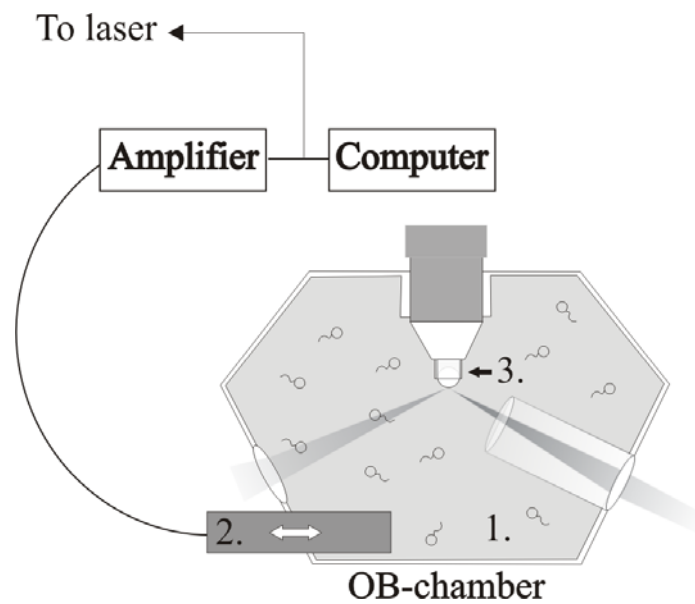
Figure 3.14   Scheme of the oscillating bubble chamber used for the SHG on an oscillating bubble experiment. 1. Surfactant solution, 2. Piezoelectric translator, 3. Capillary. The distance between the bubble and the UV-cuvette is 2 mm.

For the elastic system, the SHG measurements were carried out with the frequency-doubled light at 532 nm of an active/passive mode-locked Nd:YAG (Neodymium:Yttrium-Aluminum Garnet) laser (B.M. Industries YAG 502 DPS 7910DP). The laser pulses were 35 ps wide, the repetition rate 10 Hz and the intensity of the incoming pulse between 0,1-0,15 mJ.

The experiment is fully controlled by a computer which synchronizes the laser pulses with the bubble oscillation accounting also for the temporal jitter between subsequent pulses, a common feature of flash lamp pumped active-passive mode-locked Nd:YAG laser systems. The setup guarantees that the laser pulse hits the bubble at a user-defined phase within the sinusoidal bubble oscillation. In this way 100–500 pulses can be recorded under exactly identical conditions. This is a requirement to obtain a reliable signal-to-noise ratio.

A common problem under Windows environment is an extremely poor real time capability. For this reason, we used a Sharc ADSP 21062 processor for the all time critical processes and reduced the function of the Windows environment for the data visualization.

The laser light was plane-polarized before the surfactant solution, using a Glan–Thomson prism (extinction ratio 10-6, type *K*, Steeg & Reuter). The plane of polarization was rotated 39° from vertical polarization, where SHG is independent of the distribution of the molecular orientation.[29]

In the case of the HC_8 solution, the spectral purity of the incoming light was assured by use of a narrow-band interference filter (532BP, LOT-Oriel). The frequency-doubled light generated at the interface was separated from the fundamental light by use of two visible cutoff filters (UG5, UG11, Schott) and two narrow-band interference filters (266 BP, LOT-Oriel). The absorption spectra of the filters used in this configuration are presented in Figure 3.15.
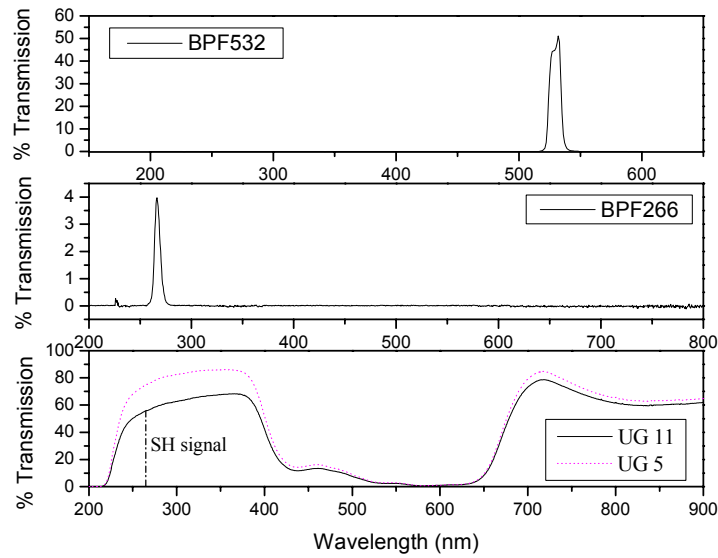
Figure 3.15   Transmission spectra of the filters used in the OB-SHG setup for the HC_8 solution studies.

The SH light was detected by a photomultiplier tube (R1398, Hamamatsu) with a quantum efficiency of 15%, and a cathode radiant sensitivity of 35 mAW^{-1} at 266 nm. The supply voltage over the photomultiplier tube was 1850 V (V5D, Seefelder Messtechnik). The detected signal was processed by an oscilloscope (54720D, Hewlett-Packard) and integrated by a computer program. The amplitude of the sinusoidal voltage over the piezoelectric translator was 30 V, giving a relative amplitude ($\Delta A/A$) of the area of the bubble during oscillation of $0,18 \pm 0,04$, as studied by optical means. A scheme and pictures of the setup are presented in Figure 3.16 and Figure 3.17.

The shape and size of the oscillating bubble in the SHG setup was studied by optical means through the small window in front of the chamber. The image of the bubble was detected by a charge coupled device camera (EHDkam-Pro02, EHD Imaging GmbH) and transferred to a screen. A sharp image of the bubble during oscillation was obtained by using the laser pulses as only light source. According to these observations, the shape of the bubble was hemispherical up to 60 Hz.
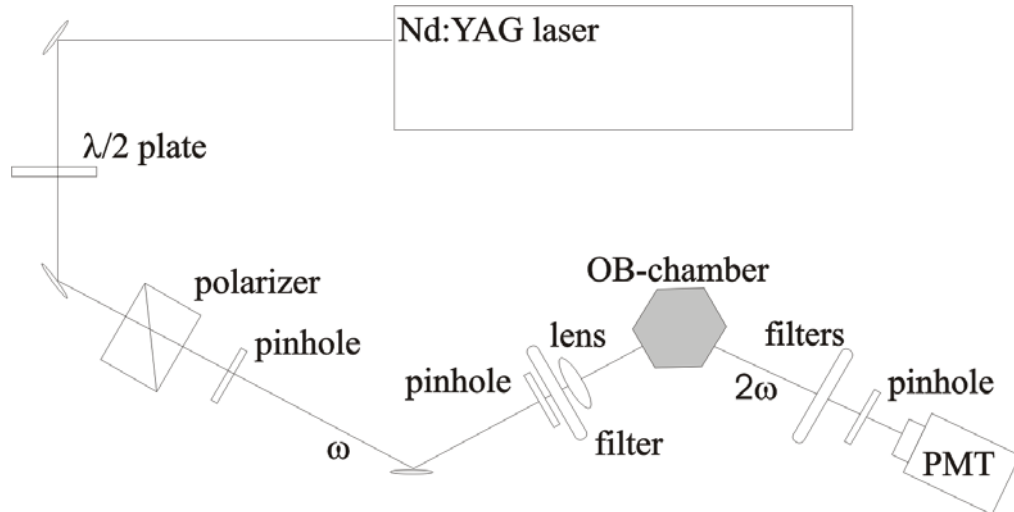
Figure 3.16 Scheme of the setup used for the SHG on an oscillating bubble experiment for the HC_8.
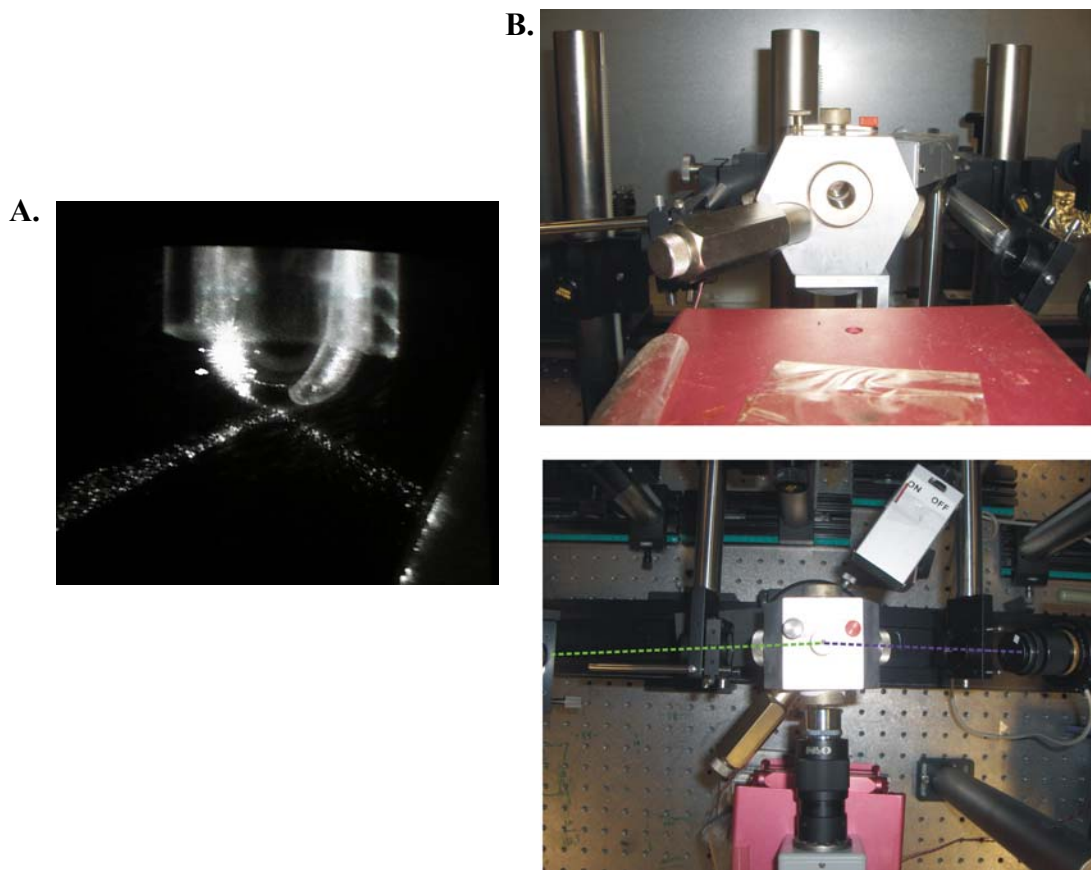
Figure 3.17 **A.** Picture of the oscillating bubble (oscillation frequency of 40Hz), with the laser beam as only light source and **B**. Picture of the setup in general (front view and top view).

We define the phase angle Ψ of the bubble during oscillation as 90° when the bubble obtains its minimum volume and 270° when it obtains its maximum volume, respectively. Consequently, at the phase angles 0° and 180°, the bubble is at its equilibrium volume. This is pictured in Figure 3.18.
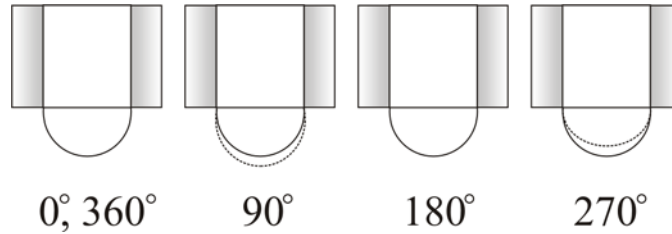
Figure 3.18   Definition of the phase angle Ψ for the different phase angles of the bubble oscillation. The dotted line is the volume of the bubble at equilibrium whereas the full line represents the volume of the bubble as the light hits it.

In measuring SHG at different phase angles, two difficulties must be overcome: first, the detected SHG signal is proportional to the square of the intensity of the fundamental light. This means that as the bubble oscillates, a small spatial deviation from focus at various phase angles may cause a change in the detected SHG signal. Moreover, the curved surface in combination with a spatially limited area of the lens collecting the outcoming light leads to a loss of some of the SHG intensity. Therefore, the shape of the bubble at minimum volume ($\Psi=90°$), having a less curved surface, may lead to a higher SHG signal. These two problems are solved by adjusting the equilibrium volume of the bubble in the following way: in the case of measuring at a phase angle of 90°, the equilibrium volume of the bubble is made slightly larger than a half-sphere, so that the bubble is exactly a half-sphere as it was hit by light. Analogically, in the case of measuring at a phase angle of 270°, the equilibrium volume of the bubble is made slightly smaller than a half-sphere, again so that the bubble is a half-sphere as it is hit by light. In the case of the phase angles 0° and 180° the bubble is a half-sphere both in equilibrium and as it is hit by light. Consequently, light hits the bubble at exactly the same position and same size at all Ψ.

3.7.4 RESULTS & DISCUSSION

Oscillating Bubble measurements

The surface dilatational modulus $\varepsilon(f,c)$ was measured for two different concentrations of aqueous solution of HC_8. A series of oscillating bubble measurements has been performed in the frequency range of 0-500Hz. Each measurement has been repeated at least 5 times. The results are presented in figure 3.19.
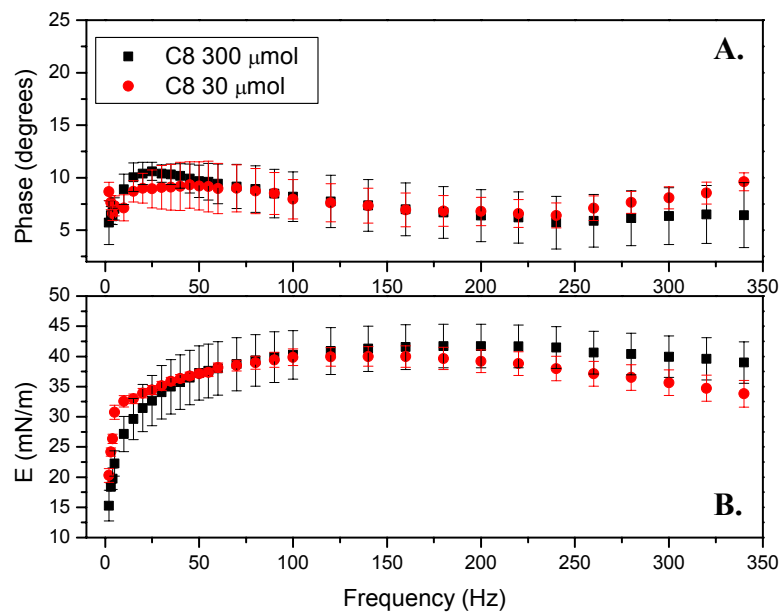
Figure 3.19   **A.** Phase shift φ between the piezo oscillation and the sinusoidal pressure response as a frequency ω of the bubble oscillation and **B**. Magnitude of the complex modulus of elasticity for 30 μmol (●) and 300 μmol (■) HC_8 solutions.

In figure 3.19 B, the magnitude of the complex modulus of elasticity is presented as a function of the frequency. We see that it increases until approximately 100 Hz and then reaches a plateau. The phase shift, φ, presented in figure 3.19 A, shows a normal trend for elastic behaviour. One should note that for the lower concentrations, the values are too small compared to what is expected: this is due to instabilities of the bubble. Nevertheless, we can conclude that the HC_8 sample is elastic at 30 μmol and 300 μmol.

Tensiometry and Static SSHG measurements

To verify the SHG analysis method, we compared the SSHG results yielding Γ_m with the results from tensiometry, giving the $\gamma(c)$ adsorption isotherm. The surfactant concentration of the monolayer can be retrieved from the $\gamma(c)$ adsorption isotherm through the Gibbs adsorption equation (equation 3.5).

SSHG measurements were done in equilibrium on a flat interface air-liquid for various concentrations of HC_8. From these measurements, we can retrieve the $\Gamma_m(c)$ adsorption isotherm by using equations 1,6, 1,9 and 1,10. This is shown in figure 3.20. The surface tension $\gamma_m(c)$ was obtained from equation 2.2 by integrating $\Gamma_m(c)$ with respect to c and by least-square fitting with a proportionality constant to $\gamma(c)$ measured by tensiometry.
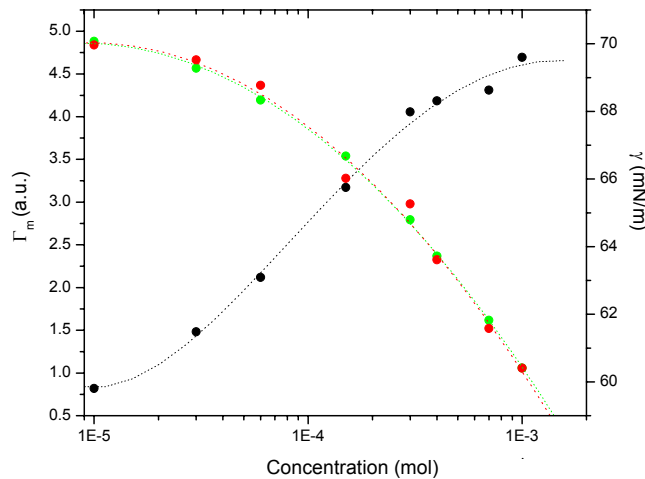
Figure 3.20 Equilibrium surface tension measured by tensiometry ($\gamma(c)$) (●) and calculated from the SHG signal ($\gamma_m(c)$) (●) and adsorption isotherm obtained by SHG ($\Gamma_m(c)$) (●) for HC_8 solution.

In figure 3.20, we present the results as a function of bulk concentration. When comparing the values of $\gamma(c)$ and $\gamma_m(c)$, we must remember that SSHG detects only the monolayer concentration $\Gamma_m(c)$[30,31] We also assumed that the measured surface tension yields the monolayer concentration according to equation 3.5[28]. We observe on figure

3.20 that there is a close overlap between $\gamma(c)$ and $\gamma_m(c)$; therefore the assumptions of equilibrium are valid and we can conclude that the use of the oscillating bubble combined with the SSHG is further motivated.

SHG on an Oscillating Bubble

The bubble that is oscillating in the SHG-OB setup has a hemispherical shape and possesses a relative amplitude ($\Delta A/A$) of $0,18 \pm 0,04$. This was determined by optical means[4]. The value of $\Delta A/A$ was chosen to be much larger than the error of the measurements.

The variation of the square root of the SH signal is proportional to $\Delta A/A$ and leads to an approximately linear response [4,28,32]. If the surfactant density of the monolayer fulfils the condition

$$\frac{\Delta \Gamma_m}{\Gamma_m} = -\frac{\Delta A}{A} \tag{3.10}$$

we can assume that the monolayer represents the effective surface layer.

According to the results published on the F381[4,28], the tensiometric studies show that kinetic exchange processes do not limit the molecular flow at the surface. This means that an equilibrium state prevails within the surface layer. Moreover, the diffusive molecular exchange between the bulk and the surface is comparatively small, already at 10Hz. It is thus expected that the number of molecules at the surface remains constant for the oscillation frequencies obtainable from the actual setup (10-60Hz).

An example of the result we obtained for HC_8 solutions is presented in figure 3.21. One can observe the measurement of the SH signal onto an oscillating bubble for four phase angles Ψ. It is important first to calibrate with water, for then we can calculate the normalized surfactant density of the monolayer as a function of the phase angle Ψ, using equations 1.9 and 1.10. We can then compare this value with $\Delta A/A$. In the following sections, this has been done for different experimental cases.
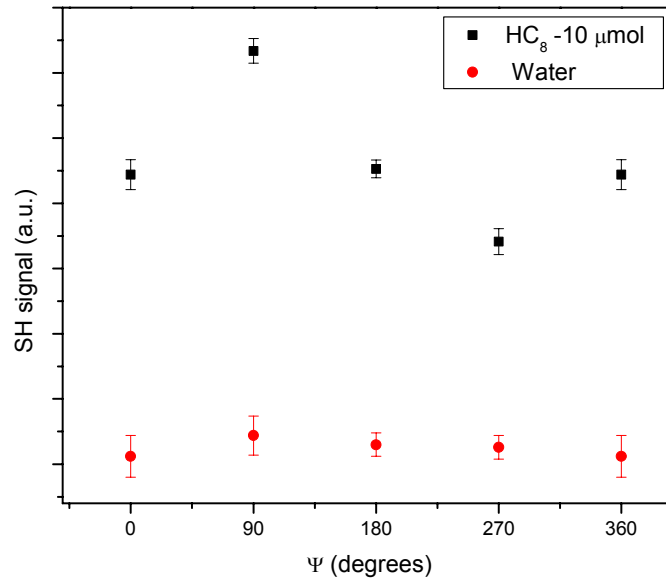
Figure 3.21   SH intensity reflected by the oscillating bubble as a function of the phase angle ψ. c = 10μmol, *f* = 40 Hz

Frequency dependence of the surfactant density of the monolayer during oscillation

Figure 3.22 presents a series of SHG-OB measurements at different phase angles Ψ for different frequencies of oscillation in the case of a 10 μmol HC_8 solution. One clearly observes maxima and minima at 90 and 270 degrees, respectively.

The normalized surfactant density of the monolayer, $\Delta\Gamma_m/\Gamma_m$, was calculated for every frequency and the results are presented in table 3.1. The variation between the four frequencies is not significant, and is mainly due to experimental inaccuracy.

We can conclude that the value of $\Delta\Gamma_m/\Gamma_m$ is independent of the oscillation frequency between 10 and 60 Hz. The same experiment was done for different concentrations and the same results were obtained in all cases. Moreover, it is completely in agreement with the first results published on the F381 surfactant[4,28]. The results obtained here show good agreement with the tensiometric studies by the oscillating bubble technique as well as with the assumption that the sublayer and the monolayer are in equilibrium during the whole deformation cycle in the studied frequency range.
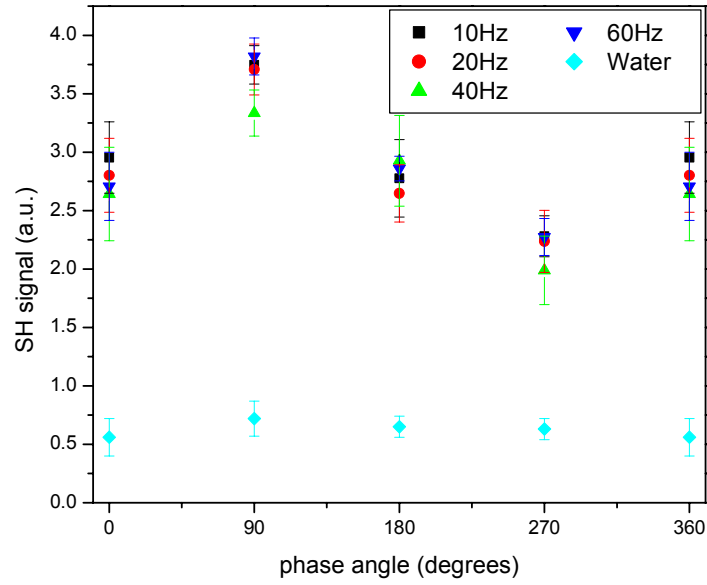
Figure 3.22   SH intensity reflected by the oscillating bubble as a function of phase angle ψ. c = 10µmol, f = (■) 10 Hz, (●) 20 Hz, (▲) 40 Hz, (▼) 60Hz, (◆) Water.

Frequency	$\Delta\Gamma_m/\Gamma_m$
10 Hz	0,16 ± 0,01
20 Hz	0,18 ± 0,02
40 Hz	0,15 ± 0,01
60 Hz	0.16 ± 0,01

Table 3.1 $\Delta\Gamma_m/\Gamma_m$ calculated for different oscillation frequencies for a 10 µmol HC_8 solution.

Bulk concentration dependence of surfactant density of the monolayer

Figure 3.23 shows a series of SHG-OB measurements at different phase angles Ψ for different bulk concentration at a fixed oscillating frequency (f = 40Hz).

The signal of the 1 µmol solution is lower than for 10 and 30 µmol since a higher concentration increases the surface coverage and thus the SH signal generated at the tip of the bubble. The signal is, however, lower for 45 and 60 µmol than for smaller concentration and this is probably due to the absorption of the signal by the bulk solution, since it also increases with the bulk concentration. As the absorption influences the signal for higher concentration, we decided to compare only the normalized surfactant density of the monolayer amplitude, $\Delta\Gamma_m/\Gamma_m$, which is not affected by the bulk absorption.
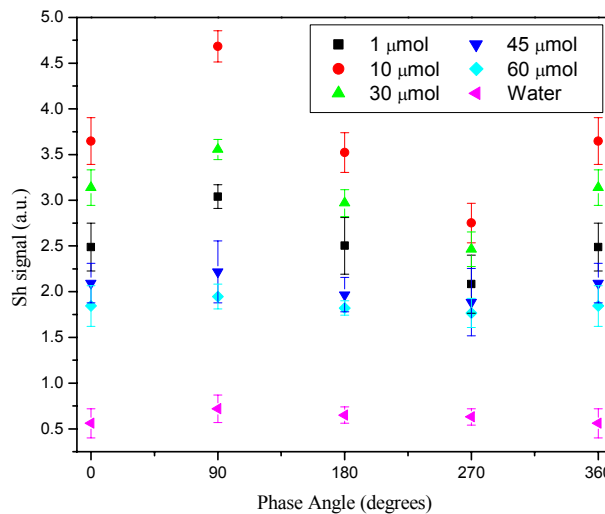
Figure 3.23 SH intensity reflected by the oscillating bubble as a function of phase angle ψ. f = 40Hz, c = (■) 1µmol, (●) 10µmol, (▲) 30µmol, (▼) 45µmol, (◆) 60µmol, (◄) Water.

The normalized surfactant density of the monolayer amplitude as a function of the bulk concentration has been calculated from the data presented in figure 3.23. An average of 10 measurements has been taken for each concentration. The result is presented in figure 3.24.
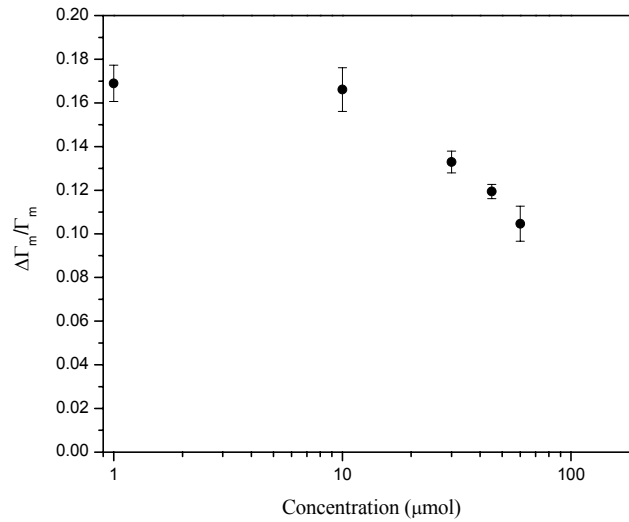
Figure 3.24   Normalized surfactant density amplitude at the tip of the oscillating bubble, as measured by SHG.

On the figure 3.24, one can observe that for 1 and 10 μmol, the value of $\Delta\Gamma_m/\Gamma_m$ is $0,17 \pm 0,02$. Consequently, the equation 3.8 is fulfilled within experimental accuracy for these two concentrations.

If we consider that the phase angle of the measured modulus is always negative, and that the elasticity modulus E reaches a plateau in the frequency range studied, we can conclude that for the lowest concentrations, the dynamics of the system is described by the LvdTH model. The exchange of the surfactants between the sublayer and the monolayer can be neglected even though the two phases are instantaneously in equilibrium due to the fast molecular exchange.

For higher concentrations, the ratio $\Delta\Gamma_m/\Gamma_m$ becomes smaller, to reach $0,08 \pm 0,02$ for 60 μmol. If we compare this trend with the F381 surfactant[4,28], we arrive at the same conclusion. It was, however, impossible to measure higher concentration of the HC_8 due to the high absorption of the signal by the bulk solution.

Thus, the observed decrease of the ratio $\Delta\Gamma_m/\Gamma_m$ suggests an increase in the flow of molecules from the monolayer towards the sublayer when compressing the surface, and a

flow back to the sublayer when expanding it. A scheme of the model is presented in figure 3.25. This means that the molecules remain located in a small sublayer and the change of the concentration in this sublayer has an influence on the surface tension. This behaviour supports the hypothesis of the modified LvdTH model.

Since the results obtained for the HC_8 agree in all cases with the one obtained for the F381 surfactant, we may conclude that the phenomena observed here are not specific to one surfactant, but can be generalized.

We would like now to compare the behaviour of the elastic surfactant observed in these studies with what is observed in the case of a viscoelastic surfactant. This is the topic of the next section.
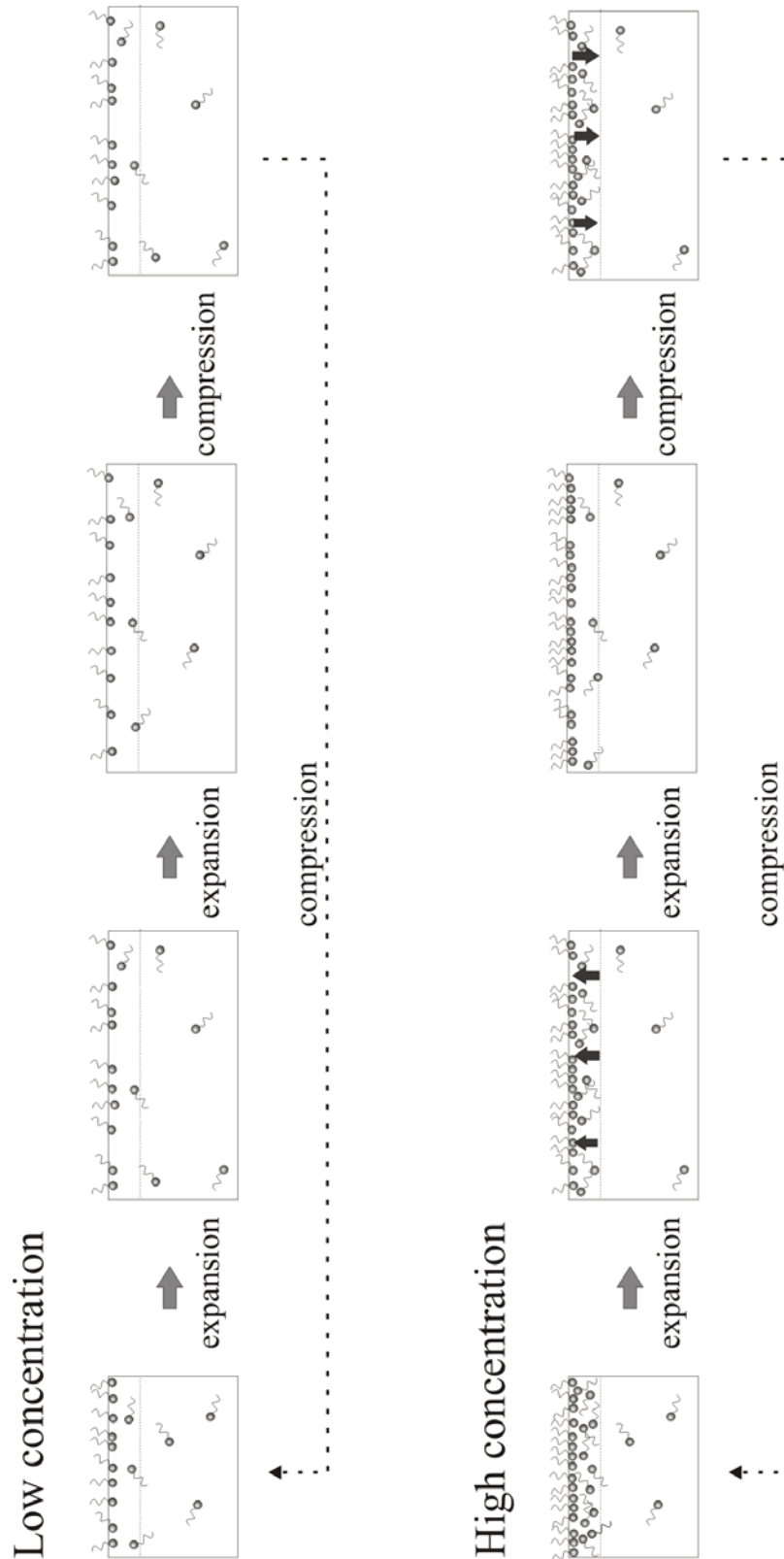
Figure 3.25   Model of the modified LvdTH model in the case of lower and higher

concentrations, for compression and expansion of the surface.Under

dynamic conditions, the sublayer is enriched in amphiphiles.

3.8 EXPERIMENTAL SECTION: SURFACE SHG-OB ON A VISCOELASTIC SYSTEM

3.8.1 MATERIALS

Various concentrations of aqueous solutions of the cationic surfactant dodecyl-dimethylaminopyridinium bromide, PyBr, were studied as a model-system of a viscoelastic surfactant. The molecule is depicted in Figure 3.26. Frau C. Stolle synthesized the compound and all the solutions were prepared by dissolving the solid in MilliQ water.
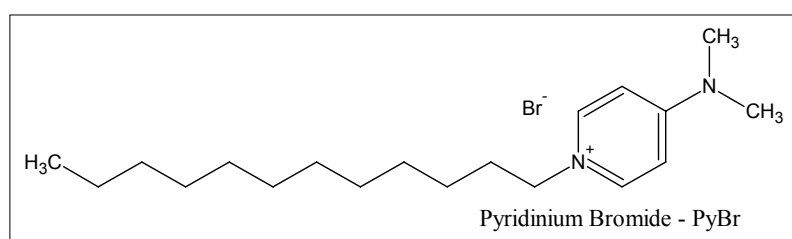
Figure 3.26   Molecular structure of the viscoelastic surfactant PyBr.

As one can observe, the π-system of this molecule is much smaller than the one from HC_8, therefore its hyperpolarizability is smaller and as a consequence, leads to a much weaker signal. The outcome is presented in Figure 3.27. This effect increases greatly the difficulties of getting a signal from the oscillating bubble tip.
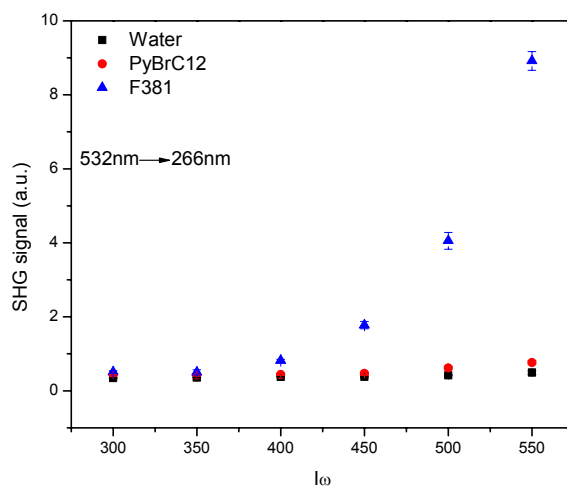
Figure 3.27   SH signal coming from Water, F381 and PyBr in a reflection configuration (532 nm) for different incoming intensities

3.8.2 OSCILLATING BUBBLE MEASUREMENTS

The oscillating bubble measurements performed onto the PyBr solutions have been done with the same system and the way as for the HC_8.

3.8.3 SHG-OSCILLATING BUBBLE MEASUREMENTS

Due to the weaker hyperpolarizability of PyBr compared to HC_8 or F381, as well as the absorption of the signal by the surfactant solutions at 266 nm, as it is presented in Figure 3.28, we could not use the configuration utilized with the HC_8 solutions for the viscoelastic compound. Modifications had to be done.
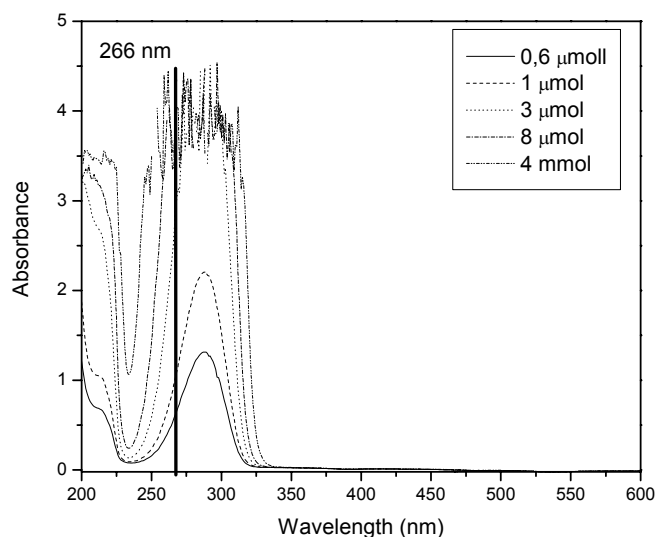
Figure 3.28   UV-VIS spectra (cuvette = 1cm) for different concentrations of PyBr.

Many different configurations have been actually built before we could get a reliable signal. We were finally successful using a 650 nm light instead of 532nm. To do so, frequency-tripled light from the Nd:YAG laser (355 nm, 15 mJ) was directed into an optical parametric generator (OPG). The signal beam at 650 nm from the OPG was used as incident light in the oscillating bubble SHG setup, having an intensity of approximately 0,1-0,15 mJ. The SH generated 325 nm light was detected with a photomultiplier tube (R1398, Hamamatsu) having a quantum efficiency of 20%, and a cathode radiant sensitivity of 55 mAW^{-1} for this wavelength. This setup is presented in figure 3.29.
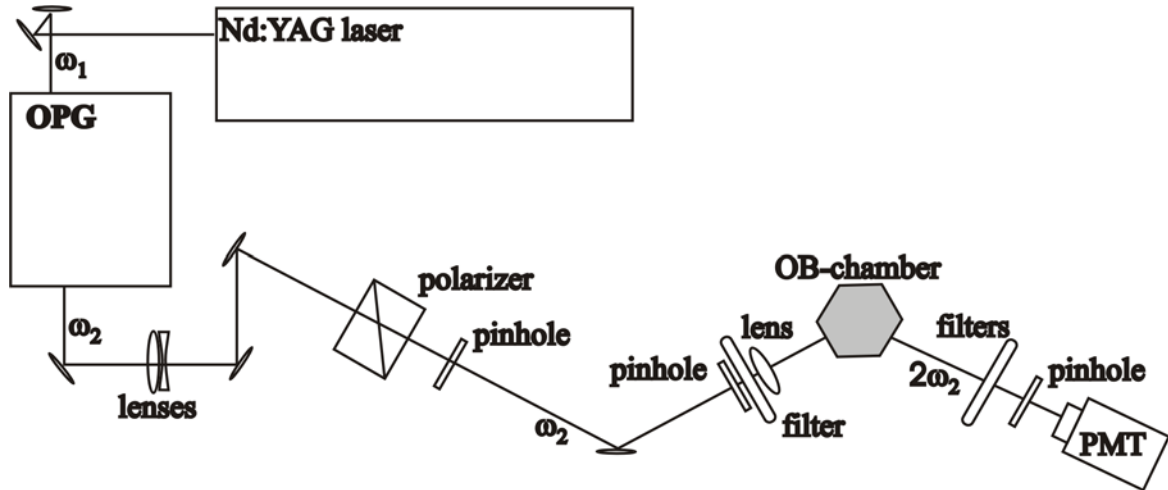
Figure 3.29   Scheme of the SHG-OB setup used for the PyBr solution.

In this setup, a combination of lenses (f = 30 mm and f = -100 mm) has been put at the exit of the OPG in order to get the beam parallel. The polarizer is also set at the magic angle[29] for intensity measurements. For this configuration, the spectral purity of the incoming light was assured by use of a colored filter (RG630, Shott). The frequency-doubled light generated at the interface was separated from the fundamental light by use of two visible cutoff filters (UG5, UG11, Schott) and a narrow-band interference filter (320 BP, LOT-Oriel). Figure 3.30 shows the UV-VIS spectra of the filters.
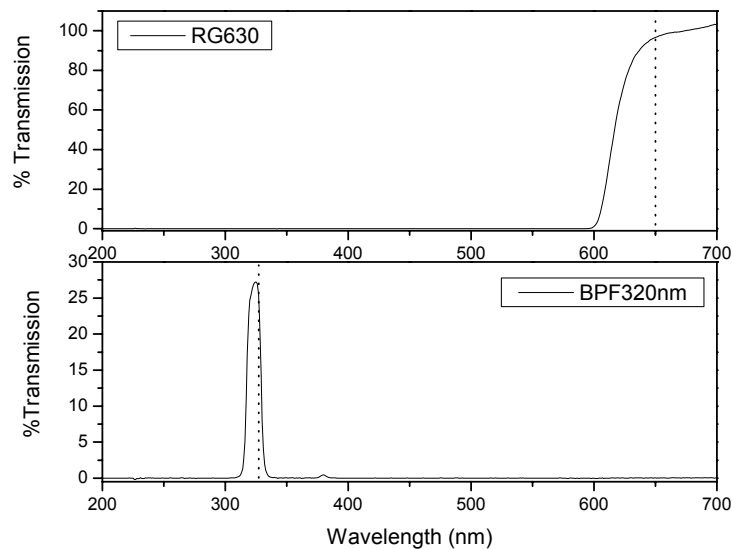
Figure 3.30   Transmission spectra of the filters used in the OB-SHG setup for the PyBr solution studies.

3.8.4   RESULTS AND DISCUSSION

Oscillating Bubble measurements

The surface dilatational modulus $\varepsilon(f,c)$ was measured for different concentrations of aqueous solution of PyBr. A series of oscillating bubble measurements has been performed in the frequency range of 0-500Hz. Each measurement has been repeated at least 5 times. The results are presented in figure 3.31.
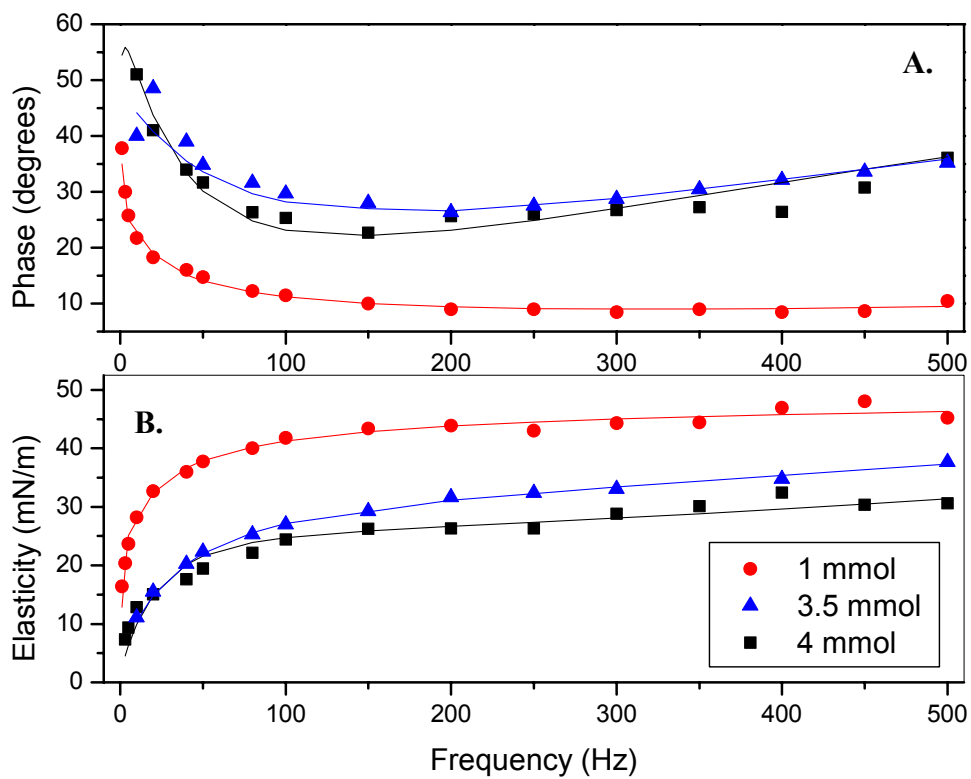
Figure 3.31   **A.** Phase shift φ between the piezo oscillation and the sinusoidal pressure response as a frequency ω of the bubble oscillation and **B**. Magnitude of the complex modulus of elasticity for 1 mmol (●), 3,5 mmol (▲) and 4 mmol (■) PyBr solutions

In figure 3.31B, the magnitude of the complex modulus of elasticity is presented as a function of the frequency. For the smallest concentration, 1mmol, we see that the

elasticity modulus increases until approximately 100 Hz and then reaches a plateau. This is a typical curve for elastic behaviour. However, if we look at the higher concentrations, we observe that after 100Hz, the value of the elasticity modulus continues to increase. This is the normal case for a viscoelastic system. The phase shift, φ, presented in figure 3.31A increases with increasing frequency for the highest concentration; this behaviour is also typical for viscoelastic systems. We can then conclude that for concentration equal to or higher than 3,5mmol, the PyBr surfactant is viscoelastic.

Tensiometry and static SSHG measurements

We compared here as well the SSHG results yielding Γ_m with the results from tensiometry, giving the $\gamma(c)$ adsorption isotherm. Again, the surfactant concentration of the monolayer was retrieved from the $\gamma(c)$ adsorption isotherm through the Gibbs adsorption equation (equation 3.5).
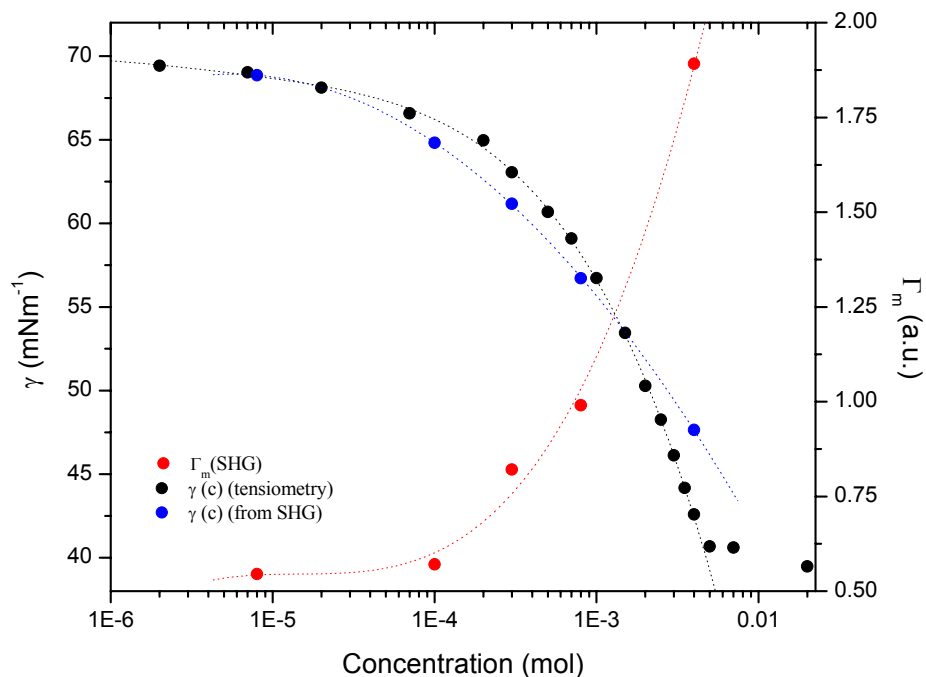
Figure 3.32 Equilibrium surface tension measured by tensiometry (γ (c)) (●) and calculated from the SHG signal (γ_m (c)) (●) and adsorption isotherm obtained by SHG (Γ_m(c)) (●) for PyBr solutions.

SSHG measurements were done in equilibrium on a flat interface air-liquid for various concentrations of PyBr. Following the same argumentation as in the section 3.7.4, we retrieved the $\Gamma_m(c)$; the results are presented in figure 3.32.

The results are shown as a function of bulk concentration. When comparing the values of $\gamma(c)$ and $\gamma_m(c)$, we must consider the same factors as in the section 3.7.4: SSHG detects only the monolayer concentration $\Gamma_m(c)$[30,31] and we assume that the measured surface tension yields the monolayer concentration according to equation 3.5[28]. Figure 3.32 shows a relatively close overlap between $\gamma(c)$ and $\gamma_m(c)$. There may be a systematic difference but due to measurement errors leaving some ambiguity. Therefore the assumptions are again realistic in equilibrium and the use of the oscillating bubble combined with the SSHG is further motivated.

It is important to mention that the scattering in the SSHG data is higher for PyBr solutions than for HC_8 solutions, due to different limitations. First, the fundamental beam used to probe the surface possesses a lower power. Also, the PyBr molecule exhibits a lower hyperpolarizability due to the shorter conjugated system. Finally, we notice a considerable photobleaching of the molecules during the measurements. This photobleaching could be observed as a decrease in the SH signal upon exposure to pump light. After 5-10 minutes of exposure, the SH signal of PyBr was similar in magnitude to the SH signal of water, as it is presented in figure 3.33. Nevertheless, the results obtained in the following section could be reproduced successfully.
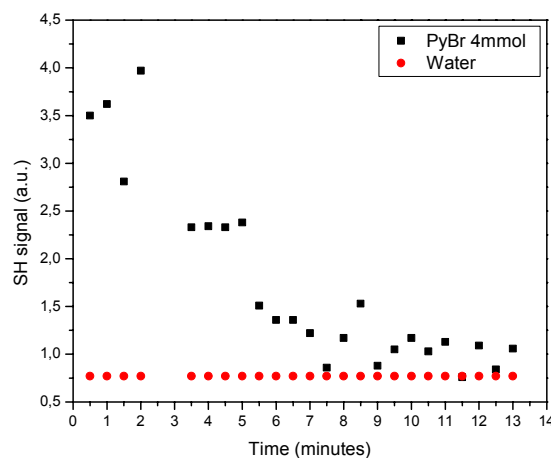
Figure 3.33 Time effect on the SH signal for a 4 mmol PyBr solution.

SHG measurements on an Oscillating Bubble

The SH signal coming from the tip of a bubble created in a surface viscoelastic PyBr solution is shown as a function of the phase angle ψ in figure 3.34 for a 1mmol and a 4 mmol solution.
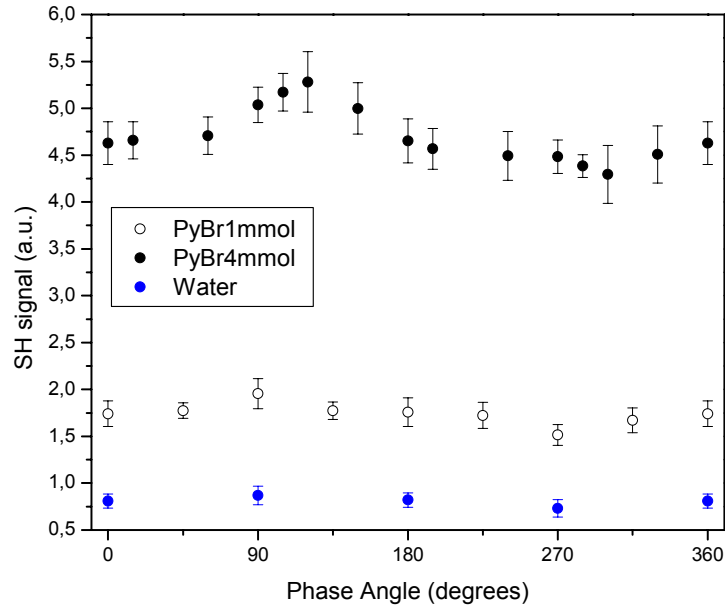
Figure 3.34   SH signal as a function of the phase angle Ψ for water, 1 mmol and 4 mmol PyBr solutions.

The relative magnitude of the measured concentration of surfactants in the monolayer during oscillation, calculated from the data presented in figure 3.34, is presented in table 3.2. We observe that in the two cases, $\Delta\Gamma_m/\Gamma_m$ is smaller than the relative magnitude of the surface area (0,18 ± 0,04). Moreover, the relative change of the concentration of surfactants in the monolayer is smallest for the highest concentration.

PyBr concentration	$\Delta\Gamma_m/\Gamma_m$
1mmol	0,09 ± 0,02
4mmol	0,03 ± 0,01

Table 3.2 $\Delta\Gamma_m/\Gamma_m$ calculated for different concentrations of PyBr solutions, for a frequency of 40 Hz.

The SSHG onto oscillating bubble allows the independent verification of the surface models because we can compare the modulus description

$$\Delta\gamma = \varepsilon(f,c)\frac{\Delta A}{A} = E(f,c)\exp(i\varphi(f,c))\frac{\Delta A}{A} \qquad (3.11)$$

of the bubble measurements and the relation for the monolayer concentration

$$\frac{\Delta\Gamma_m(f,c)}{\Gamma_m} = -C(f,c)\exp(i\alpha(f,c))\frac{\Delta A}{A} \qquad (3.12)$$

of the SHG measurements. For probing the effects, the following expressions derived from the experimental results were determined:

$$\Delta A^*(\Psi) = \Delta A/|\Delta A| = -\sin(\Psi) \qquad (3.13)$$

is the normalized area change,

$$\Gamma^*(\Psi) = |A/\Delta A| \, (\Delta\Gamma_{SHG}/\Gamma_{SHG}) = |A/\Delta A| \, ((SH(\Psi))^{1/2} - \Gamma_{SHG})/\Gamma_{SHG}, \qquad (3.14)$$

represents the normalized change in monolayer concentration and where

$$\Gamma_{shg} = \frac{1}{N}\sum_{n=1}^{N}(SH(\Psi)_n)^{1/2} \qquad (3.15)$$

Finally,

$$\Delta\gamma^*(\Psi) = |\varepsilon(f)/\varepsilon_m| \sin(\Psi-\varphi) \qquad (3.16)$$

describes the change in dynamic surface tension.

In these equations, $\Psi = f*t*360°$ represents the phase of the area change, $SH(\Psi)$ the SHG intensity, and Γ_{SHG} the mean value of the monolayer concentration, which is proportional to the average of $(SH(\Psi))^{1/2}$.

Figure 3.35 and figure 3.36 show the curves ΔA^*, Γ^*, and $\Delta\gamma^*$ for 1 mM and 4 mM PyBr solutions, respectively. Since it is a cationic surfactant which surface behaves viscoelastic in the low and the higher frequency range, we must take into account the bulk diffusion as well as the intrinsic surface viscosity. The results of the fitting are compiled in table 3.3.
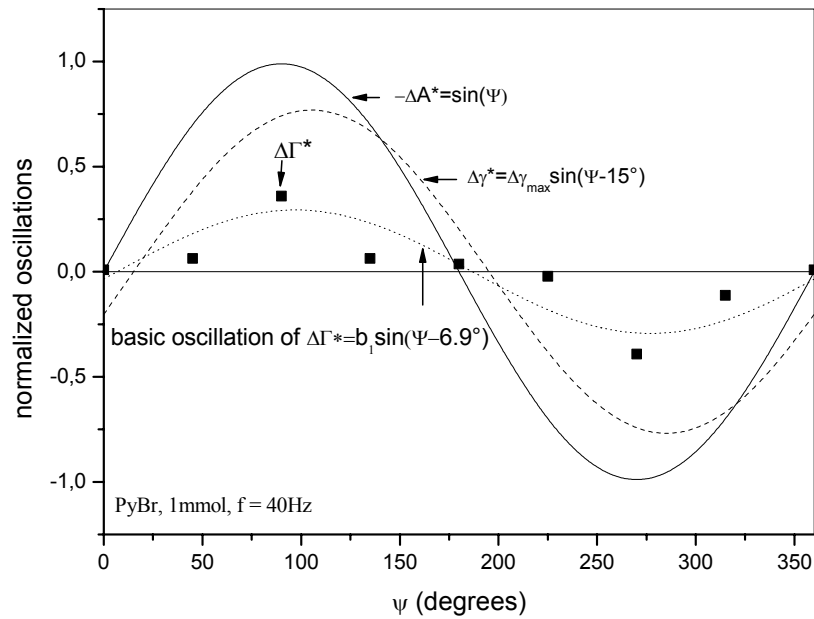
Figure 3.35 ΔA^*, Γ^*, and $\Delta\gamma^*$ calculated for a 1mmol PyBr solution.
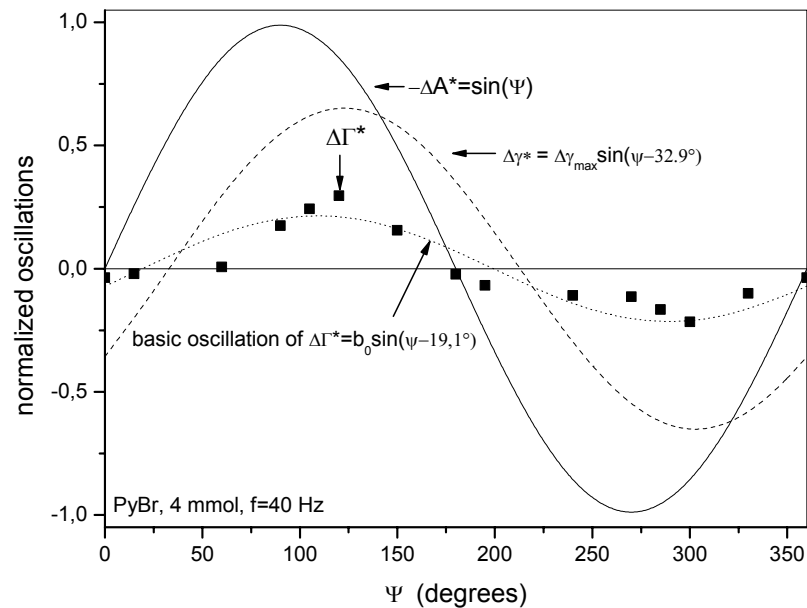
Figure 3.36 ΔA^*, Γ^*, and $\Delta\gamma^*$ calculated for a 4mmol PyBr solution.

Substance	concentration	ε_m	ω_m	κ	$\sim k$	$\sim I$
		mN/m	s^{-1}	mNs/m	cm s^{-1}	mol cm^{-2} s^{-1}
PyBr	1 mmol	48.1	58	0.0013	0.22	$0.22*10^{-6}$
PyBr	4 mmol	26.8	570	0.0050	0.033	$0.13*10^{-6}$

Table 3.3   Values obtained from the fitting for the 1 mmol and 4 mmol PyBr solutions.

To understand the results presented in figure 3.35 and 3.36, it makes the explanation easier if we start from an insoluble system. In this case, the ΔA^*, Γ^*, and $\Delta\gamma^*$ curves would have all the same amplitude, as well as no phase shift between them. We would then conclude that there are no dissipative processes occurring in the monolayer. If the amplitude of Γ^* and $\Delta\gamma^*$ would be smaller than ΔA^*, then we would need further explanation.

In the case of a soluble system presenting elastic properties, as for instance F381 or HC$_8$ solutions, the situation would be different. In the case of low concentration, the curves would be identical to the case of an insoluble monolayer. However, when analyzing higher concentrations, we would observe that the amplitude of Γ^* and $\Delta\gamma^*$ becomes smaller than ΔA^* for the complete surface. Thus, to explain this effect correctly, we have to include a sublayer in the model. The oscillating bubble experiments as well as the measurements done with the SHG onto an oscillating bubble prove this extended version of the model in the medium frequency range.

The system presented in figure 3.35 and 3.36 shows viscoelastic behaviour. Oscillating bubble measurement has proved this. Surface viscoelasticity is a consequence of dissipative processes. The question that needs to be answered regarding this fact is the location of these dissipative processes. In the case of low frequencies, (smaller than 10Hz), the dissipative processes arise from the diffusion to the bulk and can be described by the LvdTH model. However, for higher frequencies, from 10-500 Hz, we believe that the dissipative processes are located in the surface layer. This is what we tried to check by performing the SHG onto an oscillating bubble on PyBr solutions. To clearly see the effect, it would have been better to work at a frequency of 200 Hz. However, due to

experimental limitations, we could only work at 40Hz. Therefore the effect is small and difficult to analyze.

Moreover, our surfactant is ionic. This means that we would have to take into account an extended electric layer in our model and therefore these molecular motions in the sublayer are not completely clear.

As presented in figure 3.35 and 3.36, the amplitude of Γ^* is much smaller than ΔA^*, and also smaller than $\Delta\gamma^*$ for the 2 concentrations. This hints for an influence on the sublayer to the dynamic surface tension model.

The phase angle between Γ^* and $\Delta\gamma^*$ must be large, and this is due to the viscous effect ($i\omega\kappa$). In our case, this is verified qualitatively. We cannot, however, discuss it quantitatively because the calculation has been done for different parameters than used in the experiment. We worked at 40 Hz, but the calculation has been done at the high frequency limit.

The results presented in this section show that the viscous effect is present in the case of the PyBr solution. Moreover, the results from the 4 mmol PyBr solution give a hint that the dissipative processes associated to a viscoelastic system in the medium frequency range come from the sublayer. However, more experiments have to be completed in a higher frequency range to get a clearer and more complete picture of the system.

3.9   CONCLUSIONS

SSHG experiments on an oscillating bubble were performed in the medium frequency range on a surface elastic system, the HC_8, and on a surface viscoelastic system, the PyBr solutions. The optical setup allows for direct measurements of the concentration of soluble surfactants in the monolayer, Γ_m, during oscillation. The measurements were done at frequencies where the bulk-surface diffusion of HC_8 solutions is negligible.

In the case of the elastic system, the results obtained show that for low concentrated HC_8 solutions, the relative change in Γ_m during oscillation, $\Delta\Gamma_m/\Gamma_m$, was equal to the relative change in surface area during oscillation, $\Delta A/A$, whereas close to the solubility limit, the solutions show a distinct reduction of $\Delta\Gamma_m/\Gamma_m$. Moreover, the oscillations of $\Delta\Gamma_m/\Gamma_m$ and $-\Delta A/A$ remain in phase.

In the case of the viscoelastic system, we observe a phase shift between $\Delta\Gamma_m/\Gamma_m$ and $\Delta A/A$ for higher concentration of PyBr solutions. Comparing this phase angle with the phase of the surface dilatational modulus reveals the influence of the bulk diffusion and the surface dilatational viscosity.

We can explain the data by a molecular exchange process described through a modified version of the LvdTH model. In this model, the surface is assumed to consist of a monolayer and an adjacent sublayer. If the molecular exchange between both structures is fast enough, the surface response remains elastic as long as the diffusion is negligible. This has been demonstrated by measurements of the surface dilatational modulus of HC_8 solutions and verified by SHG measurements.

For lower molecular exchange rates, an expansion or compression of the surface leads to a non-equilibrium state between the internal structures of the surface layer. The measured surface dilatational modulus of PyBr solutions shows such behaviour. The SHG measurements verify the model too. The comparison between the phase angles of both measurements hints towards a non-equilibrium state within the surface.

Thus, the observed effects require the introduction of an intrinsic surface dilatational viscosity, κ, which leads to the additional term, $i\kappa\omega$, in the equation describing the

modulus. The viscoelastic behaviour of such surfactant systems implies that energy is dissipated not only in the bulk, but also in the surface. The results obtained also hint towards this conclusion.

Some hypotheses exist to describe the dissipative loss created by the molecular exchanges in the case of a viscoelastic system. Recently, our group published interesting results leading to an explanation concerning this effect. In fact, the dissipative process could very well come from the breakage of the –OH bonds of the water molecules[8]. This explanation hints towards a correlation between foamability and surface viscoelasticity in the medium frequency range.

Other theories exist, among them one considering reorientation processes inside the monolayer as a key feature to explain the origin of the intrinsic dilatational viscosity as well as dissipative processes. The next chapter considers this model, and brings some new information regarding it.

REFERENCES

1. Fruhner, H., Wantke, K. D., Lunkenheimer, K. *Colloids and Surfaces A: Physicochemical and Engineering Aspects* **1999**, *162*, 193.

2. Pugh, R. J. Foams and Foaming. In *Handbook of Applied Surface and Colloid Chemistry*; Holmberg, K., Ed.; John Wiley & Sons, Ltd, 2001; pp 23.

3. Wantke, K., Fruhner, H., Fang, J., Lunkenheimer, K.,. *J. Coll. Int. Sci.* **1998**, *208*, 34.

4. Örtegren, J., Wantke, K.-D., Motschmann, H. *Rev. Sci. Inst.* **2003**, *74*, 5167.

5. Drenckhan, W., Cox, S.J., Delaney, G., Holste H., Weaire, D., Kern, N. *Coll. Surf. A: Physicochem. Eng. Aspects* **2005**, *263*.

6. Fruhner, H., Wantke, K. D. *Coll. Polym. Sci.* **2001**, *279*, 898.

7. Engels, T., von Rybinski, W., Schmiedel, P. *Prog. Colloid Polymer Sci.* **1998**, *111*, 117.

8. Koelsch, P., Motschmann, H. *Langmuir* **2005**, *21*, 6265.

9. Möbius, D., Miller, R. (Eds) *Novel methods to study Interfacial Layers*; Elsevier: Amsterdam, 2001; Vol. 11.

10. Binks, B. P. E. Modern Characterization Methods of Surfactant Systems; Marcel Dekker: New-York, 1999; Vol. 83.

11. Langevin, D., Griesmar, C. *J. Phys. D: Appl. Phys.* **1980**, *13*, 1189.

12. Miller, R., Policova, Z., Sedev, R., Neumann, A.W. *Colloids Surfaces* **1993**, *76*, 179.

13. Leser, M. E., Acquistapace, S., Cagna, S., Makievski, A., Miller R. *Colloids and Surfaces A: Physicochemical and Engineering Aspects* **2005**, *25*, 2611.

14. van den Tempel, M., Lucassen-Reynders, E.H. *Adv. Coll. Inter. Sci.* **1983**, *18*, 281.

15. van den Tempel, M., van de Riet, J. *J. Chem. Phys.* **1964**, *42*, 2769.

16. Lucassen-Reynders, E. H., Lucassen, J. *Adv. Coll. Inter. Sci.* **1969**, *2*, 347.

17. Lucassen-Reynders, E. H. *J. Coll. Int. Sci.* **1973**, *242*, 573.

18. Lucassen, J., van den Tempel, M. *Chem. Eng. Sci.* **1972**, *27*, 1283.

19. Fang, J., Wantke, K.-D., Lunkenheimer, K. *J. Coll. Int. Sci.* **1996**, *182*, 31.

20. Lucassen-Reynders, E. H. *Physical Chemisty of Surfactant Action*; Marcel Dekker: New-York, 1981; Vol. 11.

21. Kretzschmar, G., Lunkenheimer, K. *Ber. Bunsenges. Phys. Chem.* **1970**, *74*, 1064.

22. Wantke, K.-D., Miller, R., Lunkenheimer, K. *Z. Phys. Chem. (Leipzig)* **1980**, *261*, 1177.

23. Wantke, K.-D., Lunkenheimer, K., Hempt, C. *J. Coll. Int. Sci.* **1993**, *159*, 28.

24. Lucassen, E. H., Lucassen, J. *J. Adv. Coll. Inter. Sci.* **1969**, *2*, 347.

25. Lucassen, J., Hansen, R.S.,. *J. Coll. Int. Sci.* **1967**, *23*, 319.

26. Fruhner, H., Wantke, K.-D. *Colloids and Surfaces A: Physicochemical and Engineering Aspects* **1996**, *114*, 53.

27. Wantke, K., Fruhner, H.,. *J. Coll. Int. Sci.* **2001**, *237*, 185.

28. Örtegren, J., Wantke, K.-D., Motschmann, H., Möhwald, H. *J. Coll. Int. Sci.* **2004**, *279*, 266.

29. Simpson, G. J., Rowlen, K.L. *JACS* **1999**, *121*, 2635.

30. Lehmann, S., Busse, G., Kahlweit, M., Stolle, R., Simon, F., Marowsky, G. *Langmuir* **1995**, *11*, 1174.

31. Vogel, V., Mullin. C.S., Shen. Y.R. *Langmuir* **1991**, *7*, 1222.

32. Andrews, D. L., Allcock, P., Demidov, A.A. *Chem. Phys.* **1995**, *190*, 1.

CHAPTER 4

SHG USED AS A PUMP-PROBE EXPERIMENT: ON THE PICOSECOND DYNAMICS OF MOLECULES

The results presented in Chapter 3 proved experimentally that the addition of a sublayer to the LvdTH model overcomes its imperfections. The dissipative process that gives rises to the imaginary part of the surface dilatational modulus is due to the molecular exchanges between the sublayer and the topmost monolayer. On a molecular level, our group demonstrated that the exchange process leads to different hydration states accompanied by a breaking of –OH water bonds[1]. Nevertheless, as mentioned shortly in the previous chapter, another theory has been proposed in order to explain surface viscoelastic behaviours. Hence, we challenge this approach.

The molecular reorientation model, described first by Fainerman et al[2] and further developed by Miller et al[3] and Ravera et al [4,5], proposes a two-states adsorption of molecules at the air-water interface. This model is able to explain the functional dependence of the modulus provided that the molecular reorientation process occurs in the millisecond time regime. This model has brought interest through the scientific community, but remains controversial due to the time frame of the reorientation process, which must take place, in our opinion, in the picosecond time regime[6].

Pump-Probe SHG allows, among others, the studies of interfacial molecular reorientations[7]. Taking advantage of this technique, we verified experimentally the proposed molecular reorientation model by designing a proper Pump-Probe SHG experiment. The present chapter describes first the molecular reorientation model and then the experimental setup. Finally, we present the first results obtained with the HC_8.

4.1   THE MOLECULAR REORIENTATION MODEL

It is accepted that the principal process governing the time dependence of surface pressure for most surfactant systems is diffusion. It has also been observed that for some surfactant systems, the diffusion-controlled adsorption model is not adequate to describe experimental data. To explain the adsorption dynamics of these systems, different phenomena have been put forward. In this thesis, the addition of a sublayer has already been discussed in the previous chapter.

The idea that reorganization processes, such as reorientation or conformational modifications of adsorbed molecules, can occur within the surface layer for some surfactant systems has been theoretically assessed[2-5]. Some indirect proofs on polyoxyethylated non-ionic surfactants[8-10] and proteins[11] have been described in the literature.

The model, shown in figure 4.1, considers two possible states for the adsorbed molecules, characterized by different surface molecular areas and surface activity. The state 1, with a larger surface area, corresponds to molecules adsorbed oriented along the surfaces and prevails at low-pressure surface. The state 2, characterized by a smaller surface area, corresponding to molecules normally oriented with respect to the surface, prevails when the surface pressure, e.g., the surface coverage, is high[4].

According to the literature, the utilization of a two-state isotherm, in the framework of the diffusion-controlled adsorption, provides a good description of the ageing of freshly produced interfaces. This means that, in these cases, processes internal to the adsorbed layer with changing surface area, such as orientation, should exist, but with characteristic times shorter than the diffusion relaxation time.

Figure 4.1   The molecular reorientation model, described by Ravera *et al*[4,5].

The mathematical expression proposes that the considered surfactant, once adsorbed to the surface, can adopt two different states, 1 and 2, characterized by the surface molar areas ω_1 and ω_2, related to the different surface activities. These two states are expected to correspond to two different orientations with respect to the surface, so that the process internal to the adsorbed layer is in fact an orientation process. The mathematical development leads to the following equation:

$$\frac{\Gamma_1}{\Gamma_2} = \beta \exp\left[-\frac{\Pi}{RT}(\omega_1 - \omega_2)\right] \tag{4.1}$$

where Γ_1 and Γ_2 are the adsorption states for the two different states, R is the gas constant, T is the absolute temperature, $\Pi = \sigma_0 - \sigma$ is the surface pressure, σ_0 and σ are the surface tensions of the solvent and the solution, respectively, $\beta = (\omega_1 - \omega_2)^{\alpha}$, and α is a constant (for a=0 the surface activity is independent from the molar surface area, and for a≥0 the molecules adsorbed in the state with the larger surface area have a higher surface activity[4]). The parameter β considers that the adsorption activity of surfactant molecules in state 1 is larger than in state 2. This equation is only valid under orientation equilibrium.

Thus, according to this model, a complete description of the evolution of surface pressure during adsorption involves three dynamic processes, i.e., the adsorption-desorption exchange between surface and bulk, the change in the orientation of adsorbed molecules and the diffusion process in the bulk.

In this model, the adsorption is considered to proceed in the following way. The molecules, which are randomly oriented in the bulk, adsorb either in the state 1 or 2, with a probability χ and $\chi-1$, respectively. This induces a diffusion flux in the bulk. Meanwhile, the distribution of freshly adsorbed molecules between the two states is out of equilibrium, and is then attained by the reorientation process.

The three processes have three distinct characteristic times and can be separately considered when the other processes are in equilibrium, or have a much different time. Therefore, the time evolution of the adsorption states of Γ_1 and Γ_2 is described by

$$\frac{d\Gamma_1}{dt} = \Phi_{a1} - \Phi_{d1} + \Phi_{or} \tag{4.2}$$

$$\frac{d\Gamma_2}{dt} = \Phi_{a2} - \Phi_{d2} + \Phi_{or} \tag{4.3}$$

where Φ_a and Φ_d stand for adsorption and desorption fluxes, and Φ_{or} is the contribution of the orientation which is assumed to be a kinetic process involving only the adsorbed molecules. Thus, for a non-equilibrium state, the reorientation process is described by the linear kinetic equation:

$$\frac{d\Gamma_2}{dt} = \nu_{or}\left(\Gamma_1 - \frac{\Gamma_1^0}{\Gamma_2^0}\Gamma_2\right) \tag{4.4}$$

with ν_{or} being the reorientation time, expressed in Hz (1/s). According to the results obtained in the literature[12], the reorientation time is in the order of magnitude of 10^{-3} to 10^{-4} seconds. This is very controversial in the sense that for most of the reorientation processes found in the literature, the results are always 5 or 6 orders of magnitude higher, which means reorientation times in the order of nano or picosecond[13-15]. The use of a pump-probe experiment on surfactant systems could shed some light on this discrepancy.

4.2   PUMP-PROBE SHG

An interesting property of the SHG coming from an interface is its almost instantaneous response time. This possibility, combined with the fact that pulsed lasers are normally used in SSHG experiments, provides a method to make time-resolved measurements of surface processes using a pump-probe system.

The concept of pump-probe has been utilized in the last twenty years with a number of experiments, on time scales ranging from ten of seconds down hundred of femtoseconds[7,13-17]. Many examples can be found in the literature, for different time scales: population recovery, giving the excited-state lifetime is an example of nanoseconds dynamics. The orientational motion, generally in the picoseconds order,

gives the reorientationnal time and electronic excited-state solvation allows one to get the solvation time, which is in the scale of femtoseconds.

The principle of our pump-probe experiment is quite simple and is presented in figure 4.2. Two pulses hit the surface at different times. The first one is linearly polarized and used to excite the adsorbed molecules. The strength of the absorption is proportional to the scalar product between the molecule transition moment and the surface electric field vector as presented in figure 4.2. As a result of the absorption, the hyperpolarisability of the molecule is changed. This is monitored by detecting SHG with a probe-pulse. The pump can excite more than a monolayer. However, due to the inherence of it specificity, the probe monitors only the adsorbed species. This probe measures two different parameters: surface population or orientation motions. This experiment covers a time-frame from 0- 800 picoseconds. Experimentally, this easily achieved by changing the delay time between the pump and the probe pulses. The recovery of the signal measures the orientational dynamics.

1st pulse : Adsorption   **2nd pulse : SHG**

$\vec{\mu} \cdot \vec{E} = 0$

$\vec{\mu} \cdot \vec{E} = \text{max}$
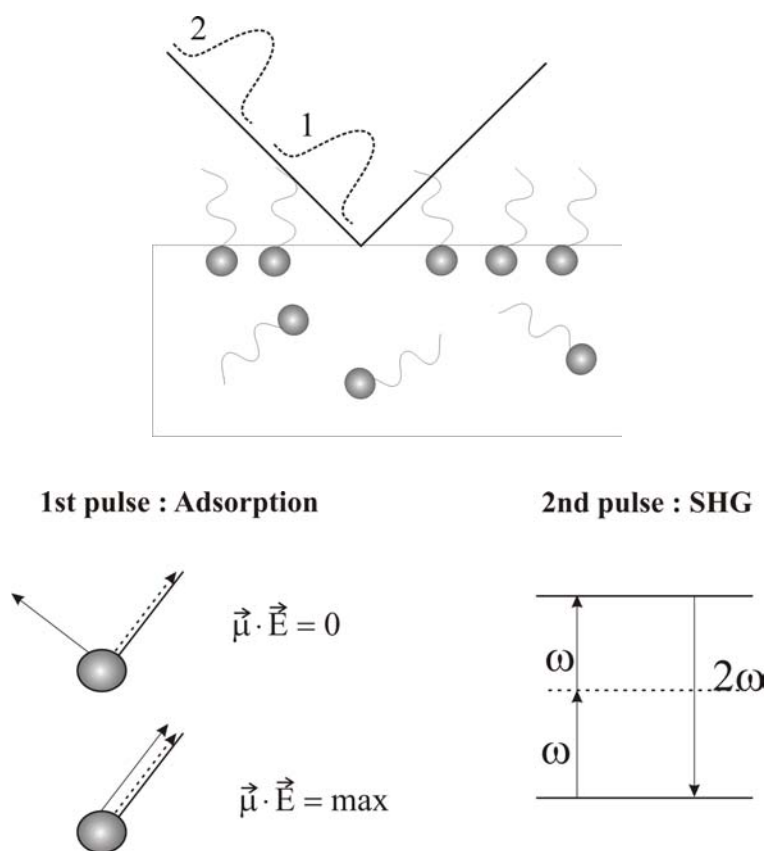
Figure 4.2   Principle of the pump-probe SHG.

Such a system allows one to perform two different types of experiments. In a first case, it should allow the determination of the width of the orientation distribution and to compare it with existing theoretical models. To realize such an experiment, one has to measure the intensity of the SH signal as a function of the polarization of the incoming beam for very small delay times.

On the other hand, it is possible to study the dynamics of orientation recovery. In that case, the intensity of the signal is measured as a function of the delay between the pump and the probe. In order to verify the two-states model presented above, we performed an experiment in this direction.

4.3   EXPERIMENTAL SETUP

The setup built for the pump-probe experiment is depicted in figure 4.3 and figure 4.4. The 355nm tripled-light is used as the pump, whereas the 532nm doubled-light acts as the probe. Both beams are coming from the Nd:YAG laser described in the previous sections. Both beams possess 35 ps duration.

The pump beam is directed through a series of mirrors before going through a Soleil-Babinet compensator. A Soleil-Babinet compensator is a continuously adjustable retardation plate allowing adjusting any arbitrary retardation. Here, it is used as a half-wave plate. The plane of polarization of linearly polarized light can be turned without loosing intensity.

The pump-beam is then directed towards the surface by passing through a pinhole and a lens (f = 200). The beam is focused slightly before the surface. Finally, the beam ends in a black hole, preventing scattered light.

The probe-beam passes first through a series of half-wave plate-polarizer-half-wave plate before going through a delay line composed of a Dove prism. The light is then directed towards the sample by passing first through a pinhole and then through a lens (f=100) that focuses the beam onto the surface of the solution

The pump and the probe must touch the surface at the same place, and in the same place. Thus, we have a spatial and temporal overlap. This remains the main difficulty of this experiment. The two beams touch the surface with a different incidence angle, as well as from a different direction; this requires a careful adjustm. The angle of incidence to the normal of the pump-beam is 65 degrees and for the probe-beam 55 degrees. The angle γ between the two beams is 30 degrees. This is also shown in figure 4.4.

After touching the sample, the SH signal (266nm) is detected via a photomultiplier tube (R1398, Hamamatsu) with a quantum efficiency of 15%, and a cathode radiant sensitivity of 35 mAW^{-1} at 266 nm. The supply voltage over the photomultiplier tube was 1850 V (V5D, Seefelder Messtechnik). The detected signal was processed by an oscilloscope (54720D, Hewlett-Packard) and integrated by a computer program. The purity of the signal is assured by a combination of a narrow-band interference filter (BP266) as well as color filters (UG11 and UG5), presented in figure 3.15.
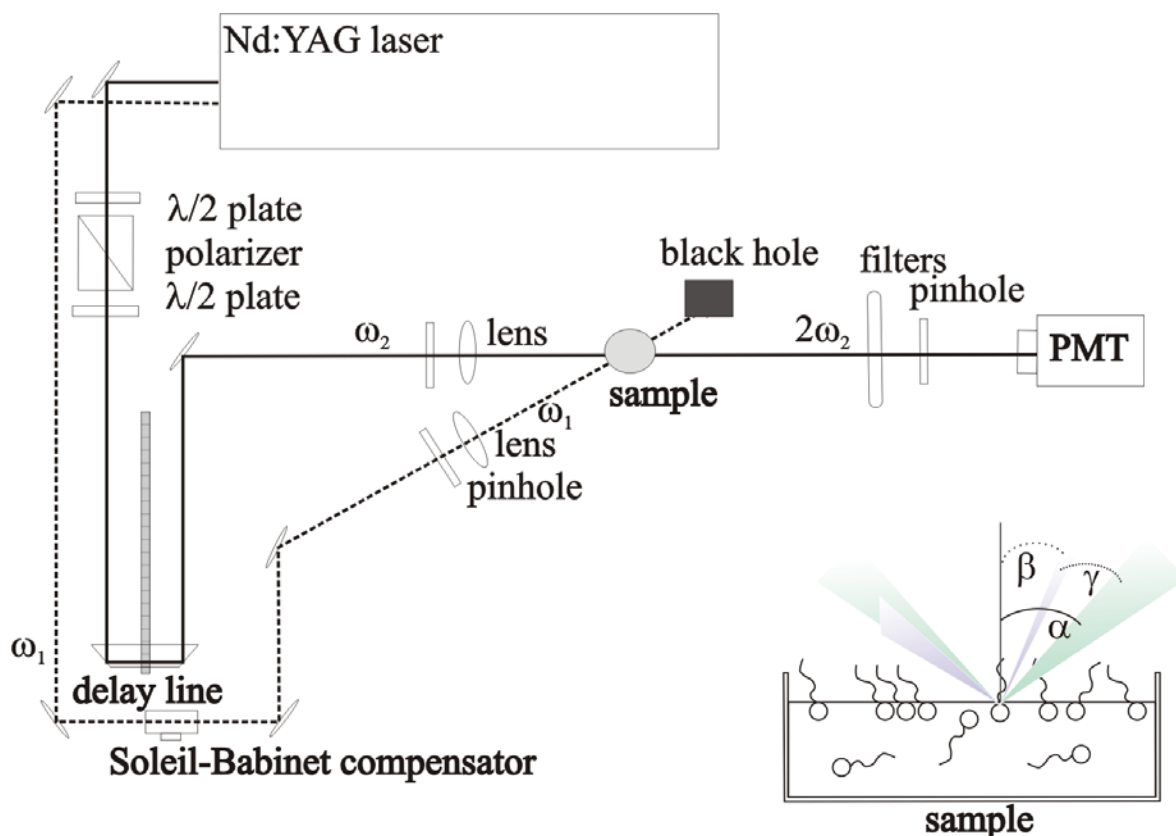
Figure 4.3   Setup for the pump-probe experiment.
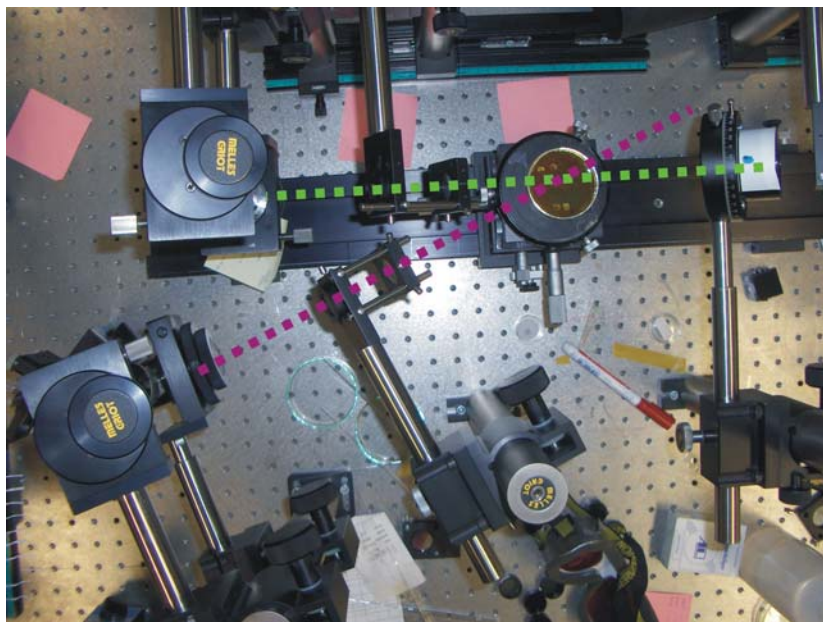
Figure 4.4 Picture of the pump-probe setup (probe: green, pump: violet).

4.4 RESULTS & DISCUSSION

The first results obtained with the pump-probe experiment are presented in this section. We utilized the HC_8 surfactant, depicted in figure 3.12, as it has been used as a model system for elastic surfactants in the previous chapter. Moreover, the UV-VIS absorption curve of this molecule is quite suitable for the wavelengths used in our setup; the absorption at 532 nm and 355 nm are quite minimal, as it can be observed in figure 3.10.

The experiment has been performed on a HC_8 aqueous solution of approximately 800 μmol. The experiment could be reproduced twice, yielding the same result. In the case of this measurement, the intensity of the probe and the pump had a ratio of 2:1, with 0,003 W for the 532 nm beam and 0,0015 W for the 355 nm beam, respectively.

The polarizer of the probe-beam was set to magic angle[18], whereas the pump-beam and the analyser were p-polarized. The result obtained is presented in figure 4.5.

The plot shows SH signal (a.u.) on the y-axis (range 4 to 8) versus Time (ps) on the x-axis (range 0 to 600), with red data points labeled HC_8 and a dotted exponential fit line. The fit equation is shown:

$$y = 6{,}1 - 1{,}64\,e^{(-x/127)}$$
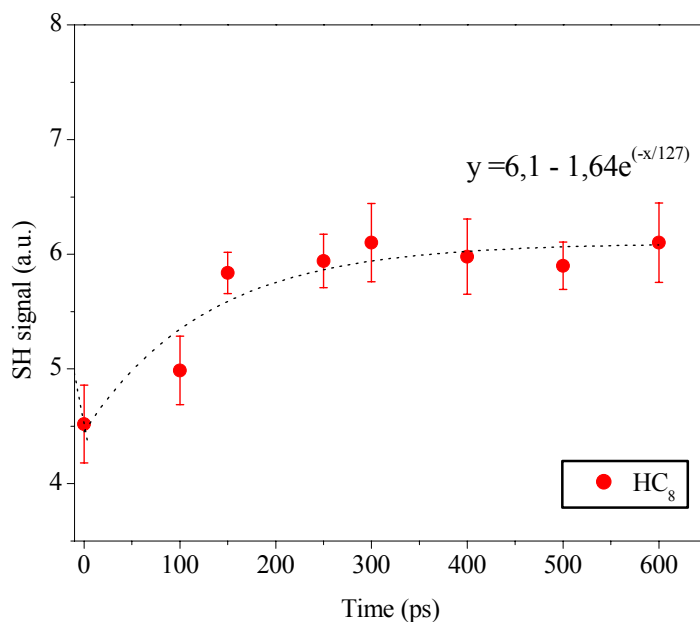
Figure 4.5   Pump-probe SSHG of the HC_8 at the air-water interface. The dotted line is an exponential fit.

The reorientation time has been calculated by applying the following equation to the curve:

$$y = A_1 e^{(-x/\tau)} \tag{4.5}$$

with τ being the reorientation time. From the calculated fit, we obtained $\tau = 127 \pm 40$ ps. The error bars refer to the analysis of several independent measurements. However, it gives a good idea of the order of magnitude of the molecular reorientation. Thus we can conclude that the dynamics of reorientation of the HC_8 at the air-water interface are in the 100 picoseconds range.

The results obtained are in accordance with what has been found in the literature. For instance, Morgenthaler *et al*[15] studied the reorientation dynamics of the rhodamine 110 on silica. The result they obtained was in the same order of magnitude as we have in the present experiment. Moreover, Castro *et al*[19] and Zimdars *et al*[14,20] published interesting results concerning the reorientation of surfactant at the air-water interface. Again, the results obtained are pointing in the same direction as what is presented here.

This is of course the first result obtained with our model-system, and more experiments have to be performed. For instance, one should modify the polarization of the incoming probe-beam to see the effect on the recovery time. In any case, according to this result showing 6 orders of magnitude smaller reorientation time, the reorientation model doesn't hold and would have to be modified. Being able to measure *in situ* and in real time the molecular dynamics of the reorientation of surfactant at the air-water interface yields a direct proof to this statement.

4.5   CONCLUSIONS

A model describing molecular reorientations has been proposed in order to explain the discrepancies of the original LvdTH model and to describe the dissipative processes associated to intrinsic surface viscoelasticity. According to this theory, the reorientation processes take place in a millisecond time-scale. This has been subject to controversy.

We built a pump-probe SSHG experiment and performed a measurement onto HC_8 surfactant to verify the speed of reorientation processes. The result demonstrates that the reorientation dynamics for this molecule occurs in the 100 picoseconds time-scale. We observed here a real inconsistency between the model discussed in the previous section and the experimental results obtained here. In fact, the experimental time frame of reorientation is 6 orders of magnitude faster than the one obtained with indirect experimental measurements.

The pump-probe SSHG experiment has proved to be useful to bring some light onto a controversial topic. Some questions remain, but according to the results obtained, we can conclude that the model doesn't represent the reality.

In the near future, we would like to use the pump-probe experiment to answer another fundamental question. By varying the plane of polarization of the linearly polarized incoming pump-beam, we should be able to quantify the width of the mean orientation of the surfactants at the air-water interface. This would provide a fundamental structural parameter.

REFERENCES

1.   Koelsch, P., Motschmann, H. *Langmuir* **2005**, *21*, 6265.

2.   Fainerman, V. B., Lucassen-Reynders, E.H., Miller, R. *Colloids and Surfaces A: Physicochemical and Engineering Aspects* **1998**, *143*, 141.

3.   Miller, R., Aksenenko, E. V., Fainerman, V.B. *Journal of Colloids and Interface Science* **2001**, *236*, 35.

4.   Ravera, F., Liggieri, L., Miller, R. *Colloids and Surfaces A: Physicochemical and Engineering Aspects* **2000**, *175*, 51.

5.   Ravera, F., Ferrari, M., Miller, R., Liggieri, L. *J. Phys. Chem. B* **2001**, *105*, 195.

6.   *Faraday Discussions* **2005**, *129*, 179.

7.   Eisenthal, K. B. *Annu. Rev. Phys. Chem.* **1992**, *43*, 627.

8.   Liggieri, L., Ferrari, M., Massa, A., Ravera, F. *Colloids and Surfaces A: Physicochemical and Engineering Aspects* **1999**, *156*, 455.

9.   Ferrari, M., Liggieri, L., Ravera, F. *J. Phys. Chem. B* **1998**, *102*, 10521.

10. Miller, R., Aksenenko, E. V., Liggieri, L., Ravera, F'', Ferrari, M., Fainerman, V.B. *Langmuir* **1999**, *15*, 1328.

11. Miller, R., Fainerman, V.B., Makievski, A., Krägel, J. Grigoriev, D.O., Kazakov, V.N., Sinyachenki, O.V. *Ad. Coll. Int. Sci.* **2000**, *86*, 39.

12. Liggieri, L., Ferrari, M., Mondelli, D., Ravera, F. *Faraday Discussions* **2005**, *129*, 125.

13. Antoine, R., Tamburello-Luca, A.A., Hébert, Ph., Brevet, P.F., Girault, H.H. *Chem. Phys. Let.* **1998**, *228*, 138.

14. Zimdars, D., Dadap, J.I., Eisenthal, K.B., Heinz, T.F. *J. Phys. Chem. B* **1999**, *103*, 3425.

15. Morgenthaler, M. J. E., Meech, S.R. *J. Phys. Chem.* **1996**, *100*, 3323.

16. Eisenthal, K. B. *J. Phys. Chem.* **1996**, *100*, 12997.

17. Steinhurst, D. A., Baronavski, A.P., Owrytsky, C. *J. Phys. Chem.* **2002**, *106*, 3160.

18. Simpson, G. J., Rowlen, K.L. *JACS* **1999**, *121*, 2635.

19. Castro, A., Sitzmann, E.V., Zhand, D., Eisenthal, K.B. *J. Phys. Chem.* **1991**, *95*, 6752.

20.   Zimdars, D., Eisenthal, K.B. *J. Phys. Chem. B* **2001**, *105*, 3993.

ANNEXE 1

Abbreviation List

Abbreviation	Signification
BAM	Brewster angle microscopy
CCD	charge coupled device
CMC	critical micellar concentration
DC	direct current
DFG	difference frequency generation
EELS	electron energy loss spectroscopy
LEED	low energy electron diffraction
LvdTH	Lucassen-van den Tempel-Hanse
Nd:YAG	neodynium: yttrium–aluminum–garnet
NLO	nonlinear optics
OB	oscillating bubble
OPG	optical parametric generator
SFG	sum frequency generation
SHG	second harmonic generation
SHG-OB	second harmonic generation on an oscillating bubble
SSHG	surface second harmonic generation
STM	scanning tunelling microscopy
UV	ultraviolet
UV-VIS	ultraviolet-visible
XPS	X-ray photoelectron spectroscopy

Chemical abbreviations

Abbreviation	Chemical
CTAB	hexadecyl-trimethylaminonium bromide
F381	6-((2-hydroxyethyl)-{2[4-(4-trifluoromethyl-phenylazo)-phenoxy]-ethyl}-amino)-hexane-1,2,3,4,5-pentaol
HCn	N-n-alkyl-4'-(dimethylamino)-stilbazium bromide
HC5	N-5-alkyl-4'-(dimethylamino)-stilbazium bromide
HC6	N-6-alkyl-4'-(dimethylamino)-stilbazium bromide
HC7	N-7-alkyl-4'-(dimethylamino)-stilbazium bromide
HC8	N-8-alkyl-4'-(dimethylamino)-stilbazium bromide
KBr	potassium bromide
PyBr	dodecyl-dimethylaminopyridinium bromide

ZUSAMMENFASSUNG

Amphiphile vereinen zwei gegensätzliche Strukturelemente in einem Molekül, eine hydrophile Kopfgruppe und ein hydrophobe, meist aliphatische Kette. Aufgrund der molekularen Asymmetrie erfolgt eine spontane Adsorption an der Wasser-Luft Grenzfläche. Die Adsorptionsschicht verändert die makroskopischen Eigenschaften des Materials, z.B. die Grenzflächenspannung wird erniedrigt. Amphiphile sind zentrale Bauelemente der Kolloid- und Grenzflächenforschung, die Phänomene, wie Schäume ermöglichen.

Eine Schaumlamelle besteht aus einem dünnen Wasserfilm, der durch zwei Adsorptionsschichten stabilisiert wird. Die Stabilität der Lamelle wird durch die Grenzflächenrheologie entscheidend geprägt. Die wesentliche makroskopische Größe in diesem Zusammenhang ist das so genannte Grenzflächendilatationsmodul E. Es beschreibt die Fähigkeit des Systems die Gleichgewichtsgrenzflächenspannung nach einer Expansion oder Dilatation der Adsorptionschicht wieder herzustellen. Das Modul E ist eine komplexe Größe, in dem der Imaginärteil direkt mit der Schaumstabilität korreliert.

Diese Arbeit widmet sich der Grenzflächenrheologie. In der Literatur werden zwei kontroverse Modelle zur Interpretation dieser Größe diskutiert. Diese Modelle werden experimentell in dieser Arbeit überprüft. Dies erfordert die Entwicklung neuer experimenteller Aufbauten basierend auf nichtlinearen, optischen Techniken. Mit diesen Experimenten konnte eines der Modelle bestätigt werden.

ABSTRACT

Adsorption layers of soluble surfactants enable and govern a variety of phenomena in surface and colloidal sciences, such as foams. The ability of a surfactant solution to form wet foam lamellae is governed by the surface dilatational rheology. Only systems having a non-vanishing imaginary part in their surface dilatational modulus, E, are able to form wet foams. The aim of this thesis is to illuminate the dissipative processes that give rise to the imaginary part of the modulus.

There are two controversial models discussed in the literature. The reorientation model assumes that the surfactants adsorb in two distinct states, differing in their orientation. This model is able to describe the frequency dependence of the modulus E. However, it assumes reorientation dynamics in the millisecond time regime. In order to assess this model, we designed a SHG pump-probe experiment that addresses the orientation dynamics. Results obtained reveal that the orientation dynamics occur in the picosecond time regime, being in strong contradiction with the two states model.

The second model regards the interface as an interphase. The adsorption layer consists of a topmost monolayer and an adjacent sublayer. The dissipative process is due to the molecular exchange between both layers. The assessment of this model required the design of an experiment that discriminates between the surface compositional term and the sublayer contribution. Such an experiment has been successfully designed and results on elastic and viscoelastic surfactant provided evidence for the correctness of the model.

Because of its inherent surface specificity, surface SHG is a powerful analytical tool that can be used to gain information on molecular dynamics and reorganization of soluble surfactants. They are central elements of both experiments. However, they impose several structural elements of the model system. During the course of this thesis, a proper model system has been identified and characterized. The combination of several linear and nonlinear optical techniques, allowed for a detailed picture of the interfacial architecture of these surfactants.

PUBLICATIONS

Until now, the following publications, representing the work that has been done in this thesis, have been published:

1. H.-D. Wantke, J. Örtegren, H. Fruhner, **A. Andersen**, H. Motschmann, Colloids and Surfaces A: Physicochemical and Engineering Aspects, *261, (2005), 75-83.*

2. M. Schneider, **A. Andersen**, P. Koelsch, H. Motschmann, Sensors and Actuators B: Chemicals, 104 (2005) 276-281.

3. V. Fazio, J. Örtegren, P. Koelsch, **A. Andersen**, D. Wantke, H. Möhwald, H. Motschmann, Proc. SPIE Vol. 5223, Physical Chemistry of Interfaces and Nanomaterials II; p.38-48, Dec. 2003.

Moreover, the following publications are in preparation:

4. **A. Andersen**, H. Motschmann, Characterization of the interfacial architecture of a soluble hemicyanine dye series by means of nonlinear optics.

5. **A. Andersen**, J. Ortegren, K.-D. Wantke, H. Motschmann, Oscillating bubble SHG on surface elastic and surface viscoelastic systems. New insights in the dynamics of adsorption layers.

6. **A. Andersen**, H. Motschmann, Oscillating bubble SHG measurements on N-8-alkyl-4'-(dimethylamino)-stilbazium bromide.

ACKNOWLEDGMENTS

First I would like to thank the MPI and Prof Dr. Möhwald for giving me the opportunity of studying in Germany. It has been quite an adventure and I enjoyed it very much.

The one person I'd like to most warmly thank is Hubert (Dr. Hubert Motschmann). Thanks for your extravagant-almost-impossible-to-realize but how challenging ideas, thanks for your wonderful patience while teaching me the basics of everything I just didn't know and thanks for your passion in science.

Thank you Dieter (Dr. Klaus-Dieter Wantke) for encouraging me, explaining me these terrible mathematical models and for all our little discussions in the S-bahn.

When I came in Golm, I had no idea about laser. I'm grateful to Jonas (Dr. Jonas Örtegren) for teaching me how to "tame" such a monster, for his friendship and for his help during my PhD. I would also like to thank Patrick (Patrick Kölsch), from our Gibbs monolayer group, for his help, whenever I needed it.

I also want to thank Ingeborg (Frau Bartsch) and Gabi (Frau Wienskol) for being always so ready to help me, for their kindness and for their patience while listening to my broken German. I also would like to thank Andreas Kretschmar who always built my setups as fast as he could, as well as Wolfgang Stein, who helped me a lot with the electronics of the laser.

My life in Golm would have been much different and probably much more boring if I wouldn't have had the chance to meet the two best officemates I ever had in my life. Thank you Zhihua (Dr. Zhihua An) and Naoko (Naoko Miyashita) for cheering me up so many times… I'll miss you girls!

Golm is a place where people come and go… sometimes too fast. I would like to thank here Vera (Dr. Vera Bosio), Gemma (Dr. Gemma Ibarz Ric), Julia (Julia Maldonado-Valderamma), Mahassine (Dr. Mahassine Safouane), Christophe (Dr.

Christophe Déjugnat), Nicolas (Dr. Nicolas Delorme), Elena (Dr. Elena Maltesa), Michelle (Michelle Prevot), Annabel (Dr. Annabel Muenter), Chris (Dr. Christopher Haluska), Said (Said Aranda) and everyone else who shared for a while my everyday life.

Thanks to the Football Team! It was always a pleasure to play with you guys! I'll be always happy to come back for a small game!

I have a bunch of friends, spread all over the world, who always tried to encourage me even when they didn't quite understand what I was talking about… Thanks to Florence, Stéphanie, Maritza, Marie-Josée, Julie, Geneviève, Eve, Catherine and Félicia.

Even far far away, my family always encouraged me in my choices, even though they were not so happy to let their oldest daughter leave for the remote Germany. Even if I don't see you so often, I always think of you… Merci papa et maman, Roxi, Clo, Alex, Adam et Thérèse… vous me manquez tous.

Finalement, un merci tout spécial à Sébastien, qui a toujours été là, et qui, depuis le début, m'encourage et me soutient. Merci pour ton sourire, pour ta joie de vivre... merci d'être si formidable.